UNIVERSITÀ DEGLI STUDI DI TORINO

FACOLTÀ DI SCIENZE MATEMATICHE
FISICHE E NATURALI

TESI DI
DOTTORATO DI RICERCA IN FISICA

Beam induced electron multipacting in the CERN Large Hadron Collider accelerator LHC

Relatori: Professor E. Chiavassa e Dr. O. Gröbner

Correlatore: Dr. J.M. Laurent

Coordinatore: Professor Ra¤aello Garfagnini

Candidato: Dott. Mauro Pivi

XII CICLO
ANNI ACCADEMICI 1996 1999

Contents

I Introduction **1**

II Beam-induced multipacting in LHC a Theoretical Introduction **7**

1 Electron-cloud in the LHC **11**
1.1 Introduction 11
1.2 A model for multipacting in the LHC - Energy gain during the passage of a proton bunch 12
1.2.1 Hamiltonian formalism: simplified model in the kick approximation 12
1.2.2 Multipacting conditions 14
1.2.3 Critical Secondary Emission Yield and heat load in the LHC 14
1.3 Electron-cloud: SPS observations during MD with LHC type beams 18

2 Experimental test set-up for simulating multipacting in LHC **21**
2.1 Traveling-Wave multi-wire chamber 22
2.1.1 Experimental setup and limits to simulate the LHC proton bunches 22
2.1.2 Electric field in the multi-wire chamber 23
2.2 100 MHz Coaxial Resonant Cavity 26
2.2.1 Experimental setup for testing multipacting 26
2.2.2 Electric and magnetic fields in the resonant cavity 27

III Experiments with a Traveling-Wave test chamber and a 100 MHz resonant cavity **31**

3 Multipacting conditions **33**
3.1 Experimental setup general overview 34
3.2 A model for multipacting in the TW chamber 36
3.2.1 Equations of motion for the reference particle 39
3.2.2 Multipacting as a function of the pulse width and period 41
3.2.3 Multipacting threshold 44
3.3 Experimental results 45
3.3.1 Multipacting dependence on the pulse parameters: period, width and amplitude 45

3.3.2 Multipacting as a function of the pulse width and period 47
3.3.3 Multipacting dependence on the bias-voltage 48
3.3.4 Resonance threshold 49
3.3.5 Mapping the multipacting regions in the multi-wire chamber 50
3.4 LHC multipacting computer simulations 53
3.4.1 Simulation results 53

4 Electron energy spectrum **59**
4.1 Electron energy spectrum in the travelling-wave chamber 60
4.1.1 Experimental setup and energy spectrum analyzer 60
4.2 Electron energy spectrum - measurements and simulations 63
4.2.1 Critical secondary emission yield in the multi-wire chamber 66

5 Remedies to reduce the electron-cloud build up **73**
5.1 Introduction 73
5.1.1 Secondary electron emission 75
5.1.2 Ultra-high vacuum physics: gas desorption in dynamical vacuum . . 76
5.1.3 Electron stimulated desorption (ESD) 77
5.2 Decreasing of multipacting during conditioning 77
5.2.1 Minimum pulse amplitude as a function of the electron dose and of the bake-out of the system 78
5.2.2 Electron stimulated desorption during multipacting 80
5.2.3 Secondary electron yield as a function of the electron dose 81
5.2.4 Reduction of the secondary electron electron yield by multipacting in the multi-wire chamber 83
5.2.5 Reduction of the secondary electron yield by beam scrubbing in the arcs of LHC 86
5.3 Freon plasma conditioning - CCl_3F 89
5.4 Freon plasma conditioning of a copper surface 94
5.5 Thin film TiZrV Non Evaporable Getter (NEG) coating 96
5.6 Measurement of the secondary electron yield 99
5.6.1 Experimental set-up and calibration of the system 99
5.7 Auger electron spectroscopy analysis 101
5.7.1 Electron cloud scrubbing effect 102
5.7.2 Samples exposed to freon plasma conditioning 105
5.7.3 Effect of freon plasma on the surface during multipacting 106

6 Suppression of multipacting with a solenoid magnetic field **113**
6.1 Solenoid magnetic field experimental setup and measurement 114
6.2 Model 115
6.3 Solenoid magnetic field in the LHC field-free regions of the LHC 117

7 100 MHz Coaxial resonant cavity **123**
7.1 Experimental set-up general overview 124
7.1.1 Coupling loop calculation 125

7.1.2 Measurement of the quality factor Q 126
7.1.3 Multipacting in the resonant cavity 127

IV Conclusions **131**

V Bibliography **137**

VI Appendixes **143**

A Fourier series of the RF pulse **145**

B Setting the correct square pulse amplitude for the simulations **146**

C LHC multipacting simulation program adapted to the multi-wire chamber geometry **148**

D Calibration of the residual gas analyzer **150**

Aknowledgements **153**

Part I

Introduction

Multipacting is a phenomenon which can absorb RF energy, and lead to the development of vacuum breakdown, in high power RF and microwave systems. The multipacting phenomenon was first described in 1934 by Farnsworth [1], the word deriving from "resonance of multiple electrons impact". Electric fields present in many vacuum systems may accelerate electrons (produced by field emission, photo-emission, ionisation of residual gas molecules, etc.) towards the dielectric or metallic surface. If the bombarding electrons acquire enough energy they produce secondary electrons. The secondary electrons may in turn be accelerated if the electric field normal to the surface is in the correct phase and they may bombard another surface which again emits secondary electrons.

This 'bouncing' back and forth between surfaces is the multipacting (or multipactor) effect. When the secondary emission coefficient is greater than unity, the electron density and the power delivered to the surface increase exponentially, usually ending in catastrophic failures of the system performances. Even if the power transferred by the multipacting process is too small to cause thermal damage or arcing, the process may cause surface charging which sets up local fields which may exceed the characteristics of the material surface (ex. dielectric strength). In summary, multipacting is a phenomenon of electron multiplication resonance, which develops by secondary electron multiplication between two opposed surfaces, when a cyclic voltage is maintained between them, and:

- if the resonant conditions for electron trajectories are fulfilled
- if the primary electrons energy at collision with the wall results in a secondary emission yield greater than unity.

A multipacting discharge develops between two opposite surfaces, a thin sheet of electrons (electron cloud) forms approximately parallel to the two surfaces. The current carried by the electron cloud at each half cycle increases exponentially with time and is usually limited by space-charge, available RF power or impedance change in the transmission lines. In space-charge limitation, the repulsion due to electron cloud cause some electrons to fall out of phase with the applied electric field, and pushing back of secondary electrons which are emitted from the surface, thereby limiting the exponential growth of the electron cloud.

Beam induced multipacting driven by the electric field of successive proton bunches in large accelerators, was first observed in the proton-proton storage ring ISR at CERN [2]. A pressure rise due to gas desorption induced by electron bombardment of the vacuum chamber walls, under the influence of the radial electric field of the protons, was observed.

Recently some laboratories in the world have recorded a pronounced pressure increase during operative conditions. In the positron ring of PEPII beauty factory, beyond a current threshold a pressure rise is observed. In KEKb the same effect occurs, but the concomitant ion-induced desorption effect could take place in this case.

In the LHC the synchrotron radiation from proton bunches creates photoelectrons when hitting the beam screen, wall of the vacuum chamber. The synchrotron radiation is the dominant source of electrons for the LHC. These photoelectrons are accelerated towards the positively charged proton bunch and drift across the beam pipe between successive bunches. When they hit the opposite side of the vacuum chamber, they generate

secondary electrons which can in turn be accelerated by the next proton bunch. The energy transferred to the electrons may be significant since the peak electric potential of the proton beam is several kV.

If the secondary emission yield exceeds unity, the electron cloud may grow up exponentially and, as a consequence, the heat load produced on the beam pipe, the space charge in the chamber and energy coupling between the electrons and the beam, and the associated fast pressure increase due to electron induced desorption, could ultimately cause a catastrophic loss of the proton beam.

A first condition for the onset of multipacting is related to the transit time of the electrons from wall to wall which must be equal or less than the time between two successive proton bunches, resulting in an electron cloud which moves in synchronism with the beam. A second condition to satisfy is that the energy transfer to an electron must be sufficient to have a secondary emission yield greater than unity, when the electron hits the wall.

In the case of LHC the multipacting have been previously studied at CERN by means of computer simulation codes [3][4], and it has been predicted that an electron multiplication resonance can take place for nominal beam parameters in the accelerator (proton energy 7TeV, beam current intensity 0.53A). Moreover simulations, obtained with the computer code before this thesis work, have shown that multipacting has a decisive dependence on the proton beam parameters (intensity, length and bunch period).

Motivated by a potential existence of an electron cloud in LHC, an extensive experimental research program is underway at CERN to quantify the key parameters driving this phenomenon.

During this thesis work I have investigated a beam-induced multipacting by means of a travelling-wave (TW) multi-wire chamber. The electric field of the bunched proton beam is simulated by short square RF pulses supplied by a pulse generator and applied to six equispaced wires inside a 1.4 m long stainless steel vacuum chamber (100 mm diameter). The system is fitted with an electron pick-up which can measure the electron current incident on the wall; multipacting is revealed by a fast pressure increase in the system, and by an electron current at the pick-up. The system clearly exhibits a multipacting behaviour, that is sensitive to:

· the pulse amplitude (related to the bunch intensity in LHC)
· the repetition rate (bunch spacing)
· the pulse width (bunch length)

The advantage of this travelling wave system with respect to a simpler standing wave system is that the secondary electrons drift takes place in the field free period between pulses and thus simulates more closely the phenomenon in the LHC.

To validate the LHC computer simulation code, the program used for LHC has been adapted to the travelling wave experimental set-up, and new simulations have been performed with the multi-wire chamber geometry.

Moreover, a model for multipacting has been studied in order to explain the dependence of multipacting on the RF pulse parameters in the multi-wire chamber. The results obtained with the model have been compared with the experimental results.

Furthermore, I have studied the physical parameters influencing the effect, such as

vacuum chamber material, cleaning and surface treatments by means of the TW multi-wire chamber in order to better understand multipacting and to find the most effective ways to reduce this critical phenomenon for LHC.

A 100 MHz standing wave (SW) cavity has also been made to study multipacting with higher electric fields than in the multi-wire chamber. In the SW configuration, after the optimization of the system, I have so far performed the first test checking for multipacting inside the cavity.

Finally in the SPS accelerator at CERN during the Machine Development (MD) with an LHC-type beam, above a threshold beam intensity a pressure rise by more than a factor 50 has been observed. Multipacting has unambiguously been confirmed in the SPS, because preliminary tests excluded the possibility of ion induced desorption, and by my observations. An extensive program is underway for the SPS in order to test the possible remedies, and to avoid the detrimental effect of the electron-cloud in the LHC accelerator.

Part II

Beam-induced multipacting in LHC a Theoretical Introduction

Notation and nomenclature

Here is a list of notations and conventions used in the following chapters. We will refer to "multipacting", or simply to "electron multiplication", having the same meaning in the context of this thesis. The "electron cloud" is due to the growth of the multipacting.

$u(t)$ *or* A	RF pulse amplitude (square pulse)
V_{p-p}	RF pulse amplitude as measured at the scope: peak to peak
T	Period between two proton bunches or two RF pulses
W	RF square pulse width - FWHM (tipically $10n$ sec)
V_a	DC potential applied to the six wires
$Vmin$	Minimum tension related to the RF signal measured at the scope
V_b	Bias-voltage with respect to ground: $(= \mathrm{V}_a + \lvert \mathrm{V}_{min} \rvert)$
δ or SEY	Secondary electron yield
$\delta_{\max}$	Maximum of the secondary emission yield curve also $= \delta(E_{\max})$
$h(\xi)$	Normalized secondary emission yield $(\delta/\delta_{\max})$
$E_{\max}$	Energy at which the secondary emission yield is maximum
$E_{1,2}$	Energy at which the secondary emission yield is $\delta(E_1) = 1$, $\delta(E_2) = 1$
σ_{se}	Width of the initial energy distribution of the seconday electrons
E_{imp}	Electron impact energy at the vacuum chamber surface
E_{peak}	Energy corresponding to the peak of the distribution
t_{imp}	Instant at which the electron hits the opposite side of the chamber
TOF	Time of flight
f	Fraction of the period corresponding to the flight of the electron
R_0	Chamber radius
R_p	LHC beam pipe radius $1.8 \div 2.2cm$ min÷max
R	Reflectivity of the LHC beam screen
U_1	Energy analyzer inner electrode potential
res	Resolution of the electron energy spectrum analyzer
$f(E)$	Electron energy distribution function [in A]
δ_{crit}	Critical SEY, minimum $\delta_{\max}$ necessary to have electron multiplication
N_0	Number of electrons per unit area incident at the wall
N_{se}	Number of secondary electrons per unit area
I_{beam}	Intesity of the proton beam
N_b	Number of protons per bunch
σ_z	Longitudinal proton beam size
W_{pe}	Heat load of the vacuum chamber wall [W/m]

$< E_{pe} >$	Average kinetic energy of the photo-electrons after bunch passage
Y	Effective quantum yield, num. of electrons emitted per incident photon
CCl_3F	Freon11 Trichloro-monofluoro-methane
B_z	Axial magnetic flux density
$FWHM$	Full width at half maximum
r_e	Classical electron radius
m_e	Mass of the electron
$\sigma_D(E', M)$	Desorption cross section for all channels
α	Sticking coefficient, probability for an impinging molecule to be absorbed
E_γ	Critical energy of the synchrotron light photons

Chapter 1

Electron-cloud in the LHC

1.1 Introduction

The synchrotron radiation in the LHC creates a continuous flow of photoelectrons when hitting the vacuum chamber wall. These electrons are accelerated by the electric field of the bunch and hit the vacuum chamber on the opposite side of the beam pipe where they create secondary electrons which are in turn accelerated by the next bunch. If the secondary electron yield exceeds unity, the electron cloud may grow up exponentially and, as a consequence, the heat load produced on the beam pipe, the space charge in the chamber, the energy coupling between the electrons and the beam, and the associated fast pressure increase due to electron induced desorption could ultimately cause a catastrophic loss of the proton beam. In the magnetic field free regions, the accelerated electrons move radially towards the beam center. In the strong dipole field, the electron motion is effectively confined to a motion along the vertical field lines and the energy gain of an electron during the bunch passage does not only depend on its radial distance from the beam but also on its horizontal position inside the beam pipe. Consequently, the average energy gain of the electrons in the field–free regions during a bunch passage is larger than in the regions with strong dipole field.

Previous simulations performed at CERN with the LHC multipacting program have shown that depending on the photo-electron yield, the secondary emission yield and the reflectivity of the beam screen material, the heat load can vary from 0.1 Watt/meter to more than 15 Watt/meter. The cryogenic system cannot tolerate a total heat load exceeding 0.5 Watt/meter, and the cryogenic budget is based on an heat load induced by multipacting of only 0.2 Watt/meter.

The design of the beam screen must assure an heat load which is smaller than this amount.

In this theoretical chapter we will discuss the model for multipacting and the multipacting conditions. The energy gain during the passage of a proton bunch and the threshold proton intensity necessary for multipacting to occur are discussed in section 1.2. The number of secondary electron emitted by impinging primary electron, secondary electron yield, is an important parameter for the electron cloud growth. The concept of a critical secondary electron yield, threshold for multipacting, will be introduced in section

1.2.3.

Recently multipacting has been unambiguously observed in the SPS accelerator at CERN with an LHC-type proton beam [5], during machine development (*MD)* sessions for LHC. The measurements performed in the SPS are shown in section 1.3.

1.2 A model for multipacting in the LHC - Energy gain during the passage of a proton bunch

1.2.1 Hamiltonian formalism: simplified model in the kick approximation

Consider a beam pipe with a highly relativistic proton source distribution moving in the z direction. Assume that the beam pipe consists of a single perfectly conducting surface. The Hamiltonian describing the motion of a non-relativistic test particle with mass m_e and charge $q = -e$ is

$$H = \frac{p_r^2}{2m_e} + \frac{p_\theta^2}{2r^2 m_e} + \frac{\left(p_z + \frac{1}{c}eA_z(r, z-\beta ct)\right)^2}{2m_e} - e\phi(r, z-\beta ct). \tag{1.1}$$

It is expected that the magnetic field due to the proton source distribution will have a small effect on the electron motion. The magnetic field due to the beam is given by

$$B_{max} = \frac{2I_{max}}{cR_p} = \frac{2eN_b}{\sqrt{2\pi}\sigma_z R_p} \approx 2.5\ Gauss$$

considering the pulse width $\tau = \sigma_z/c$ and the cyclotron frequency $\omega = \frac{eB\max}{m_e c} \approx 40$ MHz, we have then $\omega\tau = 0.039$. As a conclusion the magnetic field is not important for the electron dynamics. Thus, the vector field A_z term in the Hamiltonian (1.1) can be dropped.

The electromagnetic field carried by a relativistic point charge, is Lorentz contracted into a thin disk perpendicular to the particle's direction of motion with an angular spread of the order of $1/\gamma$, where γ is the Lorentz energy factor. In the ultrarelativistic limit of $v = c$, the disk shrinks into a δ-function width. The electric field $\vec{E}$ points strictly radially outward from the point charge. The longitudinal distribution of the electric charge of the proton bunch is large compared to the beam pipe radius, as a consequence, the energy gained in the longitudinal direction is relatively small. This allows to drop the p_z term, and z is simply a parameter in the problem. The longitudinal kick is ignored here. To treat properly, the entire p_z term should be kept, including A_z. There will probably be little effect on the total energy gain, but knowledge of how particles drift longitudinally between the bunch passages is potentially important. Finally, the angular momentum p_θ of the test charge is taken to be zero.

The simplified Hamiltonian is then

$$H = \frac{p_r^2}{2m_e} - e\phi(r, z-\beta ct) \tag{1.2}$$

In the kick approximation we assume that the proton bunch passes by before the test charge has started to move. The initial position of the photoelectron will be at the beam pipe wall, $r = R_p$, the beam pipe is generally well outside of the bunch. Well outside of the beam the scalar electromagnetic potential of a circular beam in a circular beam pipe reduces with a good approximation to

$$\phi(r, z - \beta ct) \approx \phi\,(r) = \frac{\lambda}{2\pi\varepsilon_0} \ln r \tag{1.3}$$

where λ is the line charge of the bunch $\lambda = \frac{q_b}{\sigma_z} = \frac{eN_b}{c\tau}$.

When the test charge position does not change, using Eq. (1.2) and Eq. (1.3), the total change in p_r as a result of one bunch passage of length τ is given by the Hamilton equation

$$\Delta p_r = -\frac{\partial H}{\partial r}\tau \tag{1.4}$$

$$\Delta p_r = e\frac{\partial \phi}{\partial r}\tau = \frac{e^2 N_b}{2\pi\varepsilon_0 cr} \tag{1.5}$$

independent of the bunch length. From this follows the net energy gain after the kick

$$\Delta E = \frac{1}{2m_e}\left(e\frac{\partial \phi}{\partial r}\tau\right)^2 \tag{1.6}$$

thus, the photoelectron at initial position $r = R_p$, would receive an energy kick

$$E_{\max} = \frac{2e^4 N_b^2}{(4\pi\varepsilon_0)^2 m_e c^2 R_p^2} = 2m_e c^2 r_e^2 \left(\frac{N_b}{R_p}\right)^2. \tag{1.7}$$

In the LHC the maximum energy gain for a photoelectron is then given by $E_{\max} \approx 200eV$, for a circular beam pipe of radius $R_p = 2\ cm$. The velocity increment being $\Delta v = \frac{\Delta p_r}{m_e} = \frac{e^2 N_b}{2\pi\varepsilon_0 m_e cr} = 2cr_e\frac{N_b}{r}$.

To calculate the energy gain of the electrons at any position in the beam pipe a more realistic result can be obtained by introducing the following two generalizations:

- the radial distribution of the beam charge is assumed to be gaussian and the scalar potential $\phi(r, z) = 4\pi \int_0^r r' \ln \frac{r'}{r}\rho(r', z)dr'$
- the electrons are not stationary but move during the passage of the proton bunch

Including these generalizations, taking into account a *uniform* distribution of the electrons in the beam pipe and integrating Eq. (1.2), we obtain the average energy gain $< \Delta E > \approx 650eV$, when considering LHC nominal beam conditions. The average energy gain results from the integration of the average energy gain as a function of the radial position r of the test particle in the beam pipe [7][8].

1.2.2 Multipacting conditions

The electrons must cross the vacuum pipe, in synchronism with the bunches to allow to give multipacting. The transit time has to be less than or equal to the time between successive bunches $\frac{2R_p}{\Delta v} \leq T$. Introducing the bunch distance $L_{bb} = cT$, the wall-to-wall transit time condition determining the threshold number of protons per bunch becomes

$$N_b = \frac{R_p^2}{r_e L_{bb}}. \tag{1.8}$$

With $I_b = \frac{eN_b}{T}$, the condition $N_b = \frac{R_p^2}{r_e L_{bb}} = \frac{R_p^2}{r_e cT}$, gives the equivalent condition on the beam intensity

$$I_{beam} = \frac{4\pi\varepsilon_0 m_e c}{e} \frac{R_p^2}{T^2}. \tag{1.9}$$

Evaluation for LHC

Beam parameters for the LHC at nominal beam conditions

$E_p(GeV)$	k_b	N_b	$\sigma_z(m)$	$I_b(A)$	$T(ns)$	$L_m(m)$	$B(T)$	$E_\gamma(eV)$	$R_p(m)$
7000	2835	$1.05{\cdot}10^{11}$	0.075	0.54	25	14.2	8.4	44.1	0.02

where E_p is the beam energy, k_b number of bunches per proton beam, I_b the average current, L_m and B the bending magnet length and the bending field at top energy respectively. The bunch charge is $q_b = 1.68 \cdot 10^{-8} C/bunch$. The electric field due to the proton bunch (long bunch approximation) is given by $E = \frac{q_b}{2\pi\varepsilon_0 \sigma_z R_p} \simeq 160 kV/m$. In the kick approximation the electron motion during the bunch passage is $d = \frac{eE}{m_e}\tau T = 7\ 10^{-4} m$, the threshold resonance condition for multipacting is given by $I_{beam} = \frac{4\pi\varepsilon_0 m_e c}{e}\frac{R_p^2}{T^2} \approx 0.19A$.

1.2.3 Critical Secondary Emission Yield and heat load in the LHC

The secondary electron yield (SEY) is the parameter involved in the building-up of the electron cloud, and is defined as the number of secondary electrons emitted per incident electron on the surface.

The secondary electron yield as a function of the energy E of the electron and incidence angle θ is given by Eq. (C.1) in appendix C, it can be expressed by the formula

$$\delta_{SEY}(E,\theta) = \frac{\delta_{\max}}{\cos\theta} h\left(\frac{E}{E_0}\right) \tag{1.10}$$

where $\delta_{\max}$ is the maximum yield, E_0 is the energy corresponding to the maximum, and θ is counted from the normal to the surface and the function $h(\xi)$ is given by the following formula

$$h(\xi) = \frac{\delta}{\delta_{\max}} = 1.11\xi^{-0.35}\left(1 - e^{-2.3\xi^{1.35}}\right)$$

thus, representing the normalized SEY.

The condition for an exponential growth in the number of electrons is obtained when the secondary electron yield is larger than a critical value. The expression for the critical secondary emission yield in the LHC is given by [20][21]

$$\delta_{\max} \geq \delta_{crit} = \left(\int_0^{y_0(x)} \frac{1}{\cos\theta} h\left(\frac{E}{E_0}\right) \frac{n_e(x,y,T)}{n_0(x)} dy\right)^{-1} \tag{1.11}$$

where $n_0(x)$ is the number of photoelectrons per unit area in the x-z plane, produced by the passage of the first proton bunch, dependent generally on the horizontal position x, and $n_e(x,y,t)$ the density of the electrons at time t, after being accelerated by the same proton bunch. In the dipole magnets the electron motion is constrained to the vertical direction y, then for a circular beam pipe the angle θ is related to x through $\cos\theta = y(x)/R_p$.

If $\delta_{\max} \geq \delta_{crit}$, the initial number of electrons will be multiplied after each bunch passage by a factor $1+q$, where $q = \mid \delta_{\max}/\delta_{crit} - 1 \mid$. Unlimited growth will eventually be stopped by the space charge effect in the chamber. The contribution given by multiple bunch passages lead to the exponential growth

$$N_e \approx \frac{N_{se}}{q} e^{\frac{qt}{T}}$$

where N_{se} is the total number of secondary electrons produced by the photoelectrons. N_{se} depends on the characteristics of the beam pipe surface such as the photo-electron yield, the secondary emission yield and on the number of protons per bunch. All these parameters determine the number of photo-electrons produced by the first bunch passage.

If the multipacting condition is not satisfied $\delta_{\max} < \delta_{crit}$, the initial electron cloud will decay exponentially $N_e \approx e^{\left(-\frac{qt}{T}\right)}$.

It is then important to determine the value of δ, below which the multipacting effect in LHC is substantially reduced.

In order to find the critical secondary electron yield for LHC, the evolution with time of the number of electrons per unit length has been studied. The electron density will decrease if the secondary emission yield is smaller than the critical value[1]. For the nominal LHC beam parameters[2], the critical SEY is

$$\delta_{crit} = 1.4$$

The critical secondary emission yield is in general a function of the bunch period and intensity. Fig. 1-1 shows the dependence on these bunch parameters. In the case of LHC

[1] it has been neglected the space charge effect and generate the photo-electrons for the first bunch

[2] a Gaussian distribution of the secondary electrons with σ_{se}=10eV has been considered

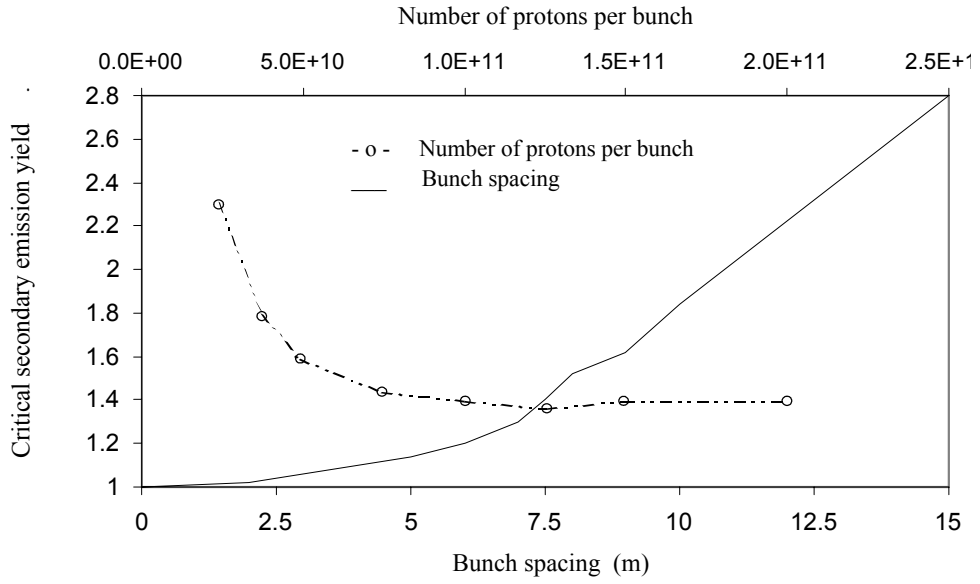

Figure 1-1: *The critical secondary emission yield coefficient versus the bunch spacing and the bunch intensity.*

the bunch spacing between the bunches is 7.5m. In order to obtain large values for δ_{crit} it would beneficial to have a larger bunch spacing, resulting in a small k_b and fewer bunches, but this will lead to a decrease in the luminosity defined as

$$L = \frac{N_b^2 k_b f_r \gamma}{4\pi\varepsilon_n \beta^*} \tag{1.12}$$

where f_r is the revolution time, ε_n the normalized transverse emittance, β^* the value of the betatron function at the interaction point.

The critical secondary emission yield remains constant for intensities larger than $1.0 \cdot 10^{11}$ protons per bunch, suggesting the possibility to double the bunch spacing and to increase the bunch population to $1.5{\cdot}10^{11}$ protons per bunch. This will give the same luminosity but a smaller heat loss in the beam screen than for the nominal LHC beam parameters. The heat load dependence on the effective secondary electron yield is shown on *left* of Fig. 1-2.

Heat load in the LHC beam screen

The cryogenic system can not tolerate a heat load induced by multipacting exceeding 0.2 W/meter. During a bunch passage the total number of photons emitted by a charge per radian is given by

$$N_\gamma = \frac{5}{2\sqrt{3}}\alpha\gamma$$

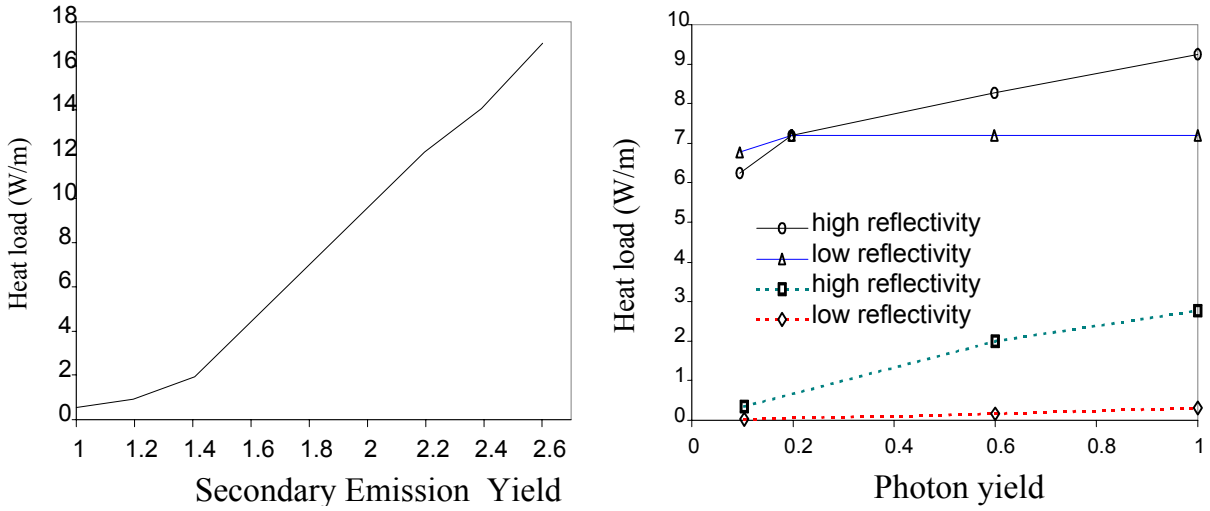

Figure 1-2: *Left*: *Heat load as a function of the secondary emission yield. The heat load, for* $\delta \rightarrow 0$, *is given by the photo-electrons.*
Right: *Heat load for high and low reflectivity, the two lower curves represent the case of* $\delta = 1.06 < \delta_{crit}$, *while the two upper curves represent* $\delta = 1.8 > \delta_{crit}$.

where α is the fine structure constant and γ the Lorentz factor. For protons at 7 TeV the critical frequency of these photons is $\omega_{crit.} = \frac{3}{2}\frac{c\gamma^3}{\rho}$, or the critical energy $E_\gamma = \frac{3\hbar c}{2\rho}\gamma^3 = 44eV$, and the total number of photo-electrons with energies larger then 4 eV (work function for copper) is approximately $0.17N_bY$ photons per bunch where $N_b = 1.05 \cdot 10^{11}$ is the bunch population and Y the photo-electron yield.

In regions with a strong dipole field the heat load depends also on the surface reflectivity. In case of high reflectivity the photons will be reflected many times and the beam screen can be uniformly illuminated, and as a consequence, the photoelectrons are approximately uniformly distributed over the surface of the beam screen. For a low reflectivity, they are mainly generated within the horizontal plane of the beam screen. The heat load due to the first bunch passages with the nominal LHC beam parameters is given by

$$W_{pe} = \frac{0.17N_\gamma Y < E_{pe} >}{T\ L_m} \tag{1.13}$$

Given an average photo-electrons energy $< E_{pe} >= 80eV$ and a effective quantum yield Y=0.2 we obtain W_{pe}=0.128W/m, representing the minimum heat load without any contribution from the electron cloud. The heat load produced by the photo-electrons created by the first bunch is near to the maximum tolerable budget of 0.2 W/m.

Because of the strong vertical magnetic field in the dipole magnets, the electrons are constrained to a motion along the vertical y magnetic field lines and electrons generated at the vacuum chamber near the horizontal plane can never reach the center of the beam pipe. The energy gain in the dipole section generally depends on the x, y position of the particle $E = E(x,y) = E_{\max}\frac{y^2}{(x^2+y^2)^2}R_p^2$. If the electrons are produced mainly in the horizontal plane

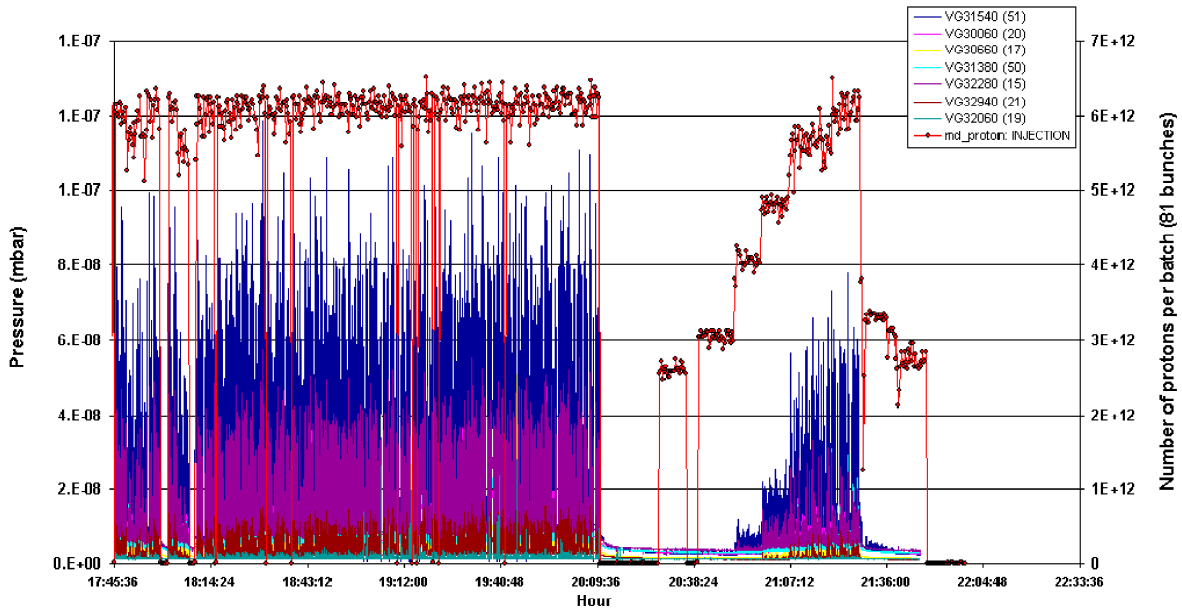

Figure 1-3: *Multipacting in the SPS during MD for LHC. Typically a pressure rise by more than a factor 50 is observed above a threshold beam intensity of ca. 3.5·10*^{12} *protons per batch.*

($y \rightarrow 0$) the heat load can be significantly reduced. *Right*-hand side of Fig. 1-2 shows the heat load for nominal beam parameters in an elliptical vacuum chamber, for a uniform distribution of the photo-electrons (high reflectivity), and for a distribution where 90% of the photo-electrons are generated around the horizontal plane (low reflectivity); the two lower curves represent the heat load in the case of $\delta = 1.06 < \delta_{crit}$, while the two upper curves represent the case of $\delta = 1.8 > \delta_{crit}$.

1.3 Electron-cloud: SPS observations during MD with LHC type beams

Recently multipacting has been unambiguously observed during dedicated *machine development (MD)* sessions for LHC in the SPS accelerator (LEP and LHC pre-accelerator), with LHC-type proton beam [5]. The multipacting signature is given by a pressure rise in the accelerator vacuum chamber due to electron stimulated desorption. Typically a pressure rise by more than a factor 50 has been observed above a threshold beam intensity. I took part in the measurements, and the results are shown in Fig. 1-3. Where it can be seen that the pressure started to rise above a proton threshold beam intensity of ca. 3.5 10^{12} protons per batch, where 81 LHC-type bunches per batch were present.

In addition to the pressure rise in the vacuum system I have measured the multipacting current of the electrons travelling across the vacuum chamber during multipacting.

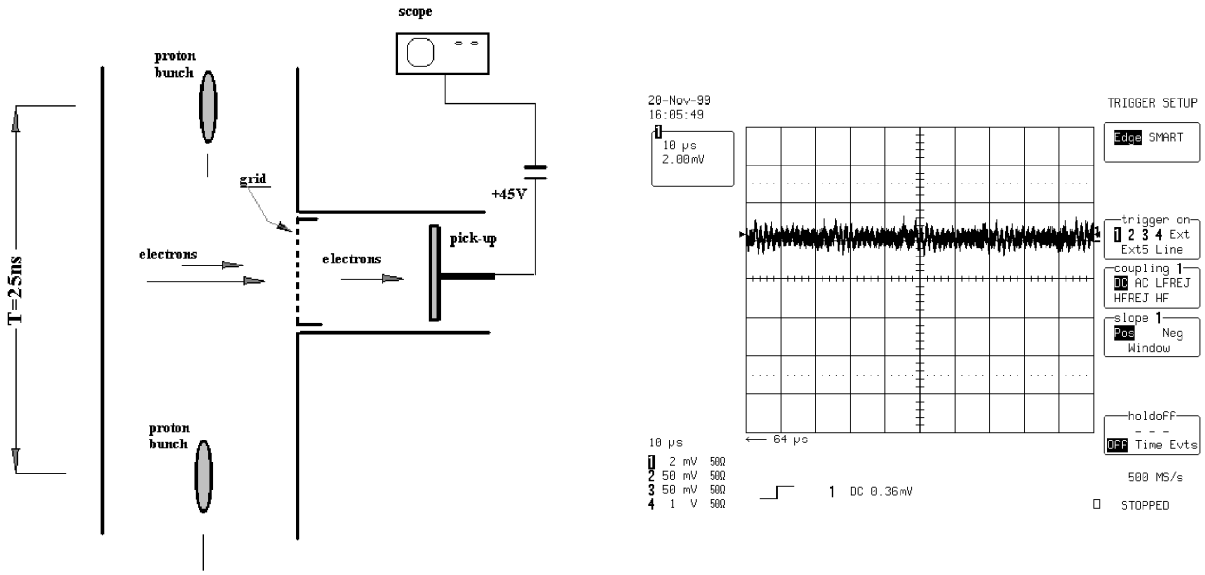

Figure 1-4: Left: *Experimental pick-up arranged in the SPS accelerator beam pipe. The pick-up collector is positively biased (+45V) with respect to ground in order to re-capture the secondary electrons emitted by the collector itself.*
Right: *signal recorded on the scope when the intensity was ca. 2.9 10^{12} protons per batch. A repetitive signal of 23 µs is recorded, due to the radiofrequency induced by the proton batch passage. No pressure rise was recorded at this time.*

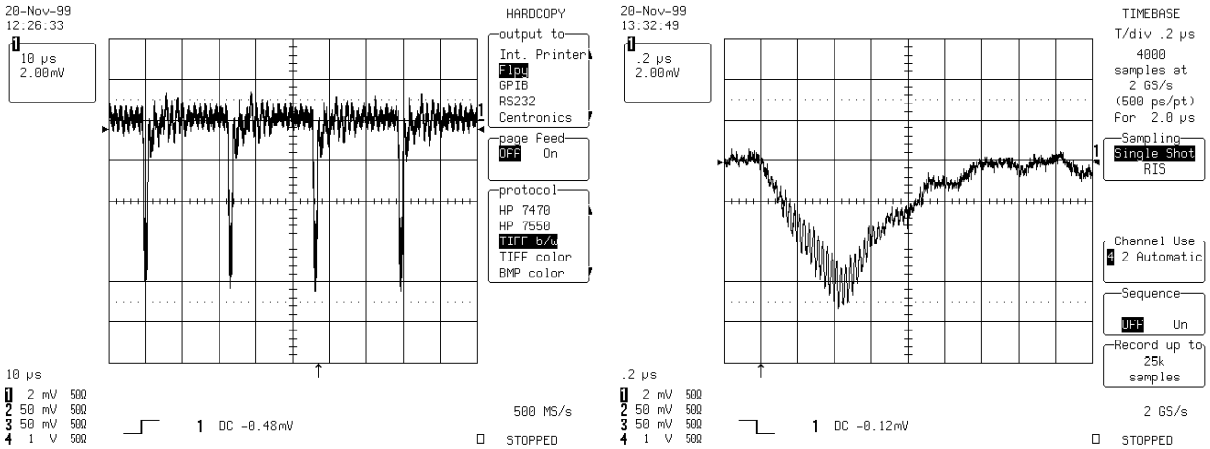

Figure 1-5: *Multipacting in the SPS during MD for LHC, proton intensity ca. 6.0 10^{12} protons per batch.*
Left: *The multipacting signal is recorded in synchronism with the proton batch revolution time accelerator of 23 µs. The horizontal scale is 10µs/div, the vertical scale is 2mV/div.*
Right: *different measurement in a different horizontal scale of 200ns/div. The increasing of the multipacting signal is repeated every passage of the proton bunch passage (25ns).*

Electrons pass through a grounded grid, and are collected by a pick-up probe, which has been arranged for the measurement, as shown on the left-hand side of Fig. 1-4. The pick-up collector is positively biased (+45V) with respect to ground in order to suppress the secondary electrons emitted by the collector itself.

I have used an oscilloscope with a high sampling rate, which allows to view single shot signals of the order of the proton bunch period (25ns). On the right-hand side of Fig. 1-4 is shown a measurement taken when the intensity was ca. 2.9 10^{12} protons per batch, where no pressure rise was recorded, e.g. the proton intensity was below the threshold for multipacting. The multipacting is visible in Fig. 1-5, when the intensity was ca. 6 10^{12} protons per batch. During this measurement a pressure rise was recorded, e.g. proton intensity above the threshold for multipacting. The multipacting signal is recorded in synchronism with the proton batch revolution frequency. The revolution time of the proton batch in the SPS accelerator is 23 μs.

Moreover, I performed some preliminary beam loss measurements during multipacting, by means of scintillators placed near the vacuum pipe, along the circumference of the accelerator. The interaction between the proton beam and the residual gas leads to the loss of protons, which produce a shower of charged particles when they hit the vacuum chamber. The scintillator synchronized with the revolution time of the batch can detect the charged particles passing through it. Thus, a small and rapid increase of the vacuum chamber pressure, due to multipacting, can be monitored by the scintillator.

An extensive program is underway at CERN in order to test in the SPS accelerator the possible remedies, which have been investigated by the recent studies (see below), to determine the most effective ways to avoid the detrimental effect of the electron-cloud in the LHC accelerator.

Chapter 2

Experimental test set-up for simulating multipacting in LHC

Introduction

A 1.4m long travelling-wave multi-wire chamber and a 100MHz resonant cavity have been built for the simulation of the electron multipacting induced by radio frequency, in order to study the parameters influencing the effect, such as vacuum chamber material, cleaning, surface treatments and to find the most effective way to avoid this critical effect in the LHC.

The systems are fitted with electron pick-ups which can measure the electrons incident on the wall, and the production of secondary electrons. The advantage of the travelling wave system with respect to the resonant system is that the secondary electrons drift during the field free period between pulses and thus simulates more closely the real situation in a proton accelerator. Nevertheless, the resonant cavity can produce higher electric fields, giving the possibility to study the multipacting phenomenon in more detail.

The two experimental set-ups are shown in Fig. 2-1. The resonant cavity is on the left-hand side, while the travelling-wave chamber is shown on the right-hand side. The two systems are provided with pumping systems, which include a primary pump, a turbo-molecular pump and an ion pump, assuring a base pressure below 10^{-9} mbar. In the TW system a residual gas analyzer is arranged between the multi-wire chamber and the turbo-molecular pumping system shown at the centre of the figure. The two systems are fitted with pick-up probes, properly arranged, for the detection of the multipacting electron current.

I will use the terms *chamber* and *cavity* for the travelling-wave and for the resonant system respectively.

In this chapter I will discuss the electromagnetic fields present in the two different systems. The travelling-wave multi-wire chamber is shown in section 2.1. In the same section, the electric field configuration which will be used for the computer simulations is presented.

The resonant cavity experimental set-up is shown in section 2.2, where an analytical introduction to the electric and magnetic fields, in the $\lambda/2$ operating mode, is presented.

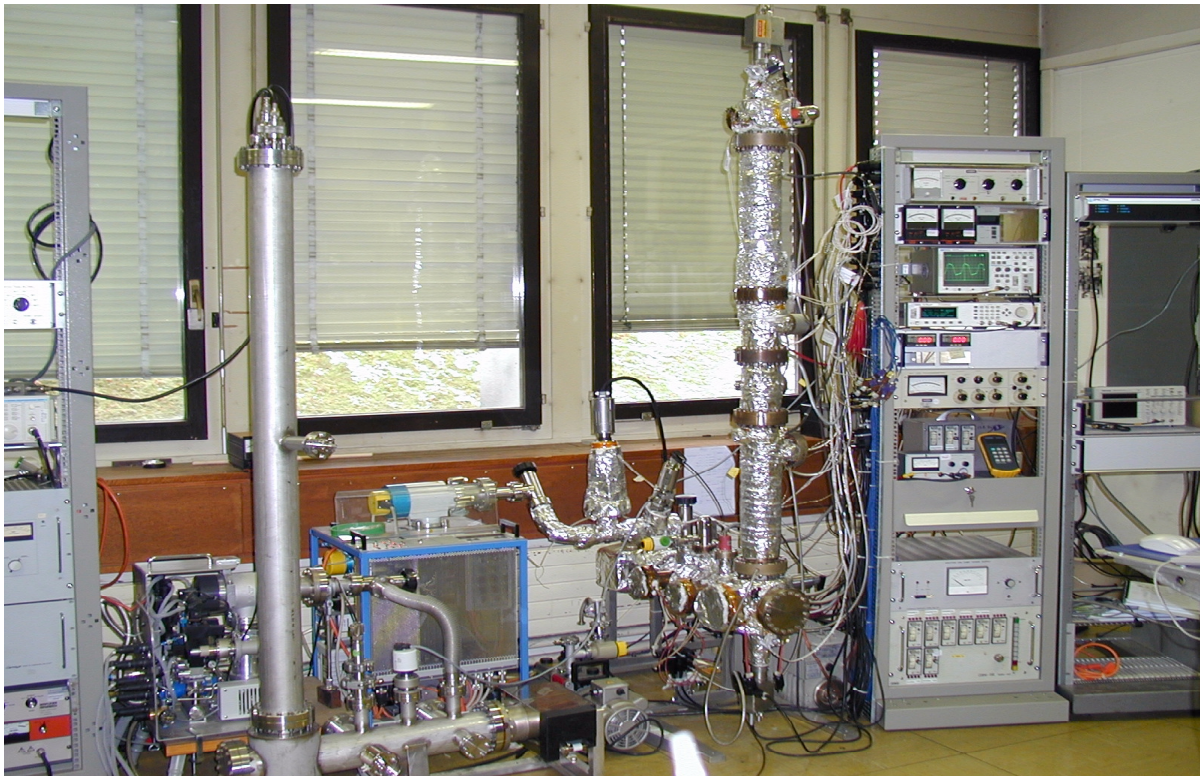

Figure 2-1: *100MHz resonant cavity (left) and travelling-wave multi-wire chamber (right) multipacting experimental set-up*

2.1 Traveling-Wave multi-wire chamber

2.1.1 Experimental setup and limits to simulate the LHC proton bunches

A vacuum chamber, 1.4m long with 100mm internal diameter, is equipped with six wires simulating the electric fields produced by a bunched proton beam by applying short rectangular pulses to the wires. The RF power is provided by a wide band RF amplifier driven by a pulse generator. The RF signal is sent to the multi-wire chamber, which needs to be matched with the 50 Ω impedance of the line, in order to avoid undesired reflections along the system. The impedance of the chamber depends mainly on the distance of the six wires from the central axis. In the actual configuration the measured impedance is ca. 53÷55 Ω inside the cavity and 71÷75 Ω at the position of the transitions; the impedance was measured with a reflectometer method. In the TW mode the input power is adsorbed by the terminating line load.

For LHC simulations in a TW configuration, we would need a high-power, high frequency pulse generator with adjustable characteristics (pulse length, period, amplitude). A power generator with the required characteristics does not exist, and we had to use available equipment. Nevertheless, we have reproduced the situation of the measure-

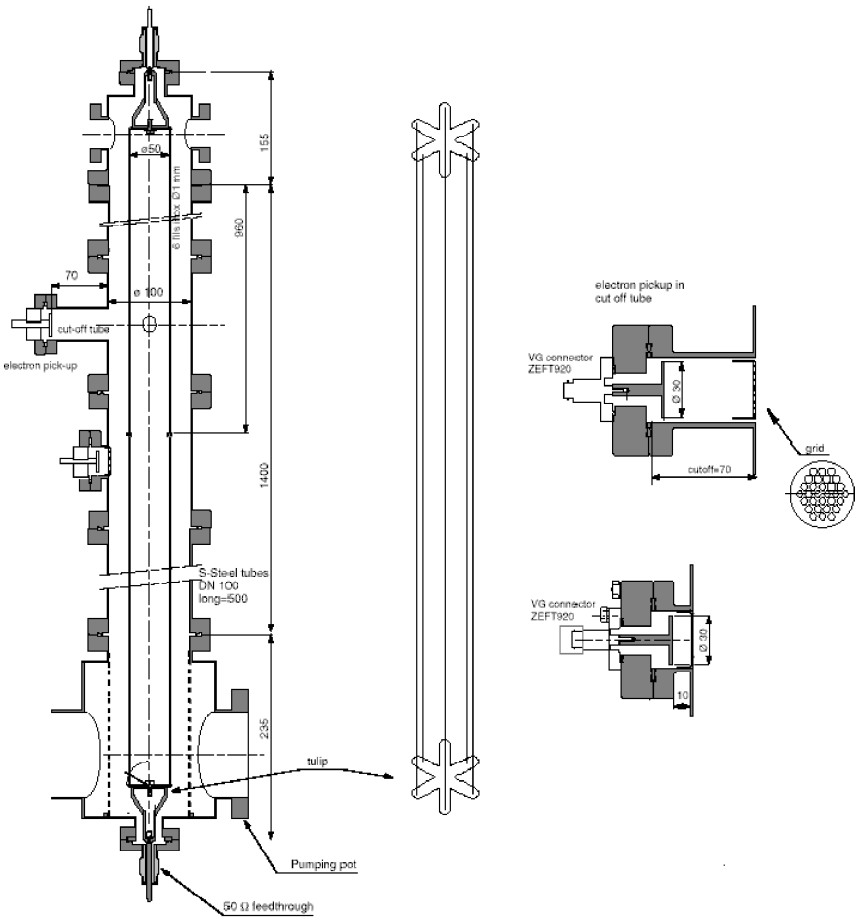

Figure 2-2: *Travelling-wave experimental set-up, a* tulip *holds the six wires. The electron pick-ups are arranged in a cut-off tube and shielded by grounded grids.*

ments in the ISR conditions [2], at lower power and lower bandwidth: 3 to 20 *ns* pulses with a 20 to 100 *MHz* repetition rate and peak to peak voltages up to 210V. This will allow us to study multipacting in the situation of a real accelerator, to test the multipacting simulation program used for LHC, to compare surface treatments and to estimate the secondary electron yield.

2.1.2 Electric field in the multi-wire chamber

In order to estimate the electric field in the experimental multi-wire chamber given by the six charged wires I assume:

- bi-dimensional problem, where the x-y transverse section is considered ($\ddot{z} = 0$)
- *no* magnetic field, as the velocity of the electron inside the multi-wire chamber is low and the $\vec{v} \times \vec{B}$ term is negligible.

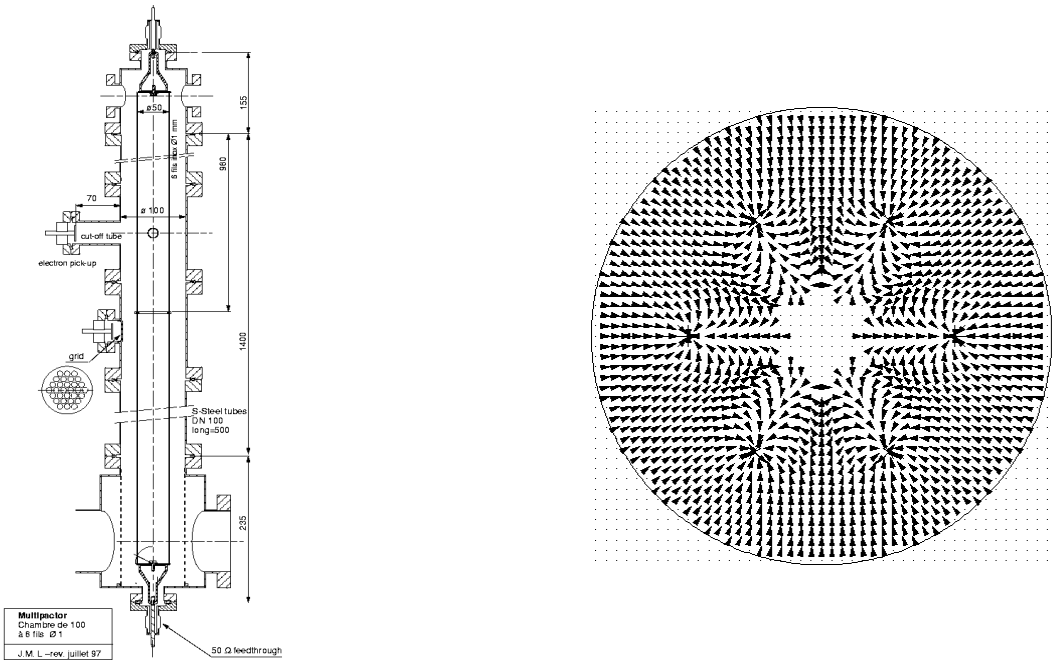

Figure 2-3: *Vector field lines inside the multi-wire chamber.*

To derive the electric field given by the six conductor wires in the multi-wire chamber, I first consider a single infinitely long conductor wire located at the center position of a round chamber. The geometrical form suggests that the Laplacian be expressed in cylindrical coordinates, giving

$$\nabla^2\Phi = \frac{1}{r}\frac{\partial}{\partial r}\left(r\frac{\partial\Phi}{\partial r}\right) + \frac{1}{r^2}\frac{\partial^2\Phi}{\partial\theta^2} + \frac{\partial^2\Phi}{\partial z^2} = 0$$

I assume no variation with the axial z direction, and the cylindrical symmetry eliminating the variations with angle ϕ. Thus, the previous equation reduces to

$$\frac{1}{r}\frac{\partial}{\partial r}\left(r\frac{\partial\Phi}{\partial r}\right) = 0.$$

Integrating twice the Laplace equation, the potential is given by $\phi(r) = \frac{\lambda}{2\pi\varepsilon_0}\ln\left(\frac{R_i}{r}\right)$, with R_i the wire radius and $\lambda = q/l$ the linear charge of the central conductor. Defining u as the potential difference between the inner and outer conductor, or likewise the central wire potential with respect to the (grounded) chamber wall, is

$$u = \frac{\lambda}{2\pi\varepsilon_0}\ln\left(\frac{R_0}{R_i}\right) \tag{2.1}$$

where R_0 the chamber radius. The electric field produced by the infinitely long charged wire is $E_r = \frac{\lambda}{2\pi\varepsilon_0 r}$ and considering the central wire potential

$$E_r = \frac{1}{r}\frac{u}{\ln\left(\frac{R_0}{R_i}\right)} \tag{2.2}$$

For a charged wire displaced at a radius d, the image charged wire (opposite charge) is placed at a distance $d' = \frac{R_0^2}{d}$. The combination of the two charged wires can be shown to produce a constant potential along the given cylinder of radius R_0; in our case $d = 3cm$ and $d' = 8.33cm$ [9]. The electric field generated by the six equispaced conductor wires at a distance d from the cylinder axis, and the related six image conductor wires placed at a distance d', is given by

$$\vec{E}\,(x, y, t) = \sum_{n=1}^{6} (\vec{a}_n \frac{1}{r_n} - \vec{a}_n^{'} \frac{1}{r_n^{'}}) \frac{u(t)}{5.419} \tag{2.3}$$

where $\vec{a}_n = (\frac{x}{r_n}, \frac{y}{r_n})$ and $r_n = \sqrt{(x - x_n)^2 + (y - y_n)^2}$ are respectively unit vectors and distances of the internal point (x, y) to the $n = 1, 2...6$ conducting wires, while $\vec{a}_n^{'}$ and $r_n^{'}$ are respectively unit vectors and distances of the internal point (x, y) to the $n = 1, 2...6$ image charged wires, $u(t)$ is the potential of the wires and the denominator term is the normalization factor determined by the line integral $\int_{d+R_i}^{R_0} \vec{E}\,(x, y, t)\, d\vec{s} = u(t)$.

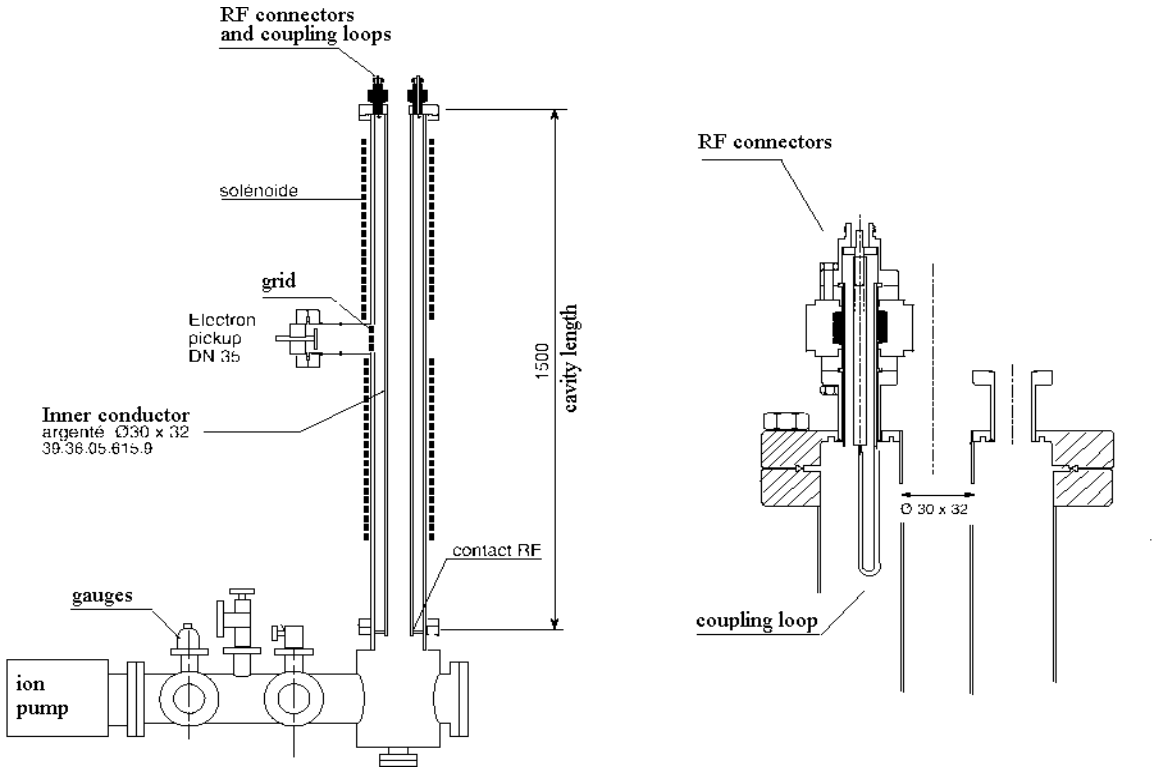

Figure 2-4: *Experimental 100MHz resonant cavity, coupling loops are arranged at the top of the cavity. Coupling loop sketched on the right*

2.2 100 MHz Coaxial Resonant Cavity

2.2.1 Experimental setup for testing multipacting

The objective of using a resonant cavity was to study multipacting with higher electric field level than available in the travelling-wave multi-wire chamber. In this case we can not reproduce the passage of the proton bunches in an accelerator. Nevertheless, the higher electric fields present in the resonant cavity supply higher energies to the electrons, which allows to study the conditioning time (see below) and to compare surface treatments in more detail. The resonant cavity built at CERN, is shown in Fig. 2-4. The electric power generated in a power amplifier is fed to the resonant cavity via a coupling loop.

Two loops are arranged at the top of the resonant cavity; the *coupling* loop to supply the power to the cavity is shown on the right of Fig. 2-4, while the *output* loop is arranged to observe a (small) signal of the electromagnetic fields stored in the cavity. Both loops are placed in the region with the highest magnetic field.

Multipacting occurs in the middle of the cavity where the electric field is maximum, and where a pick-up probe has been arranged to measure the current intensity arising from the electron multiplication resonance. Electrons close to the outer conductor surface,

near the central region of the cavity, are accelerated by the electric field, and subsequently during the second part of the sine wave driven back to the same surface. If the electrons acquire enough energy to produce secondary electrons, these may find the RF field normal to the surface and in correct phase so as to accelerate them and to bombard again the surface. Multipacting could also be generated by electrons bouncing back and forth between the inner and outer conductor surfaces.

2.2.2 Electric and magnetic fields in the resonant cavity

The electrostatic problem of guided waves along uniform systems, including the boundary conditions, results in an electric field purely orthogonal and a magnetic field purely transversal to a perfectly conducting surface.

Three solutions can take place, where z is the wave propagation direction:

- Waves with both the electric and magnetic field orthogonal to the direction of propagation ($E_z = 0$, $H_z = 0$). This solution is called transverse electromagnetic mode (TEM)
- Waves with the electric field, but not the magnetic field, in the direction of propagation ($H_z = 0$). This solution is called transverse magnetic mode (TM).
- Waves with the magnetic field, but not the electric field, in the direction of propagation ($E_z = 0$). This solution is called transverse electric mode (TE).

This is not the only way to represent the possible solutions, but it is useful since the TE, TM and TEM represent a complete system to describe the electromagnetic field, inside a cavity or a wave guide.

In this work, we are only interested in the TEM solution.

Considering the bidimensional electrostatic problem for a coaxial structure [11], the Laplace equation is

$\nabla_t^2 \Phi = 0 \qquad$ or

$\frac{\partial^2 \Phi}{\partial x^2} + \frac{\partial^2 \Phi}{\partial y^2} = \frac{1}{r}\frac{\partial}{\partial r}\left(r\frac{\partial \Phi}{\partial r}\right) + \frac{1}{r^2}\frac{\partial^2 \Phi}{\partial \theta^2} = 0$

with the boundary conditions $\Phi = \Phi_1$ on the inner conductor, $\Phi = \Phi_2$ on the outer conductor. The solution of the Laplace equation can be written

$E_t = \mathbf{e}_r E_r(r,z) \qquad$ with $\qquad E_r(r,z) = \frac{R_i}{r} E_0(z)$

where E_t is the transverse electric field, $E_0(z)$ is the electric field on the inner conductor with radius R_i. Solving Maxwell's equations, it is found that $H_r = 0$, and with $E_\theta = 0$ we obtain the scalar equations

$$\frac{\partial E_r}{\partial z} = -i\omega\mu H_\theta \tag{2.4}$$

$$\frac{\partial H_\theta}{\partial z} = -i\omega\varepsilon E_r \tag{2.5}$$

Differentiating Eq. (2.4) with respect to z, and using Eq. (2.5)

$$\frac{\partial^2 E_r}{\partial z^2} = \omega^2 \varepsilon\mu E_r \tag{2.6}$$

which has as a solution $E_r(r,z) = \frac{R_i}{r}E_0(0)e^{-\gamma z}$ where $\gamma = \sqrt{-\omega^2\varepsilon\mu} = i\beta_w$ is the wave propagation constant (the TEM mode does not exhibit a cut-off frequency, contrary to the TE and TM mode). The magnetic field **H** can be written as

$H_\theta(r,z) = \frac{\gamma}{i\omega\mu}E_r(r,z) = \sqrt{\frac{\varepsilon}{\mu}}E_r(r,z)$ then

$\frac{E_r}{H_\theta} = \sqrt{\frac{\mu}{\varepsilon}} = Z_w$

with Z_w the wave impedance, depending only on the characteristics of the medium. The total current flowing on the internal conductor is linked to H_θ by $I = 2\pi r H_\theta$ and thus

$E_r = Z_w H_\theta = \sqrt{\frac{\mu}{\varepsilon}}\frac{I}{2\pi r}$

Like the current, it is possible to define the potential between the two conductors

$V = \int_{R_i}^{R_0} E_r = \sqrt{\frac{\mu}{\varepsilon}}\frac{I}{2\pi}\ln(\frac{R_0}{R_i})$

we can define the characteristic line impedance as $Z_0 = \frac{V}{I} = \sqrt{\frac{\mu}{\varepsilon}}\frac{1}{2\pi}\ln(\frac{R_0}{R_i})$.
From Eq. (2.4) and Eq. (2.5) using the definitions for I and V we obtain

$$\frac{\partial V}{\partial z} = -i\omega\mu\frac{\ln(\frac{R_0}{R_i})}{2\pi}I \qquad \text{and} \qquad \frac{\partial I}{\partial z} = -i\omega\varepsilon\frac{2\pi}{\ln(\frac{R_0}{R_i})}V. \tag{2.7}$$

Setting $Z = i\omega\mu\frac{\ln(\frac{R_0}{R_i})}{2\pi}$, the solutions of the Eqs. (2.7) can be written as a sum of two terms, representing waves propagating in opposite directions

$V = V_+e^{-\gamma z} + V_-e^{\gamma z}$

$I = \frac{1}{Z_0}(V_+e^{-\gamma z} - V_-e^{\gamma z})$.

The electric field must vanish at the cavity boundaries $z = 0$ and l, and thus imposing the condition $V = 0$, we obtain an infinite and discrete number of resonant frequencies given by $\nu = \frac{cn}{2l}$, with $n = 1, 2...\infty$.
The TEM-mode fields in standing wave (SW) operation are given in the cylindrical coordinates (r,θ,z), by the formulae

$E_r(x,\varphi) = \frac{V}{2r\ln\left(\frac{R_0}{R_i}\right)}(\cos(kz-\varphi) - \cos(kz+\varphi))$

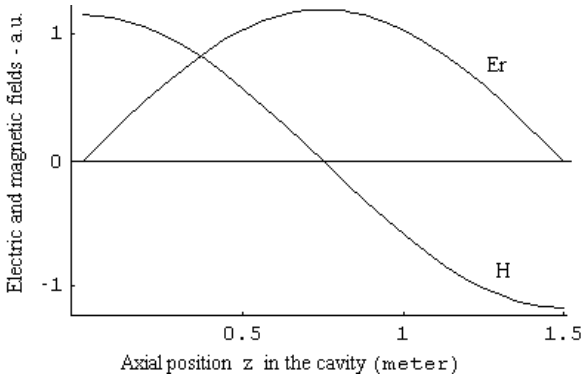

Figure 2-5: *Electric and magnetic fields (a.u.) in the* $\lambda/2$ *configuration at resonance frequency* $\nu \simeq 100MHz$

$$B_\theta(x,\varphi) = \frac{V}{2cr\ln\left(\frac{R_0}{R_i}\right)}(\cos(kz-\varphi)+\cos(kz+\varphi))$$

where $k = \omega/c = 2\pi/\lambda$, and V is the potential difference between the two conductors.

In our case $l = 1.5\ m$, the first harmonic $n = 1$ occurs at $\nu \simeq 100MHz$. Thus, when operating at $100MHz$, the wavelength is $\lambda = 2l$. The resonant cavity is said to operate in the $\lambda/2$ configuration. The correspondent electric and magnetic fields are shown in Fig. 2-5.

Let us assume that the surface is a perfect conductor without holes. Then taking a closed surface Σ delimiting a section of the cavity, inside the perfect conductor, where the electric and magnetic fields vanish, then the complex Poynting vector $S = \frac{1}{2}E \times H^*$ through Σ must also vanish. Thus,

$$-\tfrac{1}{2}\oint_\Sigma \mathbf{S}\cdot\hat{\mathbf{n}}\ d\Sigma = P_p + 2i\omega(W_H - W_E) = 0$$

where P_p represents the dissipated power inside the cavity, W_H and W_E the average stored electric and magnetic energies respectively, and $\hat{\mathbf{n}}$ is the normal to the surface Σ, pointing outwards. This equation shows that an electromagnetic field can exist only if $P_p = 0$ and $W_E = W_H$.

The quality factor Q of a resonator (figure of merit)

The design of cavity resonators, as they are commonly used for particle accelerators, determines their efficiency by concentrating the field in the region of the beam, and by storing energy. The most important characteristic number for a cavity is its 'quality factor' Q, which is defined as $Q = \frac{\omega_0 W}{P_p}$ where $W = W_E + W_H$ and ω_0 is the resonant frequency. In a closed cavity the power loss will be equal to the rate of change of the stored energy, $P_p = -\frac{dW}{dt}$, thus the decay of the stored energy

$$W = W_0 e^{-\frac{t}{\tau_W}}$$

where $\tau_W = \frac{Q}{\omega_0}$ is the decay time of the stored energy. The fields inside the cavity have a damped sinusoidal variation with time

$$E(t) = E(0) e^{-\frac{t}{2\tau_W}} e^{i\omega_0 t}$$

and since $W \propto E^2$ it can be seen that the decay time of the electric and magnetic field is twice the decay time of the stored energy.

Coupling to the cavity

The types of electromagnetic waves that may exist have been discussed without specifically analyzing ways of exciting these oscillations. Some means of coupling electromagnetic energy into and out of the resonator must be provided. The most commonly used methods for exciting waves in waveguides or cavities are:

- Introduction of a conducting probe or antenna in the direction of the electric field lines, driven by an external transmission line
- Introduction of a conducting loop with plane normal to the magnetic field lines
- Introduction of a pulsating electron beam passing through a small gap in the resonator, in the direction of the field lines

The inductive coupling is obtained by arranging a loop inside the cavity intercepting the magnetic field lines. Introducing the coupling loop alters the field distribution but in our case this field configuration is not appreciably modified with respect to the isolated cavity. The *coupling* loop has an area which is usually larger than the one of the *output* loop, which extracts only a small part of the electromagnetic fields stored in the cavity.

Part III

Experiments with a Traveling-Wave test chamber and a 100 MHz resonant cavity

Chapter 3

Multipacting conditions

Introduction

The multipacting phenomena have been studied previously at CERN by means of two computer simulation codes which were used to estimate the heat load in the LHC beam screen: one code developed at LBL [12] and one developed at CERN [13][14]. Simulations have shown that multipacting has a strong dependence on the proton beam parameters. For an LHC-type beam discussed in Chapter 1, the parameters are such that electron multipacting driven instabilities can occur. For this reason an extensive programme of experimental work and computer simulations of electron multipacting has been initiated at CERN.

In this work I have investigated beam-induced multipacting by means of the travelling-wave multi-wire chamber set-up, presented in Chapter 2. The advantage of this travelling wave system, with respect to the simpler standing wave system, is that the secondary electrons close to the wall are accelerated by the electric field and they subsequently drift in the field free period between pulses and thus simulates more closely the phenomenon as occurring in the LHC.

The system gives very clear evidence of a multipacting behaviour which is sensitive to the pulse parameters, i.e. to the proton beam parameters in the LHC accelerator. The multipacting dependence on the RF pulse parameters, have been determined experimentally in the multi-wire chamber setup. To validate the LHC computer simulation code, the program used for LHC has been adapted to the travelling wave experimental set-up, and new simulations have been performed with the multi-wire chamber geometry.

In the present Chapter, a model to explain the multipacting dependence on the RF pulse parameters in the multi-wire chamber will be compared with the results obtained with the experimental system. The Chapter is divided in three parts: multipacting model, experiments and simulations.

The proposed theoretical model describes the electron cloud build up, and is presented in section 3.2. The experimental results, related to the multipacting dependence on the RF pulse parameters (amplitude, width and period) are discussed in sections 3.3.1 and 3.3.4. In section 3.4 the results of the simulations, obtained with the LHC computer simulation code (adapted to the specific geometry of the experimental setup) will be compared with the experimental results.

3.1 Experimental setup general overview

In order to investigate the beam-induced multipacting, a travelling-wave multi-wire chamber has been designed and built to simulate the electric field produced by a bunched proton beam. In this system, the beam bunches are reproduced by short rectangular RF pulses applied to six equispaced parallel wires inside a 1.4 m long stainless steel vacuum chamber of 100 mm diameter.

The experimental setup is shown in Fig.3-1.

The electric field is produced by an RF pulse generator and applied, via an amplifier, to six parallel wires located inside the experimental chamber. The RF power is then adsorbed by two line loads arranged immediately after the multi-wire chamber.

In this travelling wave configuration the pulsed electric field simulates closely the electric field generated by a proton bunched beam in a synchrotron accelerator.

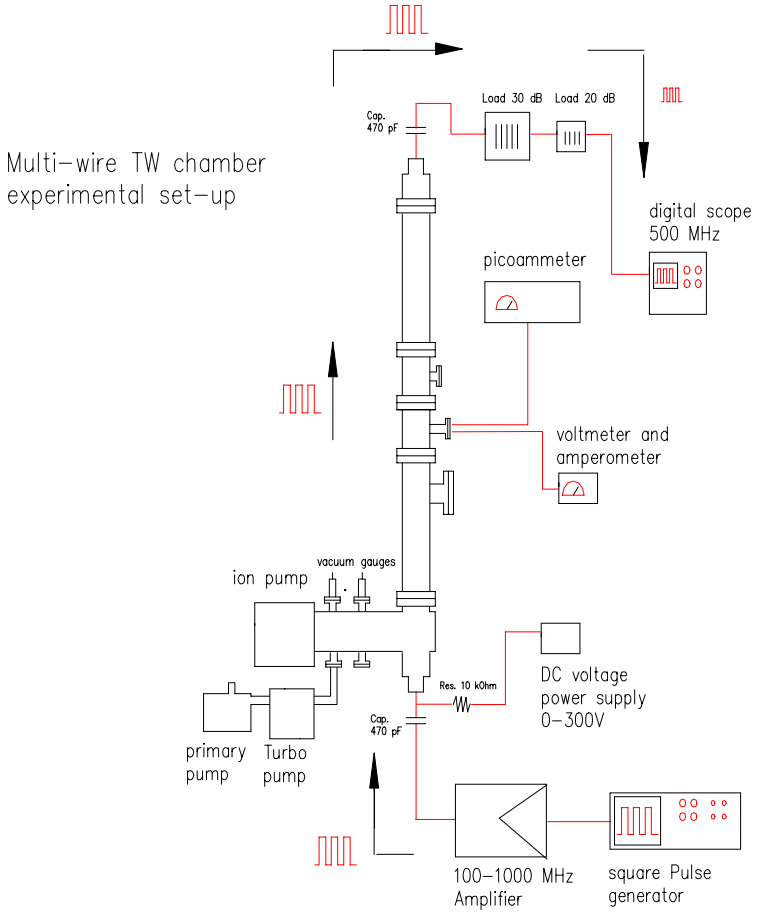

Figure 3-1: *Travelling-wave configuration to simulate the passage of a proton bunched beam in a synchrotron accelerator by a train of RF pulses.*

The output from the RF pulse generator ranges typically from 50 to 400 mV. The signal is amplified to up to $210V$ peak to peak, by the power amplifier; pulses are typically in

the range from 3 to 20 ns width with a 20 to 100 MHz repetition rate. Since the power amplifier has a 1-1000 MHz frequency band, the DC component of the RF pulse spectrum is suppressed at the level of the amplifier output (the RF signal is "DC free", i.e. positive and negative signal - see appendix A). A displacement DC voltage, ranging typically from 0 to 200 V, has been applied to the wires in order to shift the pulses by the desired voltage.

The RF signal is sent to the multi-wire chamber which has been designed to match as closely as possible the 50 Ohm line impedance, in order to avoid undesired reflections along the system (the measured impedance is described in Chapter 2).

The output power from the chamber is adsorbed by two line loads, of respectively 30 dB and 20 dB attenuation, and then sent to the oscilloscope.

3.2 A model for multipacting in the TW chamber

Introduction

Electrons close to the chamber wall are accelerated towards the center of the travelling-wave multi-wire chamber by the RF pulsed electric field. They may reach the opposite side of the chamber and produce secondary electrons if their energy is above the threshold for secondary emission. If these secondary electrons are not returned to the surface before the next pulse arrive, they will be accelerated and hit the surface with sufficiently high energy to cause the emission of new secondary electrons. This process will grow with time if the electrons remain in phase with the radio-frequency pulses and if the secondary electron yield is greater than 1.

In this section we present a model for multipacting in the multi-wire chamber. The model has been studied to explain the multipacting dependence on the RF pulse parameters measured experimentally. To validate the model I integrate the equations of motion for one *reference* electron in the multi-wire chamber and determine when multipacting occurs by varying the pulse parameters. The *reference* electron has $5eV$ initial energy, average energy of the secondary electrons.

The multipacting *conditions* have to be fulfilled in order to get the electron multiplication. Some simplifying *assumptions* considered in the model will be discussed in more detail below.

Multipacting conditions

There are two conditions for multipacting to occur: one based on kinematic considerations, and one based on energy considerations.

1. **Kinematic condition**: for an electron to be in phase with the RF field, it must be emitted from the surface in coincidence with the pulse at the time P_1 (see Fig. 3-2) and it has to travel across the vacuum chamber in one RF period. The condition for the electron velocity reads $\overline{v} = \frac{2R_0}{T}$ or equivalently for the average energy

$$\bar{E} = \frac{1}{2e} m_e (\frac{2R_0}{T})^2 \tag{3.1}$$

where R_0 is the chamber radius and T the RF pulse period. If the electron average energy is much larger than $\bar{E}$, the electrons will hit the opposite wall too early (point A in Fig. 3-2). In this case, the electron is said out of phase with respect to the RF and no multipacting can take place. If the electron average energy is lower than $\bar{E}$, the electron will not hit the wall before the passage of the next pulse and therefore, will not contribute to the multiplication. The condition of Eq. (3.1) is plotted on the *left* side of Fig. 3-3 for the case of the multi-wire chamber.

2. **Energy condition**: The secondary emission yield (SEY or δ) from the chamber surface is a function of the electron impact energy. The typical dependence for metals [15] is shown in Fig. 3-4; in particular E_1 and E_2 are the energies corresponding to $\delta = 1$, and $E_{\max}$ corresponds to $\delta_{\max}$. Experimentally the energy value E_1, for which $\delta(E_1) = 1$, is very sensitive to the surface composition of the first monolayers. For an "*as received*" sample E_1 can vary between 20eV up to 100eV depending on the surface conditions, cleaning methods, and exposition to air [16]. The theoretical curve shown in Fig. 3-4 is not precise in the energy range $0 \div 100eV$, while for higher energies it agrees better with the experimental data. In the model I will assume $E_1 \simeq 39eV$ for the stainless steel vacuum chamber surface. This value has been deduced from measurements of the energy spectrum (see next Chapter 4, Fig. 4-6). The condition to achieve $\delta(E_{imp}) \geq 1$ on the energy is given by

$$E_{imp} \geq E_1 \, [39eV] \tag{3.2}$$

This condition is necessary to get electron multiplication.

Assumptions:

- During multipacting, all the electrons move in the chamber closely packed at the same radial position, see Fig. 3-5, see also Fig. 3-21 below. Therefore, the radial distribution of the electrons in the chamber is assumed to be a Dirac delta distribution in r, $\delta(r)$, rather than a uniform distribution. As a consequence, I assume that all of them hit the wall in phase with the RF at the times labelled P's in Fig. 3-2.

- If an electron hits a central wire it is considered to be lost, as it produces secondaries with low energy which are attracted back to the wire from the positive potential. I assume that during multipacting the electrons tend to cumulate along the line between two wires. In the model I allow the starting *reference* electron to come out from the surface at the instant corresponding to the point P on the right-hand side of Fig. 3-3 (middle point between two wires) and experiencing a straight trajectory. This leads to one-dimensional harmonic oscillator problem.

These assumptions have been inferred from the results of the LHC multipacting simulation program which has been adapted to the multi-wire chamber geometry, see appendix C.

To validate the model I integrate the equations of motion for an electron in the multi-wire chamber, taking into consideration the previous assumptions. I determine whether multipacting occurs according to the *conditions* discussed above, and I compare the theoretical with the experimental results.

The electric field in the presence of six charged lines (and six oppositely charged image lines) in the vacuum chamber is given by Eq. 2.3.

An ideal RF pulse shape (perfectly rectangular) is shown in Fig. 3-6, where the DC voltage applied to the wires is taken into account. When I speak about the bias-voltage

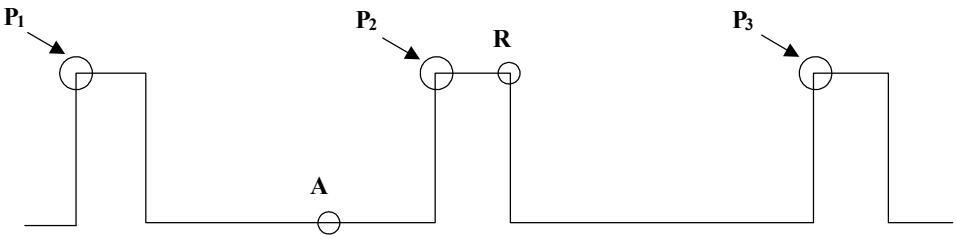

Figure 3-2: *Electrons emitted in P1 should hit the opposite surface in phase with the RF pulse at P2, while if electrons hit the surface at "A" or "R" they get out of phase with the RF pulses and no resonance can take place.*

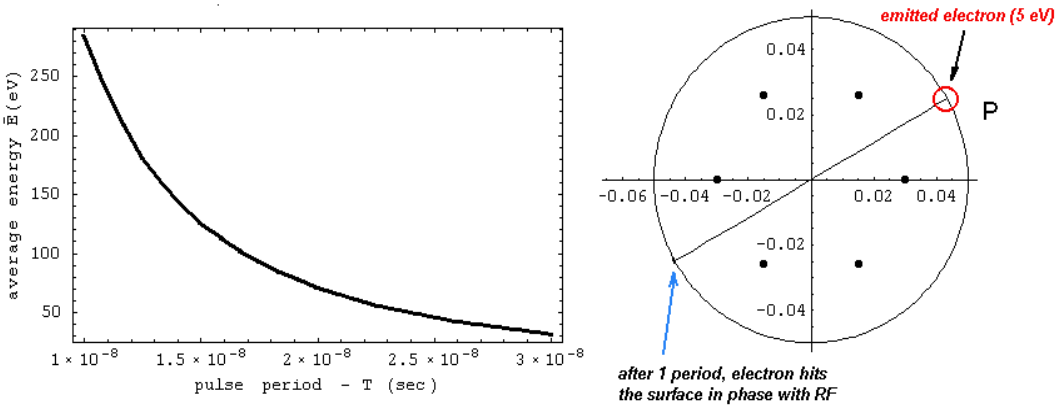

Figure 3-3: Left*: Kinematic condition, average energy $\bar{E}$ as a function of the pulse period* Right*: Trajectory of the reference electron in the multi-wire chamber.*

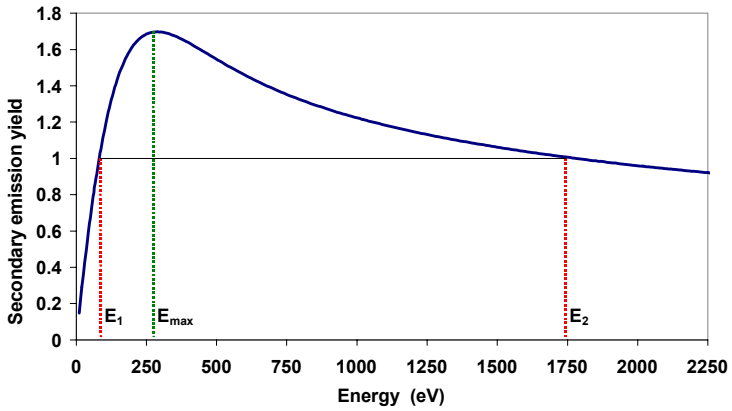

Figure 3-4: *Secondary emission yield (theoretical curve) as a function of the electron energy for* $\delta_{\max} = 1.7$

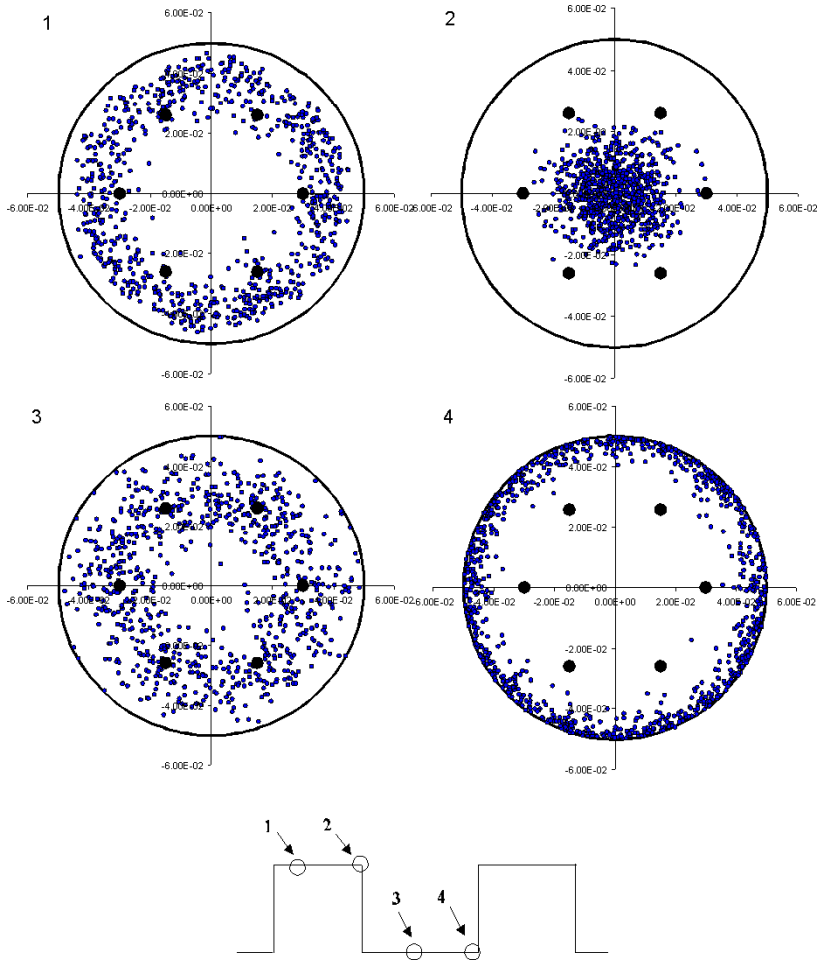

Figure 3-5: *Consecutive images during one period RF. Electrons move in the chamber closely packed at the same radial position.*

and the squared potential I refer respectively to the constant part and the upper squared part of the RF signal; I use a rectangular pulse both for the theoretical studies and for the *simulations*.

Considerations on how to set the correct pulse amplitude for the model and for the simulations are given in the appendix B.

3.2.1 Equations of motion for the reference particle

In this section I will discuss the bi-dimensional problem, where the x-y transverse plane of the multi-wire chamber is considered ($\ddot{z} = 0$). Moreover, the magnetic field has been neglected, since the velocity of the electron inside the multi-wire chamber is low and $\vec{v} \times \vec{B} \simeq 0$.

Taking into account the considerations given in section 2.1.2, the Lagrangian for a *reference* electron in the multi-wire chamber is $L(q_k, \dot{q}_k, t) = T(q_k, \dot{q}_k, t) - V(q_k, t)$, where

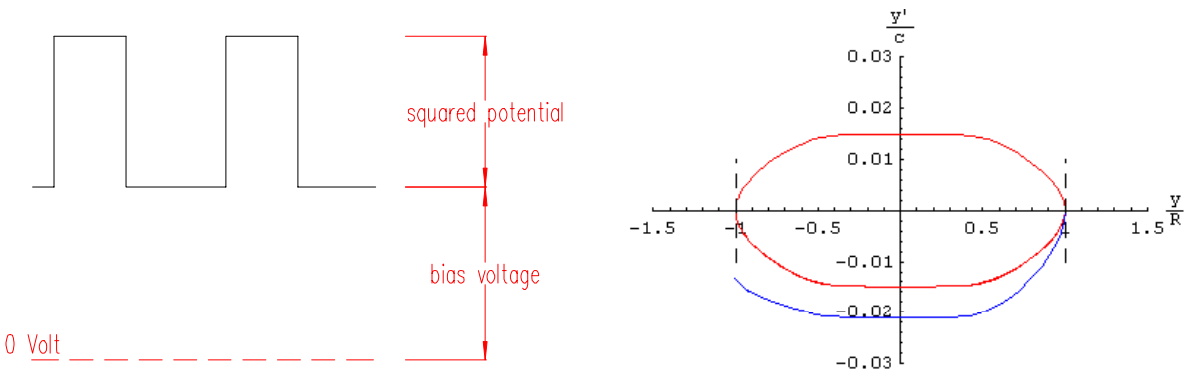

Figure 3-6: *Signal applied to the wires composed of rectangular RF pulses superimposed on a DC bias-voltage.*
Left: Square pulse used in the simulations, the bias-voltage is the displacement to ground. Right: *Phase space (normalized* $\frac{y'}{c}$, $\frac{y}{R_0}$*) for an electron emitted at point* $(0, R_0)$*. The close trajectory corresponds to the case of a constant potential applied to the wires (harmonic oscillator potential), while in the case of a square pulse the trajectory ends when the electron hits the wall. The projection on the* y'/c *axis gives the impact velocity.*

the potential energy is given by $V(q_k, t) = q\phi = -e\phi(q_k, t)$ when the magnetic field is neglected. The kinetic energy is equal to $T = \sum_k \frac{m\dot{q}_k^2}{2}$ and the canonical momenta $p_k = \partial L/\partial \dot{q}_k = m\dot{q}_k$. In x-y coordinates we have $T = \frac{m\dot{x}^2}{2} + \frac{m\dot{y}^2}{2}$, $p_x = m\dot{x}$ and $p_y = m\dot{y}$.

The Hamiltonian is given by

$$H(q, p, t) = \sum_k p_k \dot{q}_k - L(q, \dot{q}, t) = \frac{p_x^2}{2m} + \frac{p_y^2}{2m} - e\phi(x, y, t)$$

and the Hamilton's equations:

$$\dot{q} = \frac{\partial H}{\partial p} \qquad \dot{p} = -\frac{\partial H}{\partial q}.$$

For x-y coordinates

$$\dot{x} = \frac{\partial H}{\partial p_x} = \frac{p_x}{m} \qquad \dot{p}_x = -\frac{\partial H}{\partial x} = e\frac{\partial \phi(x, y, t)}{\partial x} \tag{3.3}$$

leading to the Lorentz equation in the Newton formalism:

$$\ddot{x} = \frac{e}{m}\frac{\partial \phi(x, y, t)}{\partial x} = -\frac{e}{m}E_x$$

Taking into account Eq. (2.3)

$$\ddot{x} = -\frac{e}{m}E_x = -\frac{e}{m}\sum_{n=1}^{6}(\frac{x}{r_n^2} - \frac{x}{r_n'^2})\frac{u(t)}{5.419}$$

similarly for y

$$\ddot{y} = -\frac{e}{m}E_y = -\frac{e}{m}\sum_{n=1}^{6}(\frac{y}{r_n^2} - \frac{y}{r_n'^2})\frac{u(t)}{5.419}$$

an electron emitted at point (0,R_0), experiences a straight trajectory crossing the chamber. If a constant electric potential is applied to the wires the electrons oscillate back and forth like in a harmonic oscillator potential, without being able to hit the wall[1]. *Left* of Fig. 3-6 shows the normalised phase space ($\frac{y'}{c}$ and $\frac{y}{R}$) calculated from Eqs. (3.3) for an electron emitted at point (0,R_0).

3.2.2 Multipacting as a function of the pulse width and period

The final position of the electron after one RF pulse period is determined by integrating the equations of motion for *a reference* electron. I define the factor f, called impact fractional time of the period as

$$f = \frac{\varphi(t_{imp})}{2\pi}$$

where the phase of the RF pulse is given by $\varphi(t) = \frac{2\pi t}{T}$, $t = 0$ represents the beginning of the rectangular pulse and the time at which the electron is emitted from the surface, and t_{imp} is the instant at which the electron hits the opposite side of the chamber. Thus, $f = 1$ represents an electron hitting the wall exactly in phase with the RF pulse (corresponding to the kinematic condition of Eq. 3.1).

The radial position of the electron after one pulse period is defined as $r(T)$.

According to the kinematic conditions, the multipacting occurs if the radial position of the reference electron after one pulse period is $r(T) \gtrsim R_0$, implying $f \lesssim 1$.

Considering a fixed amplitude of 140V and the parameters set during the experiment (see below Fig. 3-13), I estimate $r(T)$, the impact energy, and the factor f, as a function of the pulse width.

According to the *right*-hand side of Fig. 3-7 , we get multipacting in a time window equal to the pulse width which ranges from 4.5 to 14 nsec, where $f \lesssim 1$ (or equivalently $r(T) \gtrsim R_0$, see also *left* side of the same figure); the impact energy is always greater than 39eV (i.e. the energy condition for multipacting is verified) as shown in Fig. 3-8[2].

Similarly we consider the set of parameters during the experiment in the case of multipacting as a function of the pulse period (see below Fig. 3-14), as shown on the

[1] Here we assume, for simplicity, an electron emitted with zero energy.

[2] during the experimental measurements a variation of the pulse width can cause $Vmin$ to change, then the effective bias voltage V_b shifts from +90V to +30Volt, while the other parameters,V_a, A, T, are fixed.

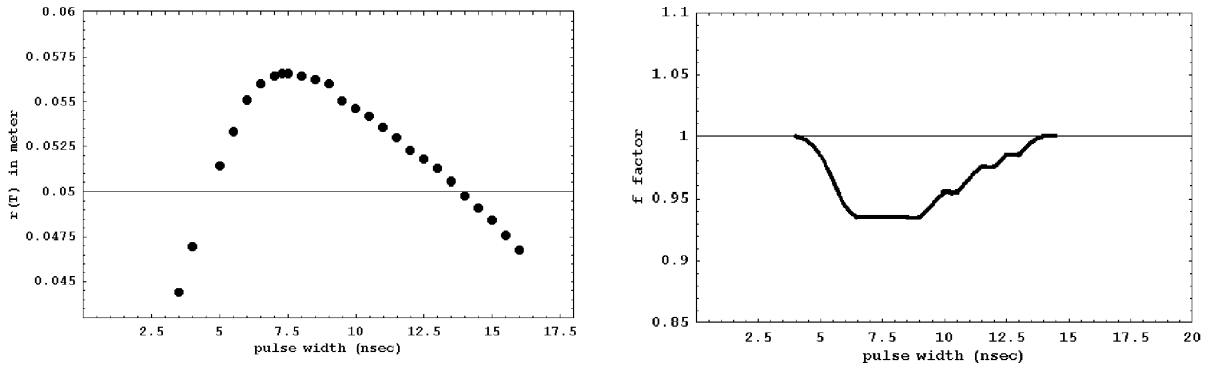

Figure 3-7: *Computed electron radial position at time t=T and related factor f.*
left: r(T) as a function of the pulse width, multipacting occurs if r(T)≥ R_0 (chamber radius $R_0 = 0.05$).
right: fractional factor f as a function of the pulse width.

right-hand side of Fig. 3-9; $f \lesssim 1$ for $T > 19$ nsec (or equivalently $r(T) \gtrsim R_0$, see also left side of the same figure). In this case the impact energy is always greater than the limit given in Eq. (3.2).

On the *right*-hand side of Fig. 3-9 is shown the fractional factor f as a function of the pulse period. If $f \ll 1$ the electron hits the surface too early, out of phase with respect to the RF pulses. In this case, the kinematic condition ceases to be fulfilled, and multipacting stops. An estimation of the lower limit of f for which electron multiplication occurs is obtained by the simulations. The simulation results show the heat load in the experimental chamber as a function of time on the *right*-hand side of Fig. 3-21**.** The heat load on the surface has a repetition rate equal to the pulse period T, meaning that the electrons hit the wall in phase with the radiofrequency pulse and this occurs in a width of 3÷4 nsec of the period (FWHM) of the heat load distribution curves.

As a consequence, an electron emitted in phase with the RF pulse should cross the chamber with a TOF$\sim T \pm 2n$ sec ($T = 20nsec$) in order to contribute to the electron multiplication, corresponding to a fractional factor $f = 1 \pm 0.1$. Thus, multipacting should stop for values of f lower than ~ 0.9.

Multipacting is predicted for a fixed amplitude of 140V and a period of 20 ns, in a window of pulse widths between 4.5 and 14 ns. A similar behaviour is predicted for the same pulse amplitude and a fixed width of 10 ns, in a window of pulse periods between 19 and 21 ns.

Although I have considered only a single 5eV *reference* electron[3], the model is in good agreement with the experimental results.

[3]where a more complete model should take in account the entire energy spectrum of the secondary electrons, resulting in slightly larger windows than the ones predicted here.

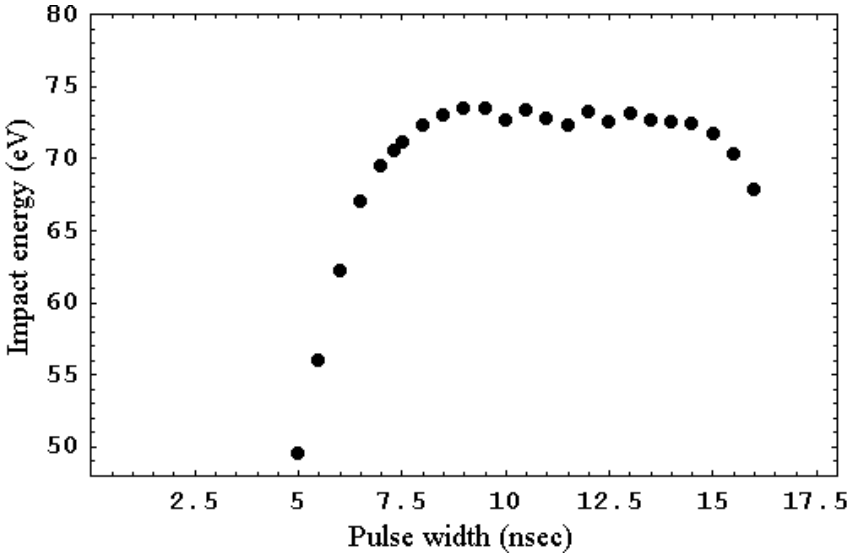

Figure 3-8: *Computed electron impact energy as a function of the pulse period*

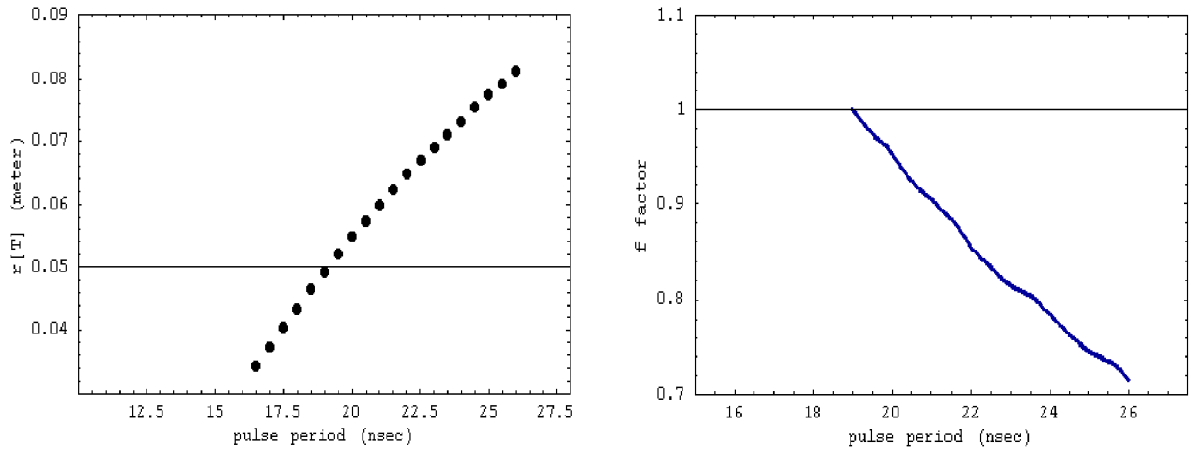

Figure 3-9: *Computed electron radial position at time t=T, and factor f.*
Left*: r(T) as a function of the pulse period.*
Right*: correspondent f fractional factor.*

3.2.3 Multipacting threshold

As discussed in section 1.2, from the LHC model we know that multipacting is mainly a function of the beam intensity and the bunch period [7][17]. The threshold proton beam intensity is given by Eq. (1.9) which gives the beam intensity dependence on the pulse period, or equivalently by Eq. (1.8).

Eq. (1.9) is derived in the kick approximation (the proton bunch passes by before the test charge has started to move, as the bunch duration is 0.25 ns). In the case of the multi-wire chamber, for which the RF pulse width typically ranges between 2 and 20 ns, the kick approximation model would be not correct. Therefore, it is necessary to integrate the equations of motion for the reference electron.

In the experimental travelling-wave chamber the beam intensity of the LHC proton accelerator is simulated by the RF pulse amplitude. The goal is to estimate the threshold pulse amplitude, necessary to trigger multipacting.

In particular, one obtains the threshold by increasing the pulse amplitude until the *reference* electron reaches the opposite side of the chamber in exactly one RF period, satisfying the kinematic condition (3.1), and the energy condition given by Eq. (3.2).

Estimating the pulse amplitude necessary to trigger multipacting as a function of the pulse period, I get a border line, which separates the stable region from the multipacting region. The time of flight of the electron is a function of the pulse amplitude, and thus, the threshold pulse amplitude is directly related to the threshold condition given in Eq. 3.1.

The threshold equations

$$\bar{E} = \frac{1}{2e} m_e (\frac{2R_0}{T})^2 \tag{3.4}$$

and

$$I_{beam} = \frac{4\pi\varepsilon_o m_e c}{e} (\frac{R_p}{T})^2 \tag{3.5}$$

are respectively derived for the multi-wire chamber and for LHC, with the same kinematic condition for the the time of flight of the electron. An experimental validation of the former condition for the experimental chamber would work as validation of the latter for LHC.

In order to define the threshold region, I refer to the set of parameters T and V_b in Fig. 3-18; I will analyse the case of 10 ns pulse width.

The results obtained applying the model are shown in Fig. 3-10 for 5 eV and 10 eV emission energy of the *reference* electron. In the next section, the theoretical results obtained will be compared with the experimental results.

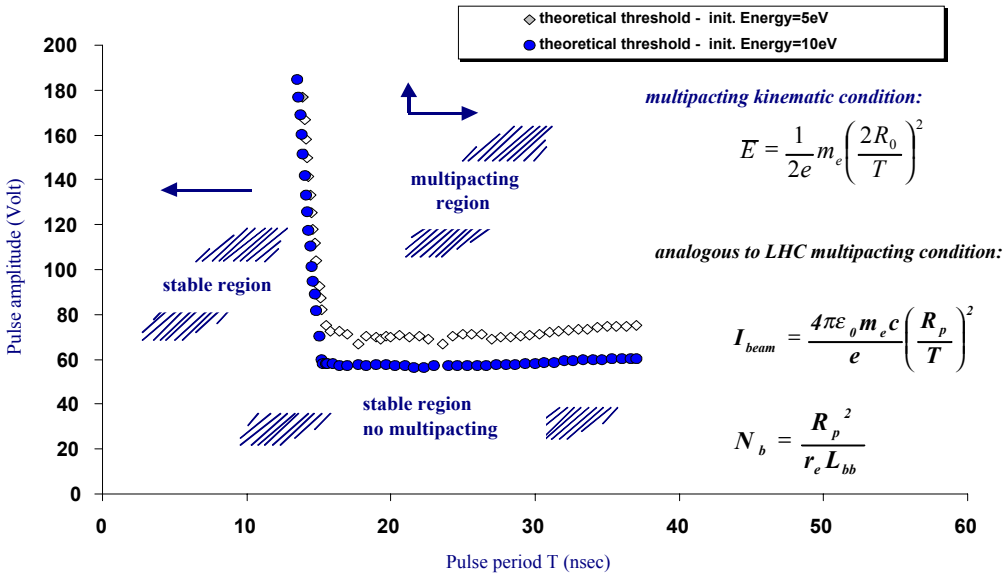

Figure 3-10: *Threshold pulse amplitude as a function of the pulse period, as predicted by calculation in the multi-wire chamber, for different energies of the emitted electron: the pulse amplitude simulates the beam intensity.*

3.3 Experimental results

3.3.1 Multipacting dependence on the pulse parameters: period, width and amplitude

Measurements overview

In the multi-wire chamber, the electrons close to the chamber wall are accelerated towards the center of the chamber by the RF pulse electric field. They may reach the opposite side of the chamber and produce secondary electrons if they have enough energy. The multipacting conditions are met if the next pulse is present at that time and if the secondary electron emission yield is greater than 1.

In the experimental set up, the multipacting build up is detected by the vacuum pressure increase and recorded by a positively (+45 V) biased electron pick-up, consisting of a circular probe in a faraday cup, both are mounted in a ground-shielded tube in the middle of the chamber.

It is possible to measure the dependence of multipacting on the RF pulse parameters, and to relate the multipacting electron cloud to the electron current recorded at the pick-up.

In order to measure the dependence of the multipacting with the four pulse parameters (period, width, amplitude and bias-voltage), measurements were performed varying each

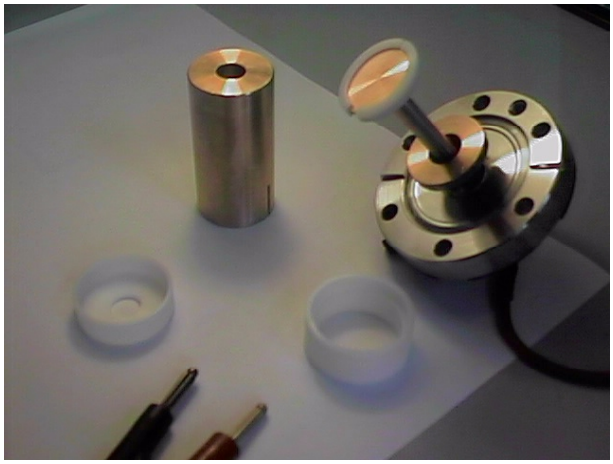

Figure 3-11: pick-up probe (1) and cup (2)

parameter while the others were kept constant[4].

As it will be discussed in next Chapter 5, the electron bombardment can change the surface composition resulting in a "cleaning" effect for this reason each measurement is performed during a short time in order to avoid any possible change of the surface.

The voltage applied to the six wires has a strong effect on the intensity of the electron cloud during multipacting.

As previously discussed a displacement potential typically from 0 to 200 Volt has been applied to the wires which was necessary because the radiofrequency signal at the level of the amplifier output is "DC free". In order to properly simulate the electric field generated by the proton bunches, the applied DC displacement potential shifts the pulses up, until the minimum of the RF pulses coincide with the "zero" potential level of the wall.

Another consideration is necessary:

Under certain conditions[5], the power amplifier output is limited. In order to trigger multipacting it is often necessary to apply a DC voltage to the wires, which shift the lower part of the pulses higher than the "*zero*" voltage level[6].

We define the effective bias-voltage V_b, as the shift of the RF pulses from the zero level (the chamber wall grounded potential)

$$V_b = V_a + \quad | \, Vmin \, | \tag{3.6}$$

where V_a is the DC potential applied to the wires, and $Vmin$ is the minimum voltage of the pulses as measured by the oscilloscope, see Fig 3-12.

[4]Changing one parameter at the pulse generator level, the amplifier gain generally changes and a re-setting of the pulse amplitude has to be achieved each time in order to mantain the pulse shape constant during the measurement.

[5]in case of the pulse width $W \to 0$ or $W \to T$

[6]this surplus potential would not be necessary if the amplifier could supply an higher output power; a wide frequency band amplifier with high output power is difficult to find.

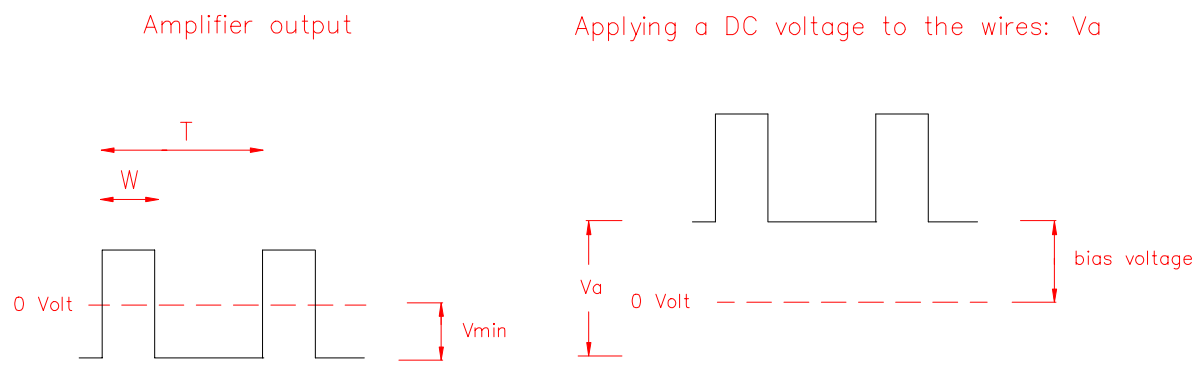

Figure 3-12: Left: *signal otput from the amplifier the RF pulse is "DC free", i.e. positive and negative values are balanced*; $Vmin$ is the minimum voltage of the pulses as measured by the scope.
Right: *applying a DC voltage* V_a *to the wires, the amplitude is shifted up with respect to the 0 volt level. The effective bias-voltage* V_b *is defined as the shift of the RF pulses from the zero-Voltage level (the chamber wall grounded potential)*

3.3.2 Multipacting as a function of the pulse width and period

For a fixed pulse amplitude of 140 Volt and period of 20 nsec, multipacting is observed in a window of pulse widths between 7 and 16 nsec. Fig. 3-13 shows multipacting as a function of the pulse width, where the multipacting electron current at the pick-up probe as a function of the pulse width has been recorded. The bias voltage decreases from 90 to 32 V when varying the pulse width from 3.5 to 16 ns.

A similar behaviour is measured for the pulse amplitude of 140 Volt and a fixed width of 10 nsec, in a window of pulse periods between 18 and 22 nsec, see Fig. 3-14. The bias voltage increases from 54 to 72 V when varying the pulse period from 16.5 to 26 ns.

The range of pulse width where multipacting takes place will enlarge or get narrower if the pulse amplitude increases or decreases, respectively. The multipacting window will also decrease with the decreasing of the secondary electron yield (SEY)[7] of the surface material.

In the two limits $W \rightarrow 0$ or $W \rightarrow T$ $(20nsec)$, multipacting should disappear, as shown in Fig. 3-13, when the pulse width approaches one of these limits the RF voltage becomes constant. When a constant potential is applied to the wires, the electrons oscillate back and forth in the chamber, and they do not strike the wall.

In the case shown in Fig. 3-14, according to the considerations given above, multipacting should disappear at the limit $T \rightarrow W$ $(10nsec)$, but we cannot draw the same conclusion for higher period values. Another possible effect can limit the multipacting: in the case of a long period, the secondary electrons emitted with low energies have sufficient time to cross the chamber and hit the wall before the passage of the subsequent pulse,

[7] SEY of the surface decreases during an electron bombardment

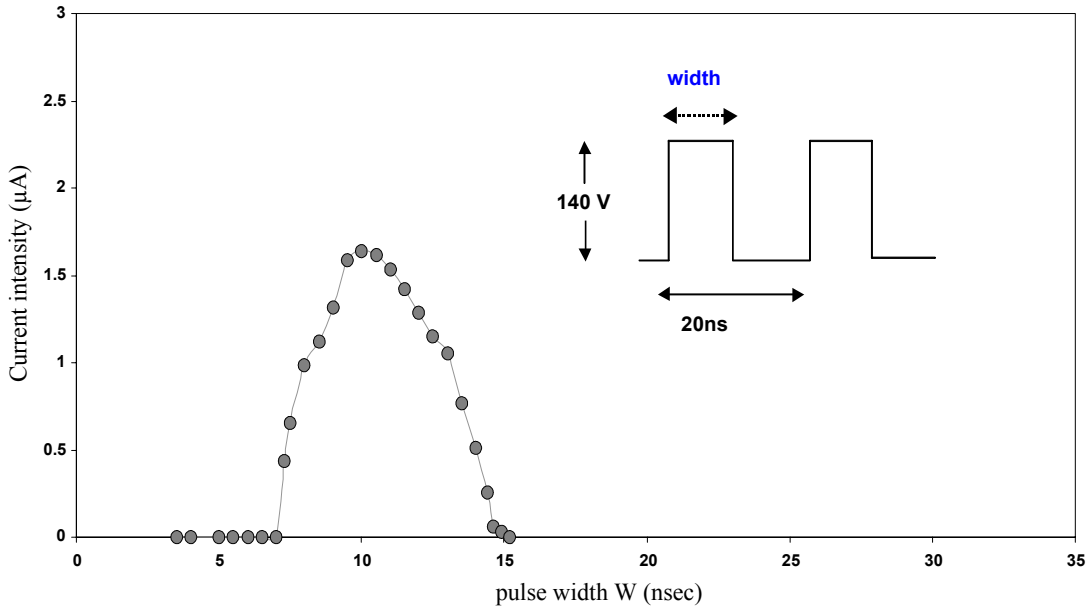

Figure 3-13: Multipacting as a function of the pulse width

and therefore, are lost.

3.3.3 Multipacting dependence on the bias-voltage

By varying the applied DC voltage the whole pulse shape will be displaced. Experimentally, multipacting occurs only in a limited range of the bias-voltage, as shown in Fig. 3-15. The shown measurement has been performed while keeping the other pulse parameters amplitude, period and width fixed.

It is observed that typically, the electron current intensity at the pick-up increases slightly up to a maximum value, after which it decreases abruptly to zero and multipacting can no longer be observed for higher V_b.

The typical behaviour of Fig. 3-15, has two possible explanations:

- when increasing V_b, the electron velocity increases and the TOF decreases. If the TOF is further below one pulse period, multipacting stops (kinematic condition).

- The second explanation is related to the space charge field arising from the secondary electrons created near the surface. In this case the space charge will effectively decelerate other secondary electrons when they are moving away from the wall and push them back onto the wall, thus resulting in a lower effective SEY. As a higher bias-voltage is applied to the wires, secondaries are accelerated faster away from the chamber surface towards the center of the chamber, attracted by the wires, with a consequent reduction of the space charge field near the surface and an increasing number of secondary electrons coming out from the wall. This effect takes place

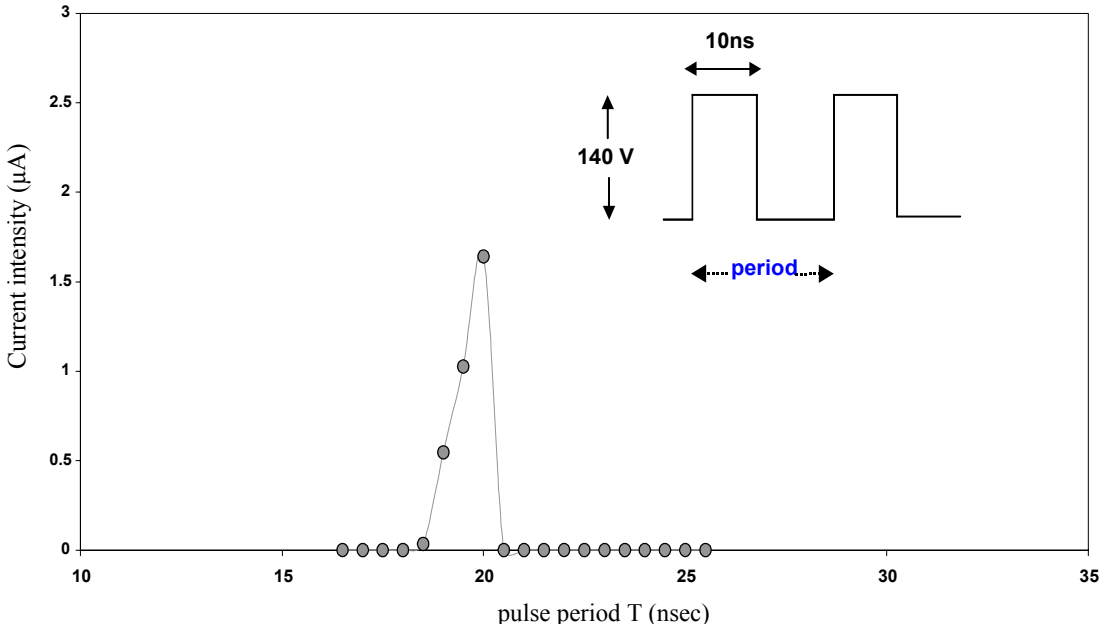

Figure 3-14: Multipacting as a function of the pulse period

until the resonance conditions are no more met and then multipacting will again stop.

If the pulse period is changed, multipacting takes place for a different window of the bias-voltage.

The lowest and the highest values of V_b where multipacting occurs while varying the pulse period, are shown in Fig. 3-16. Multipacting is confined in the region between the upper and lower curves. Note that for T=20nsec the upper and lower limits correspond to those of Fig. 3-15.

Fig. 3-16 may be explained by assuming that: as the RF pulse period increases the bias-voltage must decrease to result in a lower average energy of the electrons such as to remain in phase with the radiofrequency.

3.3.4 Resonance threshold

As previously discussed in section 3.2.3, the threshold beam intensity for multipacting in LHC is given by Eq. (3.5). The threshold intensity dependends on the bunch to bunch period, as T^{-2}.

I have determined experimentally the threshold RF pulse amplitude as a function of the pulse period which is necessary to trigger the electron multiplication resonance in the chamber. Comparing the experimental results with the computation provides a confirmation of the model adopted for LHC.

Experimentally the pulse width (W) and period (T) have been maintained constant, while the pulse amplitude and the bias-voltage have been varied in order to search for

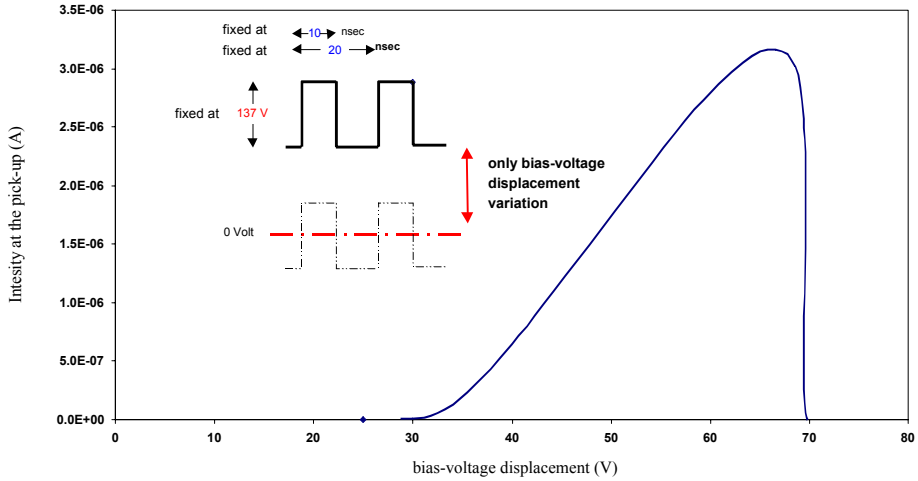

Figure 3-15: Typical effect of the bias-voltage on the intensity of multipacting

the exact pulse parameter values A, V_b for which electron multiplication starts in the chamber. The threshold amplitude is clearly determined when an electron current is suddenly recorded at the pick-up by the picoammeter and the pressure inside the cavity increases rapidly[8,9].

3.3.5 Mapping the multipacting regions in the multi-wire chamber

A map of the regions is shown in Fig. 3-17 corresponding to four fixed pulse widths. Stable regions are situated under the curve where no electron multiplication occurs. Fig. 3-17 must be read together with Fig. 3-18, which gives the value of V_b by which the pulses should be displaced in order to trigger the electron multiplication[10].

The experimental results are compared with the theoretical ones in Fig. 3-19. For pulse periods up to 25 nsec the theoretical curves fits rather well the experimental results, especially for 10eV electron emission energy.

For periods larger than $25 \div 30n$ sec a mechanism of particle loss starts to become important. Between two pulses the faster secondary electrons have sufficient time to cross the vacuum chamber and to hit the wall [11] before the arrival of the subsequent pulse; since their energy is too low to produce secondary electrons they are lost. As a consequence as the pulse period is increased a larger part of the secondary energy in the high energy tail

[8] with a precision of 1 pA; it has to be remarked that the current of a few pA recorded for a short period of time has a negligible effect on the surface cleaning

[9] The method described here consists in increasing the bias-voltage in order to determine the starting point of multipacting. The dependence of V_b on the pulse period is shown in fig.3-18.

[10] Fig.3-18 is equivalent to Fig.3-16, but the two bias-voltage limit curves in Fig.3-18 are indistinguishable

[11] a 30 eV electrons cross the vacuum chamber in ca. 30 nsec.

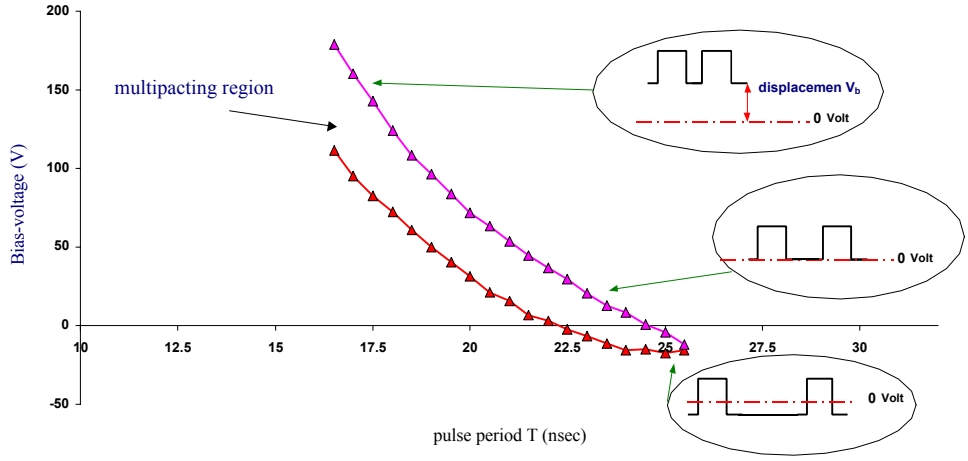

Figure 3-16: *Bias-voltage limits for multipacting; experimentally multipacting occurs within the region between the top and lower curves.*

of the distribution is lost [12].

In the experiment this effect shows up by the need of an increased power, i.e. higher pulse amplitude, to trigger the electron multiplication. This mechanism of particle loss has not been taken into account in the *single-particle* model, but in this range of periods the experimental results agree better with theoretical results for low electron emission energy, see Fig. 3-19.

As a conclusion: in the range of low pulse periods multipacting is triggered by the more energetic secondary electrons, while for higher pulse periods the electrons of the low energy tail of the distribution become more important.

In spite of the fact that for large pulse periods a particle loss mechanism should be taken into account, the model explains quite well the experimental results.

One may conclude that the agreement between the model and the experimental results, gives a good level of confidence on Eq. (3.5) for LHC.

[12] energy distribution of the emitted electrons

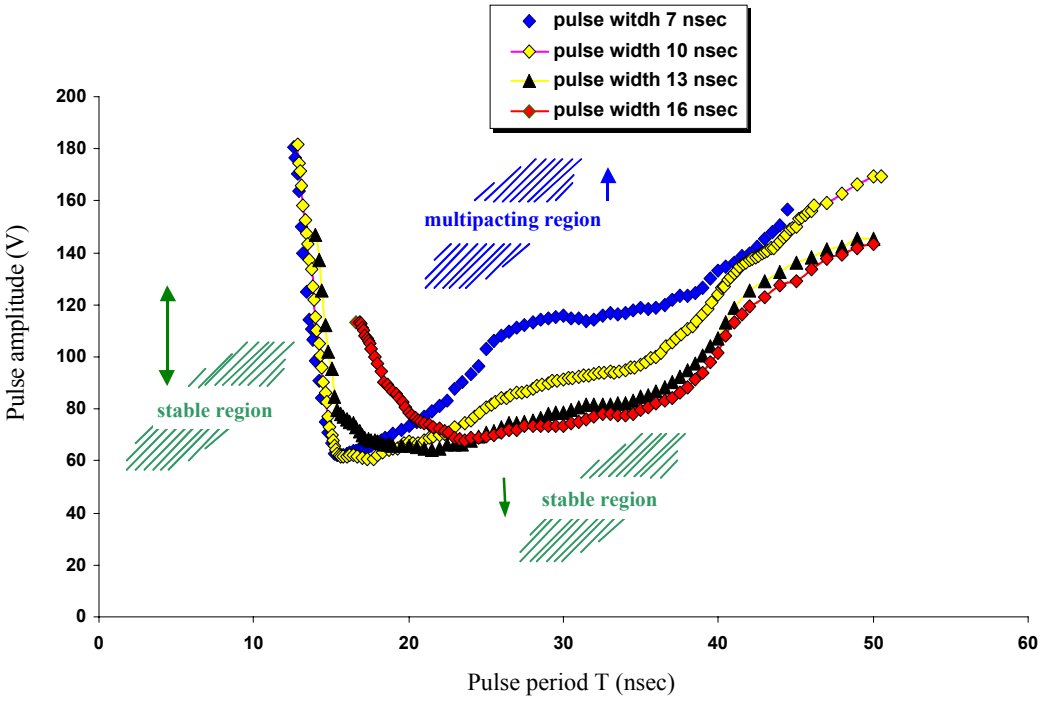

Figure 3-17: *Multipacting regions in the multi-wire chamber*

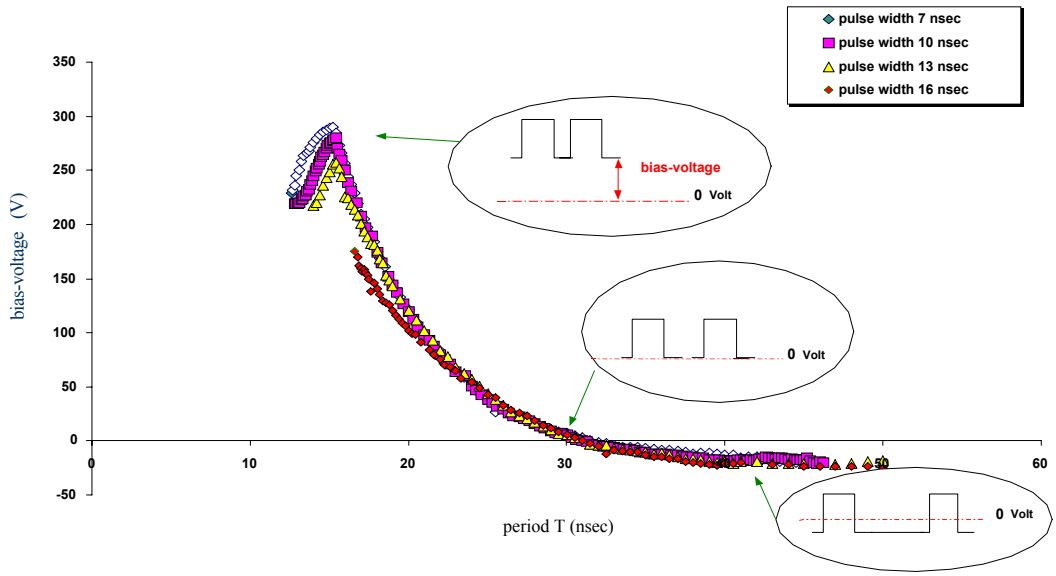

Figure 3-18: *Bias-voltage necessary to trigger multipacting in the multi-wire chamber as a function of the pulse period T*

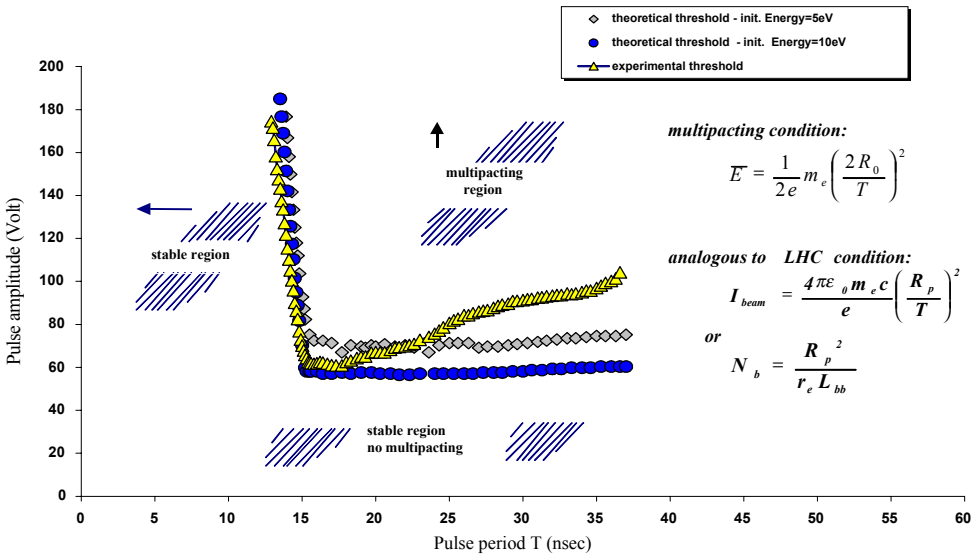

Figure 3-19: *Multipacting region for pulse width 10 nsec, experimental results and theoretical model for 5 and 10 eV initial electron energy.*

3.4 LHC multipacting computer simulations

To explain the experimental results in the multi-wire chamber, *simulations* have been performed with the LHC multipacting computer code [14]. In the simulation program the electrons are modelled by 1000-2000 macro-particles. A macro-particle is used to simulate a defined number of electrons; initially each macro-particle carries the same charge corresponding to the number of electrons; the program solves the equations of motion, and once a macro-particle reaches the wall of the vacuum chamber the program calculates the secondary emission yield of the incident macro-particle, as a function of its energy and incident angle θ with respect to the surface normal; the charge of the emitted macro-particle is then given by the product of the initial charge and the secondary emission yield $\delta(E, \theta)$. This process is iterated for (typically) 100 pulse periods.

In the model I integrated the equation of motion for only *one reference* electron during *one* pulse period and impose that the multipacting conditions are fulfilled.

3.4.1 Simulation results

Simulations for LHC, obtained with the computer code, have shown that multipacting in the proton accelerator has a decisive dependence on the proton beam parameters like the intensity, the bunch length and period.

Part of the thesis work has consisted in validating the multipacting simulation program used for LHC. The program has therefore been adapted to the travelling wave experimental set-up, and new simulations have been performed with the multi-wire chamber geometry. In order to estimate the level of confidence of the LHC computer program I compare in

this Chapter the experimental results related to multipacting as a function of the pulse width and period, with the simulations.

The simulation code gives the following relevant output parameters: number of electrons in a length of an LHC dipole magnet (14.2 meters) vs time. The heat load in W/m due to the incidence of the electrons on the chamber surface, the energy spectrum of the electrons hitting the wall, the average secondary yield of the electrons at the wall and finally the horizontal electron distribution.

After setting the experimental input parameters, (refer to Fig. 3-13 and 3-14), I have run the program and analyzed the dependence of multipacting on the pulse width and on the pulse period.

Here are listed typical values of the experimental input parameters:

Number of macro-particles initially generated	2000
Correspondent starting number of electrons in the chamber	10^{11}
Energy distribution of the seconday electrons - σ_{se}	4.4 eV
Number of rf pulse passages, during which we generate particles	20
Secondary emission yield (SEY)	2.39
E_{max}, energy at which SEY is maximum	350 eV
How often the space charge field is calculated between two pulses	10
Total number of rf pulse passages during a simulation	100
rf pulse amplitude V_{p-p}, V_b , W, T	...

During a simulation run the program generates 2000 macroparticles for the first 20 pulse passages. In the case of multipacting the electron cloud is self-sustained, and the initial number of electrons will increase until an equilibrium is reached, see next Chapter 4. If multipacting does not occur the number of electrons initially generated will decrease exponentially with time.

As an example, Fig. 3-20 shows the number of electrons (LHC bending magnet) as a function of time, related to the RF pulse parameters

left of Fig. 3-20		*right* of Fig. 3-20	
V_{p-p}	140 $Volt$	V_{p-p}	140 $Volt$
V_b	63.4 $Volt$	V_b	63.4 $Volt$
W	10 ns	W	10 ns
T	**20** ns	T	**30** ns

.

Multipacting occurs clearly in the case of T=20 ns, but not for T=30 ns.

The simulation program calculates the heat load per meter of chamber.

In order to compare the simulation results with experimental data, the calculated heat load has to be translated in current per area equal to the pick-up electrode surface[13]. This method gives the possibility of verifying the validity of the heat load calculated from the code, and of validating the simulation results obtained for LHC (see Chapter 4).

[13]The number of electrons in Fig. 3-20 cannot be used to estimate the current at the pick-up because many electrons are lost on the wires.

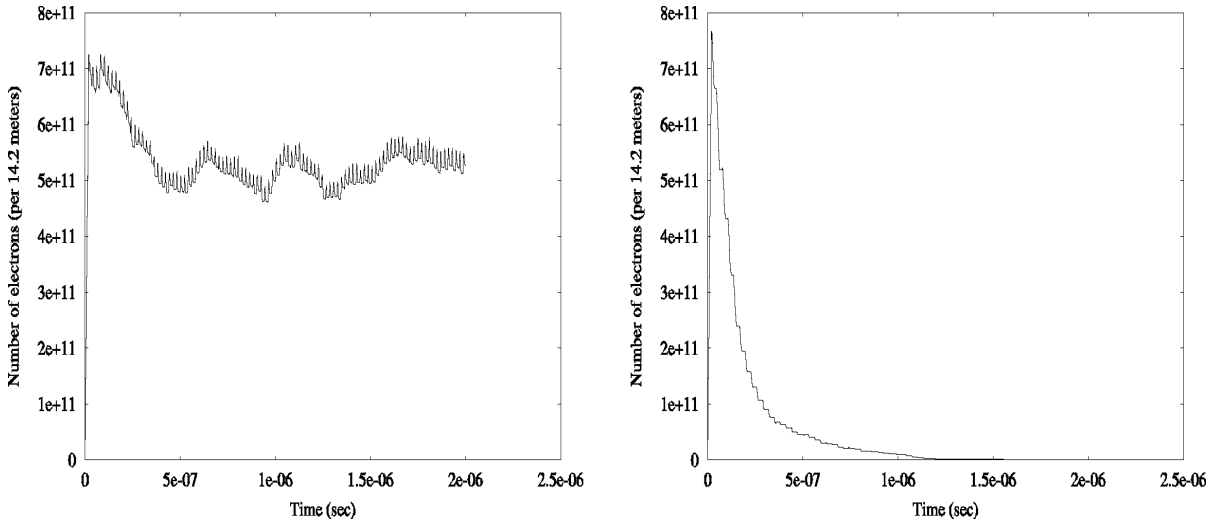

Figure 3-20: *Number of electrons in the chamber (per bending magnet) as a function of time; multipacting occurs for T=20 ns (left) but not for T=30 ns (right).*

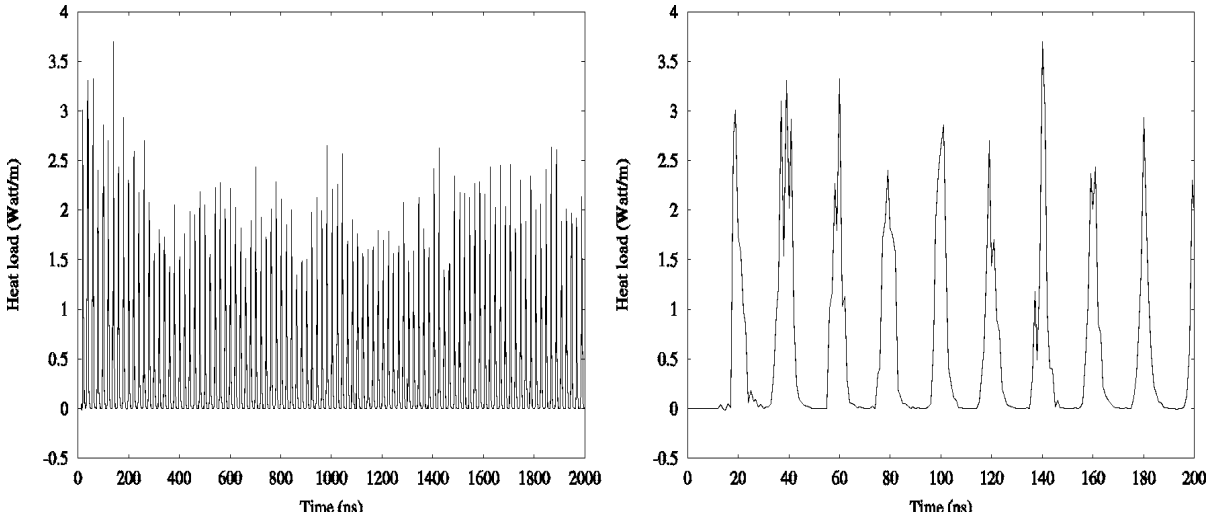

Figure 3-21: Left**:** *heat load (W/m) in the chamber, simulation of 100 rf pulse passages.* Right*: first 10 rf pulse passages, the electrons hit the surface in synchronism with the pulse*

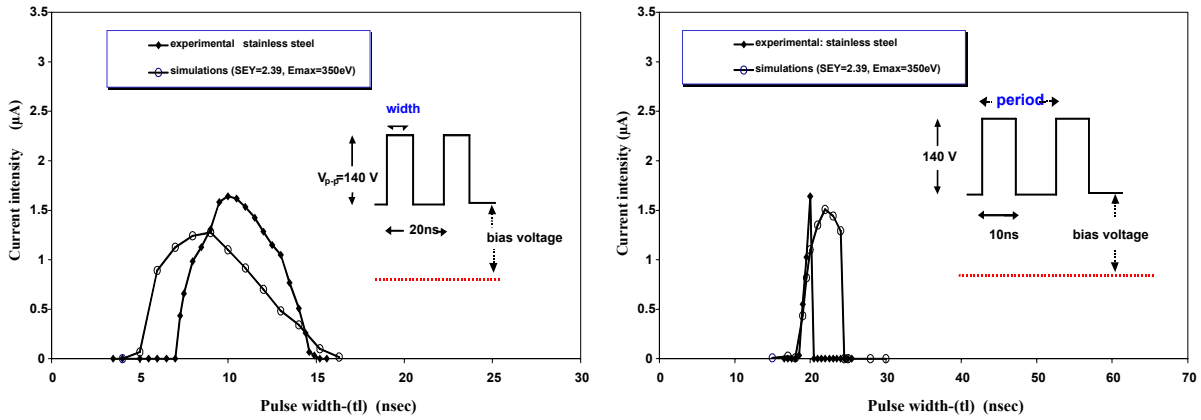

Figure 3-22: *Experimental results and simulations: multipacting current intensity as a function of the RF pulse width. For the simulations, the current intensity has been derived through the heat load (W/m)*
Left: *dependence on the pulse width* Right: *dependence on the pulse period*

Taking into account the average energy $\bar{\mathrm{E}}$ of the electron hitting the wall, the current intensity calculated for an area A is given by

$$I = \frac{1}{\bar{E}[eV]} \frac{\bar{P}[W/m]}{2\pi R_0} A \tag{3.7}$$

where A is the *effective* area of the pick-up (ca. 60 mm^2). The heat load is calculated along one meter of the structure. The average heat load $\bar{\mathrm{P}}$ in W/m is given by

$$\bar{P} = \frac{1}{nT} \int_0^{nT} P\,(t)\, dt$$

where n is the total number of pulse periods T, considered for the simulation; while the average energy is

$$\bar{E} = \frac{\int E f\,(E)\, dE}{\int f\,(E)\, dE}$$

where $f\,(E)$ is the electron energy distribution as calculated by the simulation (see Chapter 4).

The heat load $P(t)$ is shown on the *left* hand side of Fig. 3-21 as a function of time; this situation corresponds to simulation of *left*-hand side of Fig. 3-20.

It is interesting to consider the heat load during the first 10 RF pulse on the *right*-hand side of Fig. 3-21 where it can be seen that the heat load has a period of 20 ns, equal to the RF pulse period. The electrons hit the chamber surface in synchronism with the RF pulse, in a window of 3÷4 nsec (FWHM of the heat load distribution curves).

After evaluation of the number of electron hitting the area A per unit time, I have

compared the simulation and experimental results in Fig. 3-22 (see also Figs. 3-13 and 3-14). The *left*-hand side of Fig. 3-22 shows the multipacting as a function of the RF pulse width for a fixed $T = 20ns$, while the dependence with the pulse period is shown on the *right* hand side for a fixed $W = 10ns$; in both cases the pulse amplitude and bias-voltage are $V_{p-p} = 140V$ and $V_b \sim 63V$ respectively.

The simulations seem to be qualitatively in agreement with the experimental results, indicating nevertheless that the heat load could be underestimated by 10-20% with respect to the real case. The discrepancy between simulation and experimental results gives the possibility to revise the simulation code. Cross checking the simulations with the experimental results gives also the possibility to have a more precise estimate of some of the physical parameters introduced in the simulation.

Chapter 4

Electron energy spectrum

Introduction

As discussed in Chapter 1, the beam-induced electron cloud may produce a substantial heat load in the LHC beam pipe. Since the cryogenic system cannot tolerate a heat load exceeding 0.5 W/m, the current capacity based on an heat load induced by multipacting is only 0.2 W/m. The heat load is linearly dependent on the average energy of the electrons hitting the beam pipe during multipacting and the electron energy is therefore a parameter which needs to be estimated as accurately as possible.

In the travelling-wave multi-wire chamber, the impact energy distribution of the electrons accelerated by the electric field of the RF pulse towards the opposite wall is defined.

To verify the validity of the electron energy spectrum which has been estimated for LHC, the following studies have been made:

- the LHC multipacting simulation computer code has been run with the geometry adapted to the multi-wire chamber setup.
- I have studied and built an electron energy analyzer to measure the energy spectrum of the electrons hitting the surface of the multi-wire chamber during multipacting.

finally the measured electron energy spectrum has been compared with the simulation results.

The electron-cloud decreases when the secondary emission yield is below a *critical* value, while it increases exponentially if the SEY is above this value. In the multi-wire chamber the same effect occurs. The *critical* secondary emission yield has been estimated for the multi-wire chamber both by calculation and by simulations.

Section 4.1 describes the experimental setup and the energy analyzer used to measure the electron energy distribution in the multi-wire chamber. A comparison between the result of the experiment and of simulations is discussed in section 4.2. The concept of the critical secondary emission yield introduced in section 1.2, is discussed in detail in section 4.2 for the multi-wire chamber.

4.1 Electron energy spectrum in the travelling-wave chamber

4.1.1 Experimental setup and energy spectrum analyzer

In order to measure the energy distribution of the electrons hitting the surface of the multi-wire chamber during multipacting and to compare it with the energy distribution obtained by the simulations, I have built an energy spectrum analyzer, which has been mounted in a tube near the middle plane of the chamber.

During the electron multiplication process, electrons are accelerated towards the center of the chamber by the RF pulsed electric field and when they reach the opposite side may pass through the holes in a metallic grounded plate. They enter the energy spectrum analyzer situated behind; the holes must be sufficiently small (ca.1 mm diameter) to reduce the electric field penetration from the chamber, which could cause disturbance.

The energy analyzer, which has been built at CERN, is shown in Fig. 4-1 and in Fig. 4-2.

The principle of the energy analyzer is the following:

Two cylindrical plates of radii R_1 (inner) and R_2 (outer) are positioned concentrically. A positive potential U_1 is applied to the inner electrode while the outer one is grounded. The radial electric field between the two electrodes is thus generated. The entrance and the exit to the volume between the cylinder is limited by two plates, each having a $0.2mm$ slit at the median radius R_0 equidistant from both plates.

Electrons pass through a circular focusing grid before passing through the $0.2mm$ wide entrance slit.

Once inside the cylindrical section, the electrons are deflected by the radial electric field, and experience different trajectories depending on their kinetic energy. Electrons with the selected energy follow a central trajectory (at radius R_0) and pass through the second slit ($0.2mm$ wide), to be collected on a plate. The current is measured by a picoamperometer. The electron energy is selected by varying the potential of the inner electrode U_1[1].

The resolution is mainly determined by the widths of the entrance and exit slits. It can be demonstrated that directional focusing occurs in the analyzer and that a sector of 127^o gives the best focusing [2][22][23][24]. Two mu-metal $0.2mm$ foils have been used to shield the analyzer from the background magnetic field, both during the calibration test and the measurements in the chamber.

During the measurement, a negative potential (-20 V) is applied to the second slit in order to repel secondary electrons produced on the electrodes.

Solving the Laplace equation in cylindrical coordinates gives the potential, $\Phi(r)$, between two infinite cylindrical electrodes

$$\Phi(r) = C_1 \ln(r) + C_2$$

[1] with the energy analyzer described here the energy of positive ions can be measured by inverting the polarity of the applied potential.

[2] the sector in the apparatus is 90^o for construction reasons

Figure 4-1: *Section of the electron energy spectrum analyzer and plot of the field lines between the cylindrical electrodes*

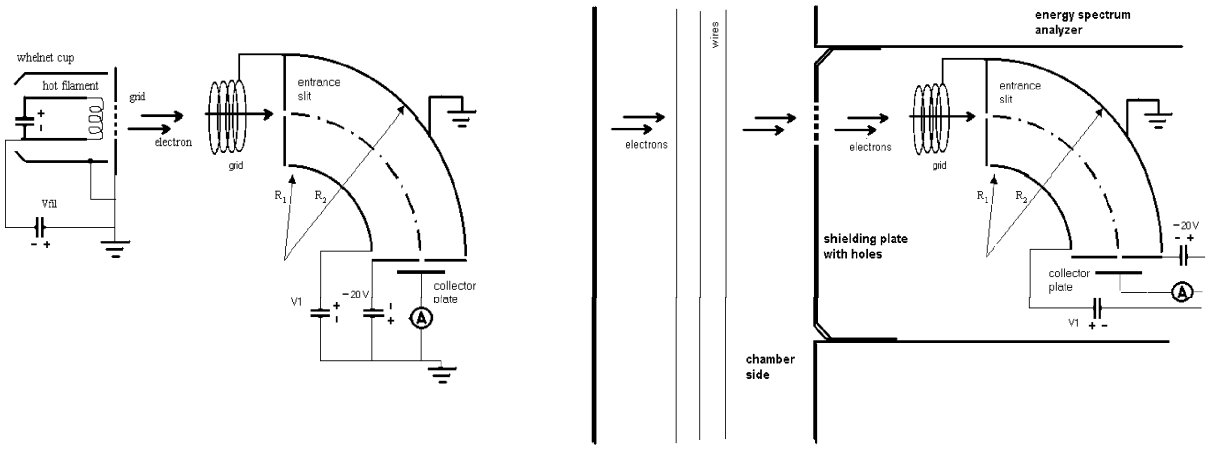

Figure 4-2: Left*: schematic cross section of the energy spectrum analyzer during the test with an electron gun (both realized at CERN). Radius R_1=11.2mm, R_2=18.7mm and the slits width=0.2mm.* Right*: installed on the multi-wire chamber*

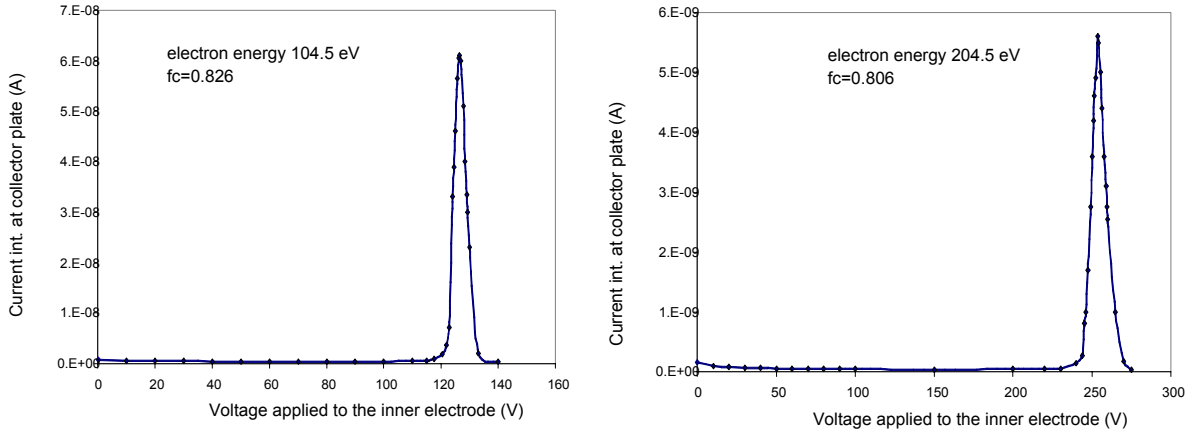

Figure 4-3: *Energy analyzer calibration with a test beam of 104.5eV* (left) *and 204.5eV electron energy* (right)

The resulting electric field is $E_r = -C_1/r$. The constants C_1 and C_2 are calculated by imposing the condition $\Phi(r_1) = U_1$ and $\Phi(r_2) = 0$ and we obtain $C_1 = -\frac{U_1}{\ln(R_2/R_1)}$, and $C_2 = \frac{U_1}{\ln(R_2/R_1)} \ln(R_2)$. The potential is therefore given by

$$\Phi(r) = -\frac{U_1}{\ln(R_2/R_1)} \ln(r) + \frac{U_1}{\ln(R_2/R_1)} \ln(R_2).$$

The electric field by

$$E_r = \frac{U_1}{\ln(R_2/R_1)} \frac{1}{r} \tag{4.1}$$

for which the vector field lines are shown in Fig. 4-1. The electrons with energy eU_e pass the exit slit if the following relation is fulfilled:

$$\frac{1}{2} U_1 = U_e \ln(R_2/R_1) \tag{4.2}$$

this relation is derived equating the centripetal force to the radial force between the two electrodes, $F_{centr} = eE_r$, and $mv^2 \frac{1}{r} = e \frac{U_1}{\ln(R_2/R_1)} \frac{1}{r}$, corresponding to a velocity $v = \sqrt{\frac{e}{m} \frac{U_1}{\ln(R_2/R_1)}}$.

The calibration test of the energy analyzer has been performed with an electron beam of variable energy, provided by a tungsten filament. The energy of the electrons leaving the hot filament (shown on the *left* hand side of Fig. 4-2) is given by:

$$E = eV_f + e\phi + kT$$

where V_f is the voltage difference between the filament and the grounded collector probe of the energy analyzer, $e\phi$ is the work function of tungsten (4.5 eV), and kT the thermal energy (0.02 eV at 293^{o}K). The resolution is defined as the ratio of ΔE (FWHM)

to the kinetic energy E_0 of the peak position, $res = \frac{\Delta E}{E_0}$, often expressed in percentage $(\Delta E/E_0) \times 100$.

Calibration of the spectrum analyzer

From Eq.(4.2), in the case of R_2=18.7mm and R_1=11.2mm, we obtain the relation $eU_1 = 1.02 \cdot E$, with U_1 being the inner electrode potential for which the electrons of energy E, are deflected along the trajectory of radius R_0 and collected on the plate.

The above Eqs. (4.1) and (4.2) have been derived for infinite cylindrical electrodes, while in the real case a correction factor must be introduced. The correction factor, defined as $f_c = \frac{E}{eU_1}$, has been estimated during the calibration test. The electron energy during the measurement will be given by $f_c eU_1$[3].

The results of the calibration test are shown in Fig. 4-3. The electron beam energy on the left-hand side is $E = 104.5eV$. The peak of the current intensity recorded at the collector plate corresponds to $U_1 = 126.4V$, which results in a correction factor $f_c = E/eU_1$ =0.826. The energy resolution is $res = \Delta E/E_0 \approx 4\%$.

4.2 Electron energy spectrum - measurements and simulations

I have measured the energy distribution in the multi-wire chamber surface during multipacting with the energy analyzer described in the previous section. Fig. 4-4 shows the current intensity recorded at the collector plate of the spectrum analyzer as a function of the electron energy, in the case of an RF pulse with the following characteristics: pulse amplitude 140V, period 20 ns, width 10 ns, and bias-voltage ca. 65V. The background noise is higher at lower energies.

The energy distribution function $f(E)$ shown in Fig. 4-4 has the dimensions of a current, and the spectrum or number of electrons per unit energy is given by

$$\frac{dN}{dE} = \frac{T}{e} f(E) \tag{4.3}$$

where T is the pulse period over which the measured current is averaged.

Fig. 4-5 shows the measured spectrum and the spectrum obtained by the simulations with the same pulse characteristics. In the simulations the pulse amplitude has been chosen as discussed in appendix B of Chapter 3. The electron energy spectrum is peaked around a single energy value. The width FWHM of the experimental peak is $15eV$, against a width of ca. $8eV$ from simulation.

Fig. 4-6 reports the peaks of the energy distribution as a function of the RF pulse amplitude V_{p-p}. Here it is shown the dependence of the energy peak, from 40 to 85 eV, on the pulse amplitude, from 80 to 210 Volt. Then, the simulations are in good agreement

[3] f_c is a function of the electron energy

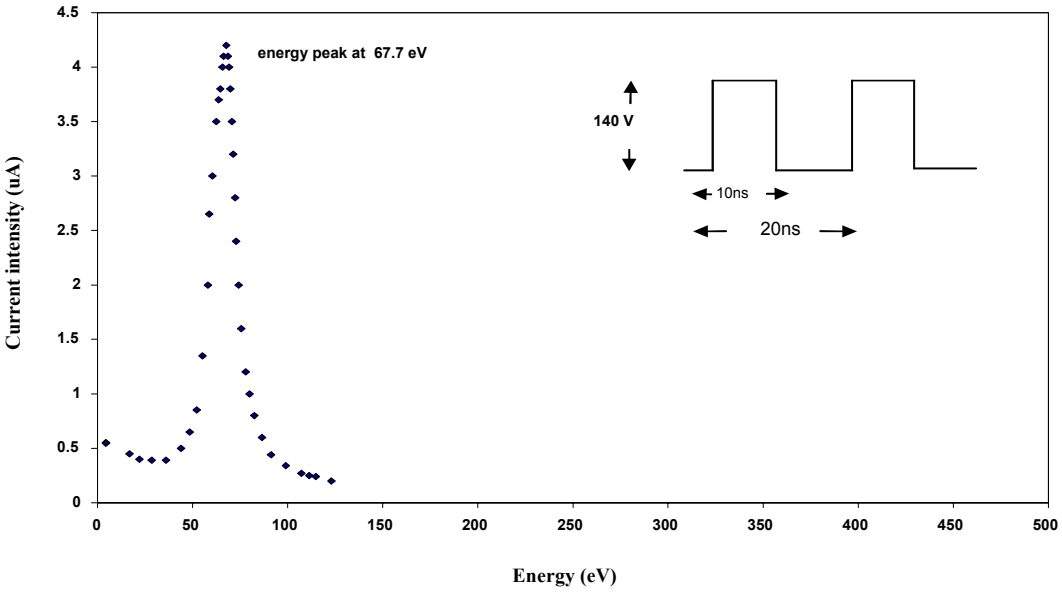

Figure 4-4: *Energy distribution of the electrons hitting the vacuum chamber*

with the experimental data.

A perfectly rectangular RF pulse shape is shown in Fig. 3-6, where the DC voltage applied to the wires is also taken into account; I refer to "bias-voltage" and to the squared potential as represented by the displacement to ground and by the upper level of the RF signal; In the subsequent section I will examine the effect of the two contributions on the electron motion.

If we apply a positive constant potential, the electrons oscillate back and forth inside the chamber without being able to strike the wall. If now the squared potential is superimposed to the constant voltage, this supplies the energy difference for the electrons to hit the wall, with an energy defined as the impact energy. Thus, the bias-voltage is important when one considers the average velocity, while the pulse potential fully determines the impact energy. Therefore I have pointed out that the electron impact energy is independent of the bias-voltage.

To validate this assumption I have measured the energy distribution of the electrons hitting the wall as a function of the bias-voltage. In Fig. 4-7 the peak of the energy distribution of the electron hitting the wall is plotted as a function of V_b. The energy peak remains constant in the bias-voltage limits for which multipacting occurs. This can be seen in Fig. 3-15 where the same pulse parameters are set. This means that shifting the whole RF pulse up with respect to the ground potential has practically no effect on the electrons impact energy.

The instant energy of the 5eV *reference* electron during its flight in the multi-wire chamber is plotted in Fig. 4-8, where the pulse parameters correspond to the parameters of Fig. 4-5. The electron is accelerated towards the central region, where the potential is

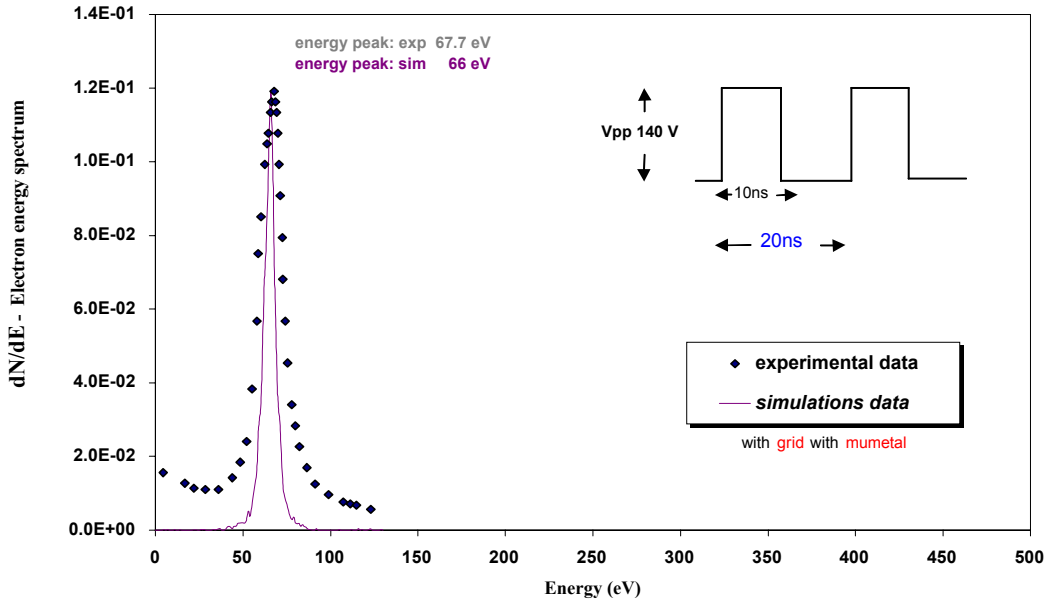

Figure 4-5: *Measured electron energy spectrum and spectrum obtained by the simulation*

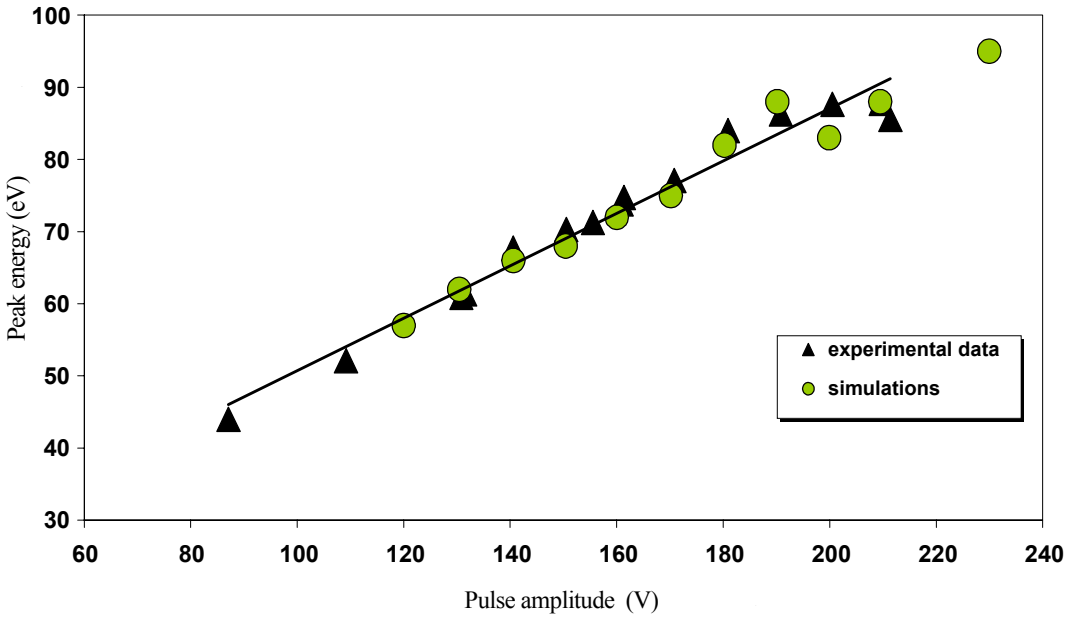

Figure 4-6: *Experimental and simulation results: Peaks of the energy distribution as a function of the RF pulse amplitude V_{p-p}, linear dependence of the energy peak from 40 to 85 eV with the pulse amplitude from 80 to 210 Volt*

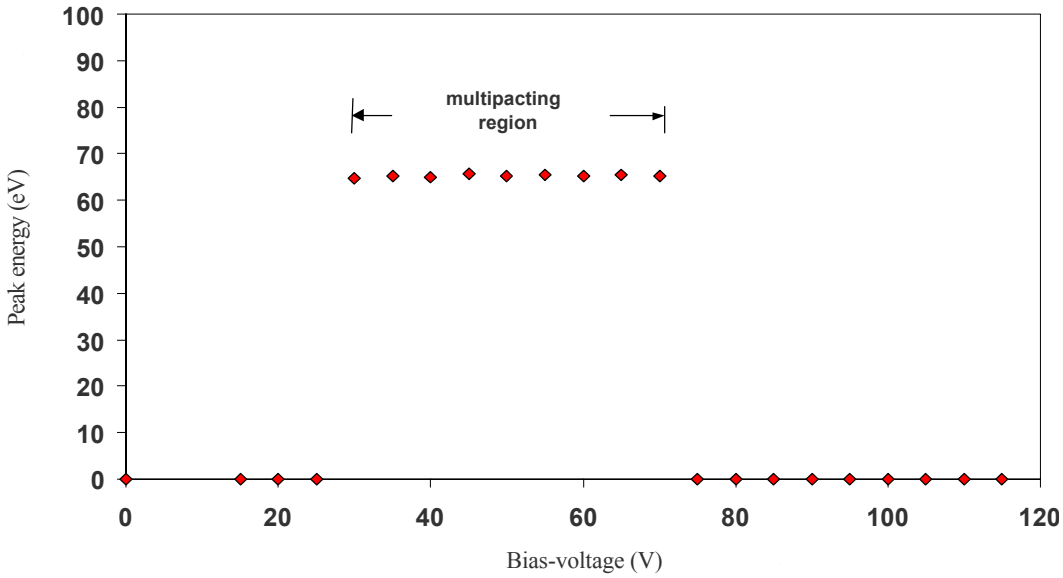

Figure 4-7: *Energy corresponding to the peak of the energy distribution, as a function of the bias-voltage of the RF pulses: experimentally the electron energy spectrum of the electrons hitting the vacuum chamber surface is not dependent on the bias-voltage* V_b

constant, and is decelerated before hitting the surface after one pulse period (T=20 ns). The final energy shown here is the impact energy at the wall as measured by the energy spectrum analyzer.

4.2.1 Critical secondary emission yield in the multi-wire chamber

As discussed in section 1.2.3, the secondary emission yield as a function of the energy E of the electrons and of the incidence angle θ, can be expressed by

$$\delta_{SEY}(E,\theta) = \frac{\delta_{\max}}{\cos\theta} h\left(\frac{E}{E_0}\right) \simeq \delta_{\max} h\left(\frac{E}{E_0}\right) \tag{4.4}$$

I introduce the following approximation $\theta \sim 0$, since the electrons experience approximately straight trajectories in the multi-wire chamber (as discussed in the previous chapter 3).

Integrating the spectrum $\frac{dN}{dE}$ over all the energies one obtains the number of electrons entering the aperture area A of the energy spectrum analyzer

$$N_0 = \frac{1}{A}\int_0^\infty \left(\frac{dN}{dE}\right) dE = \frac{1}{A}\int_0^\infty \frac{T}{e} f(E)\, dE \tag{4.5}$$

where N_0 has the dimensions of particles per unit area.

When the electrons hit the surface they may produce a new generation of secondary

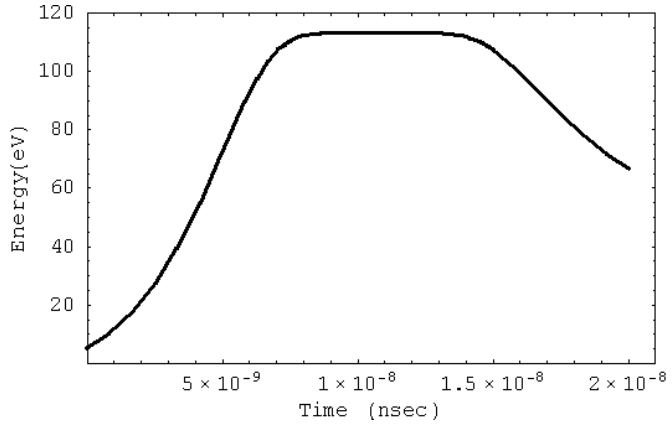

Figure 4-8: *Instantaneous energy computed for an electron with an initial energy of 5eV, during its flight in the multi-wire chamber. The impact energy is approx. 66eV at T=20ns.*

electrons. Given the secondary emission yield $\delta_{SEY}(E)$, the new generation of electrons is given by

$$N_{se} = \frac{T}{eA}\int_0^\infty \delta_{SEY}(E)\, f(E)\, dE. \tag{4.6}$$

If the ratio N_{se}/N_0 is greater than 1, the electron multiplication is possible. The condition for multipacting is therefore given by

$$\frac{N_{se}}{N_0} = \frac{\int_0^\infty \delta_{SEY}(E)\, f(E)\, dE}{\int_0^\infty f(E)\, dE} \geq 1 \tag{4.7}$$

or using Eq. (4.4)

$$\delta_{\max} \geq \delta_{crit} = \left(\frac{\int_0^\infty h\left(\frac{E}{E_0}\right) f(E)\, dE}{\int_0^\infty f(E)\, dE}\right)^{-1}. \tag{4.8}$$

The definition of the critical secondary electron yield δ_{crit}, given by the Eq. (4.8), corresponds to the minimum value $\delta_{\max}$ necessary to produce a number of new generation secondary electrons equal to the initial number of electrons. The condition, $\delta_{\max} \geq \delta_{crit}$ is therefore a necessary condition to have multipacting.

Assuming that the secondary electron yield is larger than the critical one, i.e. $\delta_{\max} \geq \delta_{crit}$, as for the LHC case, the initial number of electrons will be multiplied after each RF pulse passage by a factor $1+q$, where $q = \mid \delta_{\max}/\delta_{crit} - 1 \mid$. This gives an exponential growth

$$N_e \approx N_{se} e^{\left(\frac{qt}{T}\right)} \tag{4.9}$$

where T is the RF pulse period, and N_{se} the number of secondary electrons generated

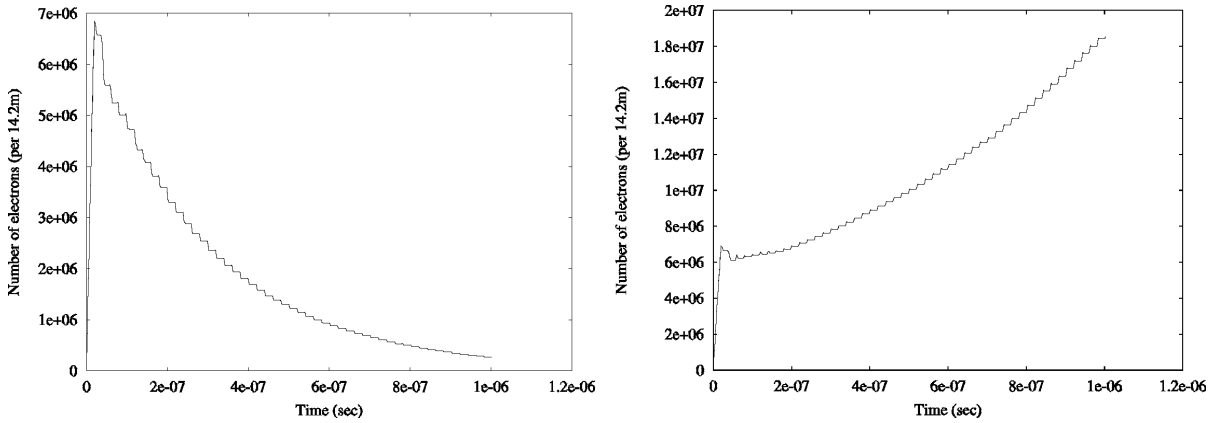

Figure 4-9: *Evolution of the number of electrons in the multiwire chamber, for the highest possible pulse amplitude and for* $\delta_{crit} = 1.7$. Left-side*:* $\delta_{\max} = 1.6 < \delta_{crit}$ Right*:* $\delta_{\max} = 1.7 \gtrsim \delta_{crit}$.

after the first pulse passage [20]. The unlimited growth predicted by Eq. (4.9) will be stopped by two effects: the electrons which are lost on the wires and by the space charge effect (see below).

If the condition for electron multiplication is not satisfied, i.e. $\delta_{\max} < \delta_{crit}$, an initial electron cloud will decay as $N_e \approx e^{\left(-\frac{qt}{T}\right)}$. The characteristic time which determines the exponential growth or decay of the electron cloud is then given by

$$\tau_{growth} = \frac{T}{q}$$

Fig. 4-9 shows the evolution of the number of electrons in the vacuum chamber as a function of time. The *left*-hand side shows the case $\delta_{\max} < \delta_{crit}$, and the *right*-hand side shows the case $\delta_{\max} \gtrsim \delta_{crit}$.

In order to find the critical secondary electron yield, I generate electrons during the first 20 pulses and look at the evolution of the number of electrons over 100 subsequent pulse passages. I have determined the minimum value $\delta_{\max}$ for which multipacting occurs, resulting in an exponential growth of electrons [4]. The critical SEY has been determined for different values of the RF pulse amplitude and is shown in Fig. 4-10.

The method of estimating δ_{crit}, by looking at the evolution of the number of the electrons, is compared with the estimate obtained by integrating Eq. (4.8). The difference between the two methods is that in the latter *analytical* method I integrate the normalized SEY $h(\xi)$, which is independent of $\delta_{\max}$, while in the *simulation* the secondary electron yield $\delta_{\max}$ is used to calculate the number of secondary electrons produced when the primary electrons reach the vacuum chamber. It can be seen that both methods are in

[4]The threshold of $5{\cdot}10^6$ electrons (per LHC magnet length) corresponds to a current of 10 pA on the pick-up. This current corresponds to the minimum multipacting current detected by the picoamperometer.

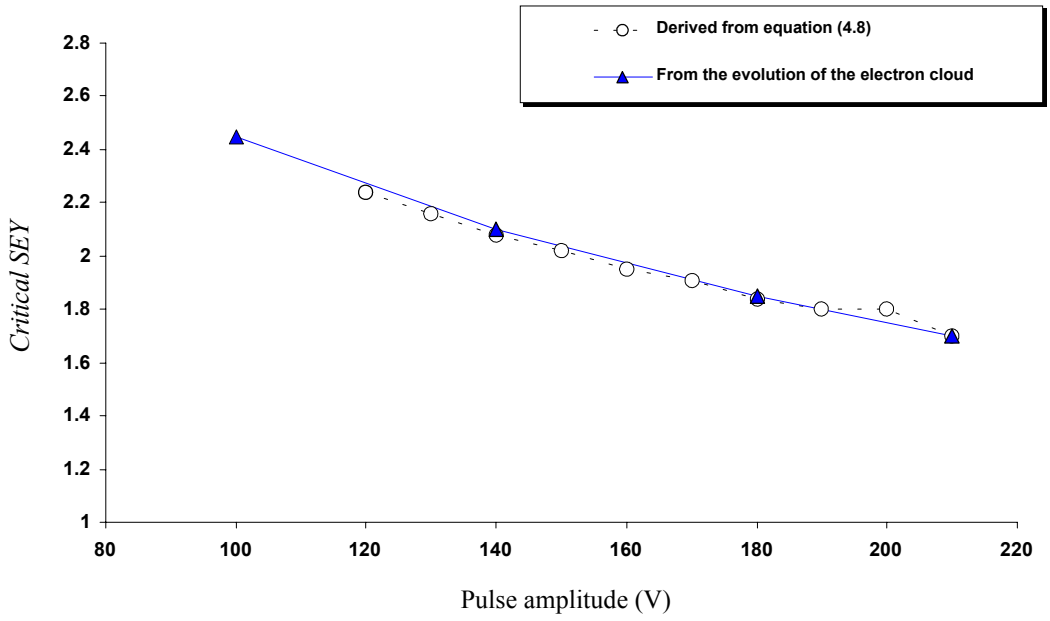

Figure 4-10: *Critical secondary electron yield δ_{crit}, obtained by integrating the energy spectrum of Eq. (4.8) and derived from the evolution of the electrons number during simulations*

good agreement.

When setting the highest available output power (pulse amplitude 210V, see Fig. 4-10) the critical secondary electron yield results to be δ_{crit}=1.7. Therefore, if the secondary electron yield of the surface is lower than 1.7 multipacting can no longer be initiated in the multi-wire chamber.

As it will be discussed in detail in the Chapter 5, an intense electron bombardment leads to a decrease of the SEY and to a shift of E_{max} towards higher values, as shown on the *left*-hand side of Fig. 4-11.

A shift of E_{max} from 300eV to 450eV, and a decrease of $\delta_{\max}$ from 2.4 to 1.3, has been considered in the simulations [19].

If I do not include the shift and keep E_{max} constant when $\delta_{\max}$ decreases, the resulting critical secondary electron yield is reduced. In particular, setting the highest pulse amplitude and considering a constant value $E_{max} = 300eV$ in the simulation, the result is

$E_{max} = 300eV$	$300eV < E_{max} < 450eV$
$\delta_{crit} = 1.4$	$\delta_{crit} = 1.7$

The critical secondary electron yield was previously estimated for LHC, by means of the simulations, keeping $E_{max} = 300eV$ constant. As discussed in Chapter 1, for the nominal LHC beam parameters, the result was $\delta_{crit} = 1.4$. The critical secondary electron yield is a crucial parameter for LHC, and a large effort is aimed at reducing the effective

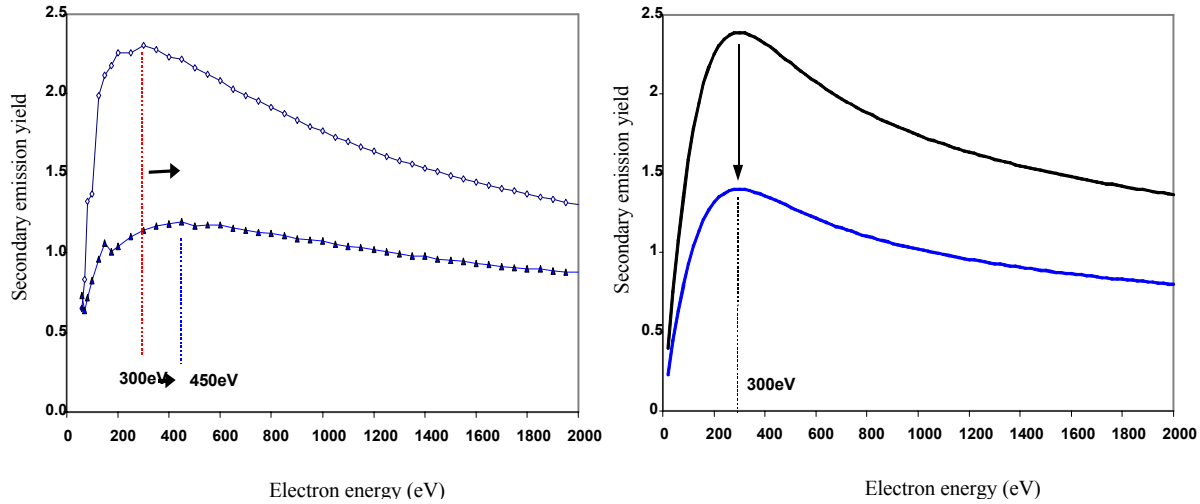

Figure 4-11: Left*: Under the effect of an intense electron bombardment the secondary electron yield decreases and a shift of* $\delta_{\max}$ *towards higher electron energies occurs.* Right*: Emax remains fixed at 300eV when* $\delta_{\max}$ *decreases [19]*

SEY below this value. Including the E_{max} shift in the simulations for LHC may result in an increase of δ_{crit}. The estimation of δ_{crit} taking into account the real behaviour of the secondary electron yield curve, is then important. One can predict for the LHC a difference smaller than 20%, when including the E_{max} shift, as it was found in the case of the multi-wire chamber[5], since for the LHC the average electron energy is higher.

Effects limiting the growth of multipacting

As mentioned before, the growth of the electron cloud, predicted to be unlimited by Eq. (4.9) results to be stopped. Once the pulse parameters are fixed, the electron cloud does not grow up indefinitely. On the contrary, since I measure an almost constant current intensity at the pick-up, I can deduce that the system is at equilibrium.

A possible effect, limiting the growth of the electron cloud, is the space charge. An estimation of the electron cloud density, n_e, at which the space charge effects becomes important is given by the Debye radius for the electron cloud

$$r_D = \sqrt{\frac{E_{se}}{4\pi n_e e^2}}$$

where E_{se} is the average energy of the secondary electrons. If the electron density is such that the Debye radius is comparable to the multi-wire chamber radius, the electric field of the space charge will push the new secondary electrons back to the surface preventing the exponential growth of the electron cloud [20].

[5] the average electron energy is higher for LHC

If this equilibrium is due to the space charge effect, then a maximum electron density would be reached. In the experiment it is found that the current intensity is a function of the pulse amplitude applied. And therefore, the electron density does not reach a saturation value. In fact, when increasing the pulse amplitude the measured electron current always increases.

Another effect, limiting the growth of the electron cloud, could be a loss mechanism of the electrons.

When the electrons hit one of the wires they may produce low energy secondary electrons. These secondary electrons may reach the chamber wall and may be lost[6]. Alternatively, they are attracted back to the wire by the subsequent pulse, and they are trapped in the wire potential and no longer participate in the multipacting process.

When the system reaches the equilibrium, the electrons lost on the wires compensate exactly the number of electrons which are created at the wall of the vacuum chamber. From equations (4.5) and (4.6) the electrons lost per unit area

$$N_{lost} = \frac{1}{A}\int_0^\infty \delta_{SEY}(E)\left(\frac{dN}{dE}\right)dE - \frac{1}{A}\int_0^\infty \left(\frac{dN}{dE}\right)dE = \frac{T}{eA}\int_0^\infty \left(\delta_{SEY}(E)-1\right)f(E)\,dE \tag{4.10}$$

where $f(E)$ is the measured energy distribution. From Eq. (4.10) it is possible to give an estimation of the secondary electron yield δ_{SEY} by measuring the electron current collected at the wires.

Another possible explanation is that when the electron cloud build-up, a partial short-circuit is produced, which decreases the impedance of the transmission line. Thus, a part of the incident RF power is reflected by the impedance change, and the available voltage is limited, as well as the electron energy and the transmitted signal.

[6] the average energy of the secondary electrons is 5eV, the seconary electron yield is $\delta(5eV) \ll 1$, see Fig 3-4.

Chapter 5

Remedies to reduce the electron-cloud build up

5.1 Introduction

Some conventional remedies to reduce the multipacting phenomenon in the RF cavities or waveguides are coating the surface with a low SEY material, baking the surface to desorb surface contaminants, conditioning the surface by means of electron bombardment and to shape the components with particular geometries.

In order to avoid the build-up of an electron cloud in the LHC, I have studied a series of remedies by means of the travelling-wave multi-wire chamber.

When the multipacting is initiated in the experimental chamber for a fixed pulse amplitude, the electron cloud produced current on the probe is observed to decrease with time until it completely disappears, after a sufficiently long processing time. This typical behaviour known as 'conditioning' or 'scrubbing' is one of the most effective ways to cure the electron multiplication in RF cavities and high power components such as couplers, windows and waveguides.

Scrubbing by means of the energetic multipacting electrons might be one of the most effective ways to clean up, *in-situ,* the beam screen surface for LHC.

We estimate the time necessary to decrease the secondary electron yield below the critical value for LHC, by means of the photo-electron dose only. If one includes with this estimate also the multipacting electrons the scrubbing time is further reduced. However, the pressure in the beam pipe can increase due to electron stimulated desorption, causing finally the loss of the proton beam, if its intensity is too high.

Surface conditioning due to an intense electron bombardment results in a decreasing of the secondary electron yield.

Even if the variation of δ_{SEY} during multipacting, or electron bombardment is known, the decreasing effect is still not fully understood. To better understand the phenomenon and to study the effect of multipacting on the surface composition, Auger electron spectroscopy analysis of samples exposed to different multipacting electron doses have been performed.

In addition to the *in-situ* beam-scrubbing method for LHC, other possible remedies

have been studied in order to suppress multipacting in the most effective way and as permanently as possible. As the first method the system has been baked-out to study the effect of thermal desorption on multipacting.

A promising way to eliminate multipacting from the system was a novel Freon11 (CCl_3F) plasma RF discharge treatment, which I have tested on a stainless steel and copper surface. In addition, I have studied the recontamination time after the freon plasma treatment and after venting the system to atmospheric pressure with air for long period of time. Auger analysis shows that in stainless steel and copper samples exposed to the freon plasma two effects occur on the different surfaces, both very effective to reduce the secondary electron yield.

In order to study multipacting with different LHC surface materials, like copper, TiZrV-coated (NEG) and aluminium made from rolled sheets ($100mm$ diam., $1.4m$ long), were introduced into the multi-wire chamber.

The multipacting conditioning time has been measured on the copper surface.

TiZrV non evaporable getter alloy once activated, by means of heating, shows a secondary electron yield lower than 1.1 [39]. After fitting the TiZrV rolled sheet in the chamber and baking the system up to $180°C$ for 12 hours, I have verified the vanishing of multipacting, following the NEG activation.

Finally we were interested to measure directly the reduction of the secondary electron yield in the multi-wire chamber during multipacting conditioning. I have built and tested a system to measure the SEY in the multi-wire chamber.

For LHC other possible remedies under investigation are: special coatings, photon scrubbing, satellite bunches situated behind the proton bunches to remove slow photoelectrons [19], axial solenoid magnetic field (discussed in Chapter 6), increasing the bunch spacing or decreasing the beam intensity, and clearing electrodes [14].

In this chapter introductions to the secondary electron emission and to the electron stimulated desorption are given in section 5.1.1 and 5.1.3 respectively. The decreasing of multipacting during conditioning and the related decrease of the SEY will be discussed in section 5.2. The promising results to suppress multipacting by means of a freon plasma treatment both on a stainless steel and on a copper surface with subsequent venting to atmospheric pressure with air, are shown in section 5.3. Results obtained with a copper surface and TiZrV non evaporable getter activation are presented in section 5.4 and 5.5 respectively. The apparatus to measure the SEY is shown in section 5.6. The Auger surface analysis of both samples exposed to different multipacting electron doses, and samples exposed to freon plasma conditioning, are reported in section 5.7.

5.1.1 Secondary electron emission

Secondary electrons (S) are emitted from a surface when a primary electron (P) impinges a solid.

Experimental information about S can be obtained by measuring of the number of S emitted per second from a unit area of the surface with energy E in the direction $\Omega(\theta, \varphi)$. This function is the current density, denoted by $J_s(\theta, \varphi)$. The current density can depend only on the state of the interacting systems, that is to say, on the properties of primary beam and on the physical and chemical properties of the emitter; such as chemical composition, crystal structure, surface conditions.

The aim of an experimental investigation is to measure the function $J_s(\theta, \varphi)$. Although, theoretical studies on the subject have contributed to clarify the problems, our experimental as well theoretical knowledge of the function J is still unsatisfactory. From the experimental side, the reason for this lies in the difficulties connected with measurement of low energy electrons (E<20eV). In addition, the agreement between theory and experiment is somewhat doubtful. The shape of the theoretical δ given by Eq. (C.1), in section C, is in reasonable agreement with experimental results. However on the other hand some experimental results are *not* in accordance with the theoretical predictions.

In order to clarify the meaning of the single processes effective in the secondary emission, we will examine how a calculation of J has to proceed in principle. The first interaction occurring is that of the P with the potential barrier on the surface. The impinging primary beam will be divided into two parts, the reflected part and the part of P penetrating in the solid. The latter part will interact with the atoms and nuclei.

The primary electrons will suffer both elastic collisions with atomic nuclei where their direction is changed and lose energy via the interaction with electrons. The former process results in splitting the primary beam and thus partly in a reversed motion toward the surface. The Coulomb interaction between P and the electrons causes the excitation of the latter. The inner S generated will interact with the different components of the solid, electrons and phonons. During their motion they will spread over the solid in a similar way as the P, and will partly reach the surface where they will be reflected or emitted according to their energy and direction of incidence.

Energy distribution of the secondary electrons

The energy of the emitted secondary electrons varies from *zero* up to the primary electron energy. One may distinguishes mainly between three groups of secondary electrons: true secondary electrons, inelastically backscattered primary electrons and elastically reflected primary electrons.

Most emitted electrons have low energies (<20eV), with a spectral energy distribution peaked around 2eV, the average energy is $4 \div 5$eV and the distribution width is typically $\sigma \approx 5$eV. These are referred to as true secondary electrons, indicating that they are electrons which originally occupied bound states in the crystal, they result from inelastic collision of the P. In each collision process only a relatively small amount of energy is transferred, so that a single primary electron can create several secondary electrons. As it

is impossible to determine the origin of individual electrons one usually regards all emitted electrons with an energy below $50eV$ as true secondary electrons.

The medium energy range is characterized by a relatively smooth background on which small peaks are superimposed. These are either caused by the emission of Auger electrons or by energy losses of the primary electrons due to electronic excitations in the solid.

The P may also suffer loss of energy by excitation of surface vibrations. These energy losses are considerably smaller than 1 eV.

Finally some small fraction of P is back scattered elastically.

The yield and energy distribution of the secondary electrons may be strongly affected by the state of the surface. The mean free path of incident electrons in solids is of the order of a few atomic layers, for energies about 10 and 1000eV being less than 10 atomic layers [22]. The maximum escape depth of secondary electrons from metals is estimated as 10 atomic layers. Assuming a thickness of 3Å for one atomic layer, the emitted electron origins from the upper 3nm of the solid. Differently the escape depth of secondary electrons passing through a layer of condensed gas could be one order of magnitude higher.

The secondary emission yield will be averaged between that of the base material and that of the pure condensate layer.

5.1.2 Ultra-high vacuum physics: gas desorption in dynamical vacuum

In an experimental system, the equilibrium pressure P (Torr) is obtained from the pumping speed S (l $\sec^{-1}$) and the molecular flux Q, by $P = Q/S$.

The surface of the vacuum chamber is generally covered by one or several monolayers of adsorbed molecules. The concentration N of a species on the surface is determined by the variation of the density of adsorbed particles

$$\frac{dN}{dt} = -Q_i - Q_{h\nu} - Q_e - Q_T + Q_a + Q_D \tag{5.1}$$

where the first three terms on the right side, represent respectively the gas desorption due to ions, photon stimulated desorption and electron stimulated desorption. The fourth term Q_T is the thermal desorbed gas flow, Q_a is the adsorbed gas flow. In the multi-wire chamber case, I neglect the terms $Q_i, Q_{h\nu}$, then the surface concentration is given by

$$\frac{dN}{dt} = -\sigma_D(E^{'}, M)\frac{iN}{Ae} - \zeta N e^{-\frac{E}{kT}} + 10^3\frac{\alpha}{\sqrt{MT}}p - D \cdot gradC \tag{5.2}$$

with i the primary electron current striking the surface, $\sigma_D(E^{'}, M)$ the electron stimulated cross section for desorption depending on the energy $E^{'}$ of the primary electron and the molecular weight M, k the Boltzmann constant, ζ the thermal desorption rate, E the binding energy of the molecules, T and p the temperature and pressure, D and C respectively the diffusion coefficient and the gas concentration in the metal.

5.1.3 Electron stimulated desorption (ESD)

Electron stimulated desorption can be considered as bimolecular reactions between the impinging electrons and the adsorbed particles. The variation of the density of adsorbed particles N with time is given by the first term on the right side of Eq. (5.2), which can lead to a decrease of the population of N. In a very first approximation, the integration of the desorption term equation

$$\frac{dN}{dt} = -\sigma_D \frac{iN}{Ae} \tag{5.3}$$

yields $N(t) = N_0 e^{(-\frac{i}{Ae}\sigma_D t)}$. In order to get an estimate of the effect of an electron beam on an adsorbed layer, one may consider the time

$$\tau_D = \frac{Ae}{i\sigma_D} \tag{5.4}$$

in which N drops to 1/e of its initial value. The estimation of the cross section σ_D is given by measuring the desorption time τ_D[1].

Desorption induced by electron impact can be seen in terms of the following consecutive steps:

- initial electronic excitation ($10^{-6}s$)
- redistribution of electron energy ($10^{-15}s$)
- displacement of nuclear positions, eventually leading to desorption ($10^{-13}s$)
- modification of the desorbing species as it recedes from the surface ($10^{-13}s$)

After electron excitation, the energy distribution among the various vibrational degrees of freedom until a particular bond is sufficiently energized to cause its rupture. The mechanism for desorption of neutrals according to the Menzel, Gomer, Redhead (MGR) model [22] is due to the excitation from the ground state into a repulsive state (M+A)*. During the separation of the adsorbed particle from the surface, transition to the ground state (M+A) is an effective competing channel, since the excitation energy can be readily transferred to the metal.

A recapture process may occur and the ESD cross section will in general be lower than that for dissociation in gas phase. If, however the transition occurs beyond a critical distance from the surface, the particle has already achieved sufficient kinetic energy to escape.

5.2 Decreasing of multipacting during conditioning

Once multipacting is triggered in the multi-wire chamber, the multipacting electron current at the pick-up electron probe, is observed to decrease with time. This typical behaviour is explained if conditioning due to an intense electron bombardment results in a decrease of the secondary electron yield of the surface.

[1] Assuming a constant current. In case of multipacting the current decreases and τ_D will be larger.

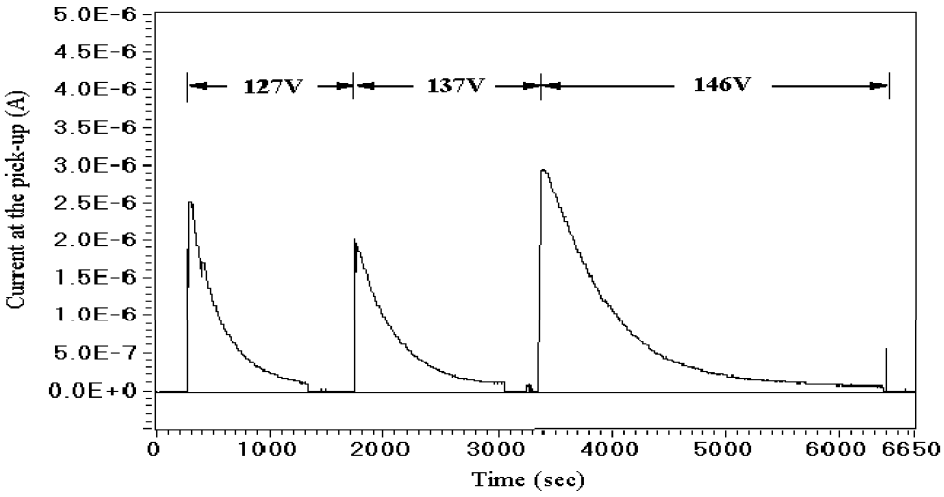

Figure 5-1: *Multipacting current at the pick-up probe as a function of time. Setting a pulse amplitude of V_{p-p}=127V, multipacting starts and decreases exponentially with time. A pulse amplitude of V_{p-p}=137V is necessary to trigger again multipacting in the chamber. A further increase of V_{p-p}=146V is necessary to start again the electron multiplication.*

As discussed in previous chapters, the condition to satisfy so that electron multiplication occurs is that the energy transfer to the electrons must be sufficient that when the electrons hit the chamber surface the average secondary emission yield is larger than unity.

When the secondary electron yield decreases, the energy E_1 corresponding to $\delta(E_1) = 1$, may shift slightly towards higher values, in the case of stainless steel or copper. In addition, if one considers also the shift of E_{max}, as shown in Fig. 4-11, the effective shift of E_1 is even more pronounced. As the secondary electron yield decreases the pulse amplitude has to be increased so that the energy gained by the electrons also increases thus restoring an average secondary electron yield sufficient to cause multipacting, see Fig.5-1.

5.2.1 Minimum pulse amplitude as a function of the electron dose and of the bake-out of the system

The minimum pulse amplitude V_{p-p}, necessary to trigger multipacting in the stainless steel multi-wire chamber ranges initially, between 75V÷100V, depending on the surface composition and on the time the system has been exposed to air.

I initiated the multipacting in the multi-wire chamber, and from time to time I stopped the conditioning to check the value of the minimum V_{p-p} required to trigger the electron multiplication. This minimum pulse amplitude is shown as a function of the integrated electron dose in Fig. 5-2. Different experiments show that the conditioning is achieved with the same electron dose, in spite of the initial value V_{p-p}, which may depend on the

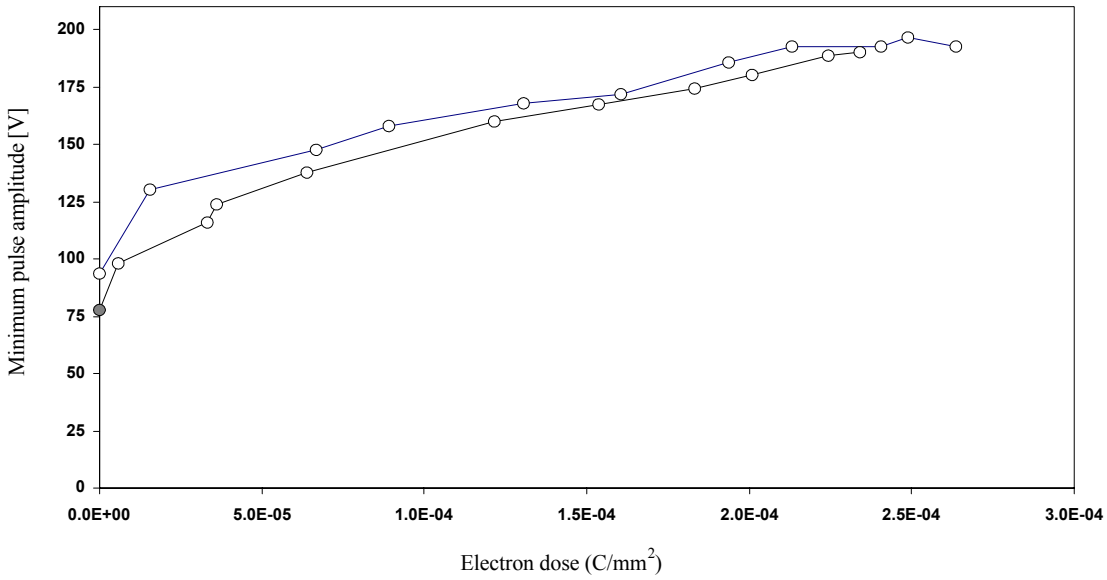

Figure 5-2: *Minimum pulse amplitude required for multipacting as a function of the integrated electron dose. Different experiments show that the conditioning is achieved with the same electron dose, in spite of the initial value* V_{p-p}.

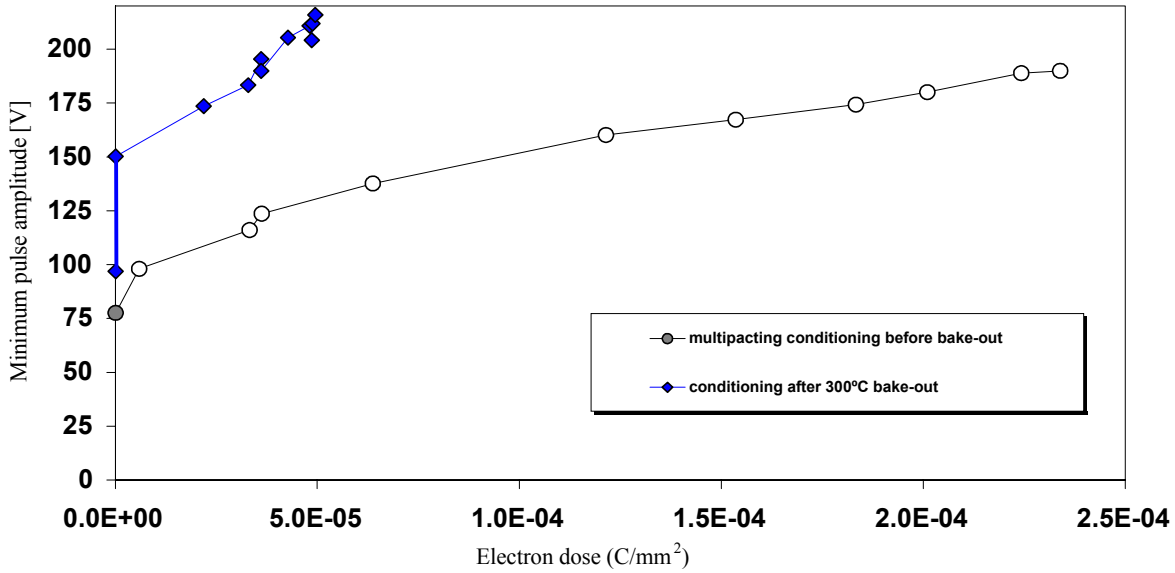

Figure 5-3: *Minimum pulse amplitude as a function of the electron dose after bake-out (upper curve) and before bake-out (lower curve).*

composition of the first few monolayers.

Once the multi-wire chamber has been conditioned, venting the chamber to pure O_2 for 24 hours, did not increase the multipacting level. However, when venting the system to air for a few days, the multipacting current on the probe returns to its original value. This method of venting has been used to re-establish the same initial conditions, in the multi-wire chamber, before each measurement.

Bake-out of the system

If the contaminating molecules on the vacuum chamber surface have a higher vapor pressure than the base material, they can be removed by heating the system. The molecules gain energy by thermal agitation and are more likely to escape from the surface so that they can be evacuated by the pumping system.

Molecules with a binding energy E[2], decrease in number according to the thermal desorbed gas flow term in Eq. 5.2 which shows that the degassing rate increases with temperature

$$\frac{dN}{dt} = -\zeta N e^{-\frac{E}{kT}}. \tag{5.5}$$

From Eq. (5.5) the time required to reduce the initial surface concentration to 1/e by heating at a temperature T is given by

$$\tau = \zeta^{-1} e^{\frac{E}{kT}}. \tag{5.6}$$

In a more complete model of bake-out, the diffusion of the molecules through the bulk of the material should also be taken in consideration, e.g. the Q_D term in 5.1.

After bake-out the degassing rate of the surfaces at room temperature is small enough that with a suitable pumping system, low pressure can be reached.

After $300°C$ bake-out of the multi-wire chamber the system has been cooled down to a room temperature. The minimum pulse amplitude required to trigger multipacting is then increased by a factor 1.5, as shown on Fig. 5-3. In addition, after the bake-out, I have triggered multipacting in the chamber and the same conditioning efficiency is achieved with one order of magnitude less dose, eliminating multipacting with an electron dose of ca. 5 10^{-5} C/mm^2.

5.2.2 Electron stimulated desorption during multipacting

Electron stimulated desorption due to multipacting, measured by means of a residual gas analyzer, is shown in Fig. 5-4, before, at beginning, during and after multipacting.

Electron stimulated desorption during multipacting[3], is also shown in Fig. 5-5. This figure is related to multipacting as a function of time shown in Fig. 5-7. The residual gas

[2] typical binding energy of gases are in the order of $1 \div 3eV$ [22]

[3] this measurement relates to a copper surface. An OFHC copper rolled sheet has been introduced in the multi-wire chamber, see section 5.4.

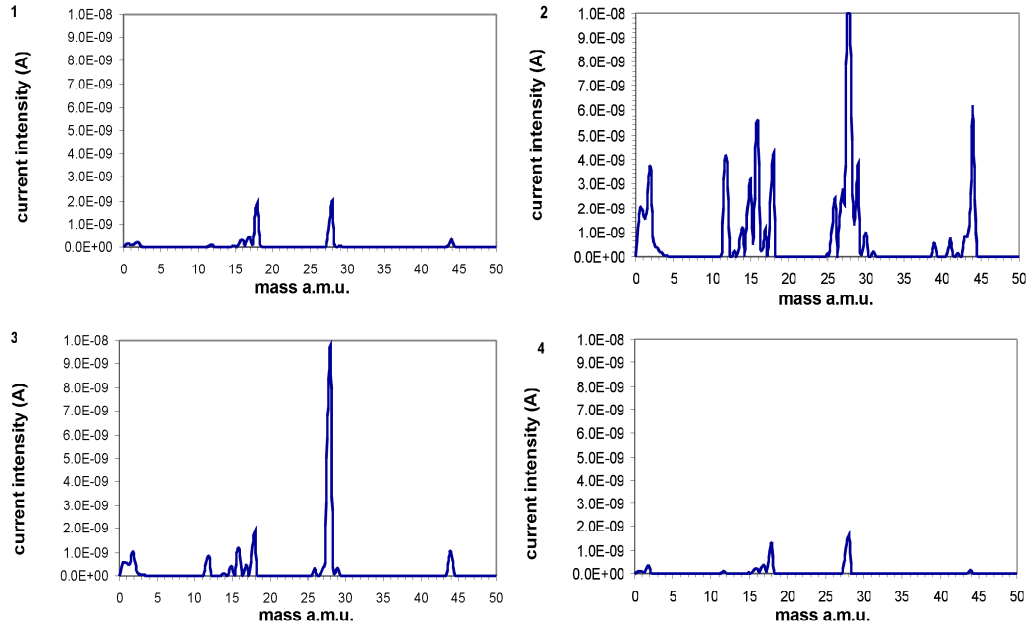

Figure 5-4: *Residual gas spectrum:* Top left*: before multipacting.* Top right*: beginning of multipacting.* Below left*: during multipacting, after 20 min of conditioning.* Below right*: multipacting stopped since 3 min.*

spectrum shows the desorption of H_2, CH_4, CO, H_2O and CO_2 when electrons strike the vacuum chamber surface. Fig. 5-6 shows the spectrum in a different scale with respect to Fig. 5-5, where peaks 2 (H_2) and 28 have been omitted to better show the behaviour of peak 18 (H_2O). The residual gas analyzer used during the measurements is described in appendix D. Extensive studies at CERN have shown that water vapour plays an important role in the contribution of the SEY, although water vapour can only increase $\delta_{\max}$ of only $0.2 \div 0.3$ in a clean copper sample [32]; according to the author, a co-adsorption of two or more gases present in air could be responsible for the strong increase of SEY. It is possible that the presence of water molecules increases the sticking probability for other gases.

5.2.3 Secondary electron yield as a function of the electron dose

The secondary electron emission yield, SEY or δ, of metals depends drastically on the composition and the roughness of the surface[4]. It is important to measure the real SEY of materials used in accelerators such as copper colaminated on stainless steel, the proposed material for the LHC beam screen. The SEY can be modified by surface treatments [29] and by *in-situ* electron bombardment, as firstly reported by Septier et al. [30][31].

As previously shown in Fig. 4-11, the variation of secondary electron yield for a sample of copper colaminated on a stainless steel substrate, shows a decrease of the secondary

[4]from a rough surface secondary electrons are less likely to escape than from a smooth surface

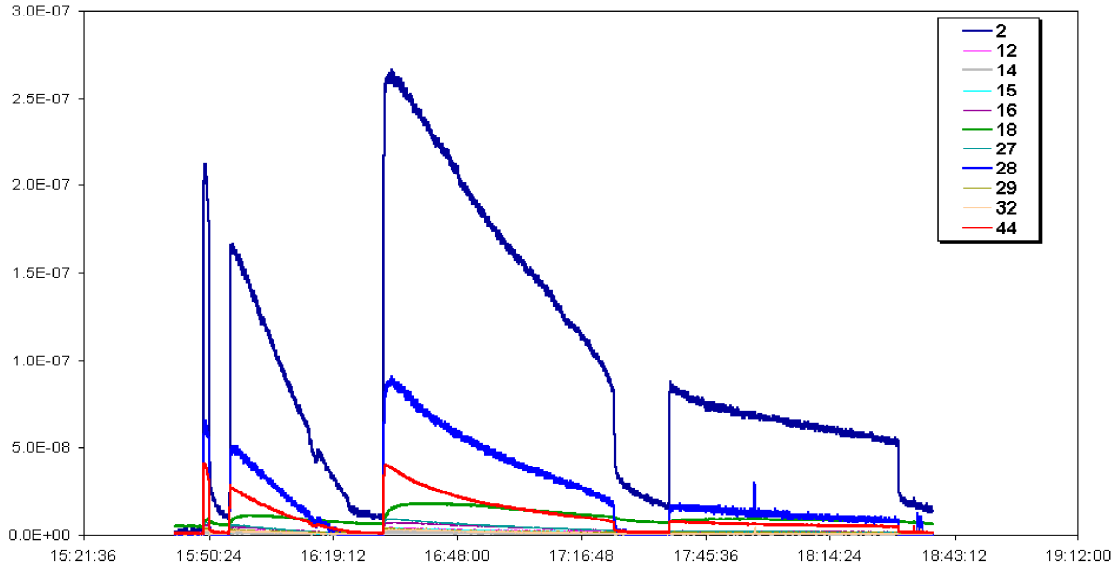

Figure 5-5: *Residual gas spectrum, during multipacting. Current $I^+_{G_i}$, measured on the RGA gauge collector (see appendix E).*

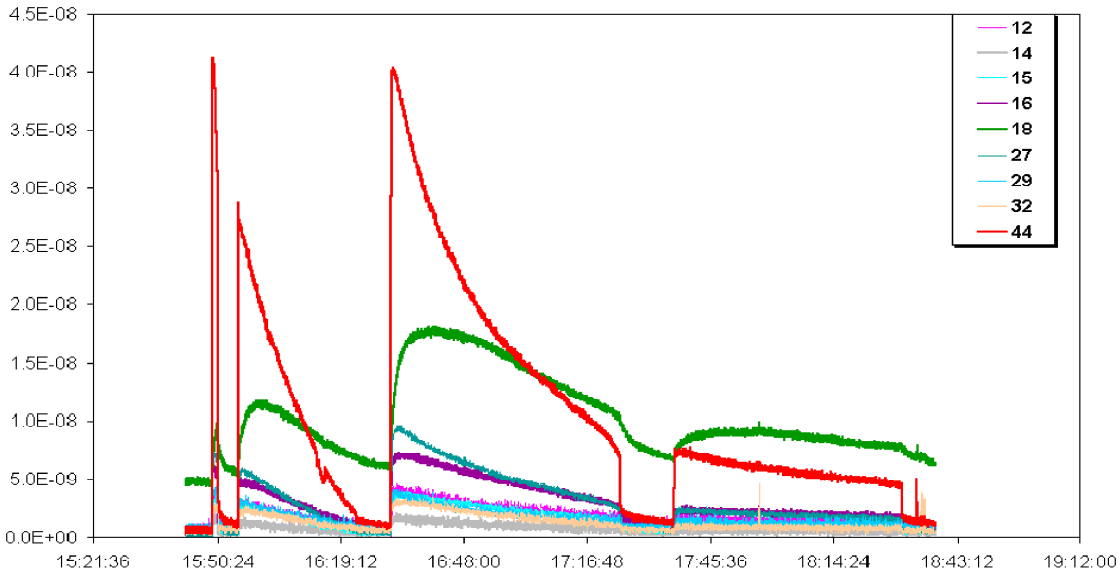

Figure 5-6: *Residual gas spectrum, during multipacting. Different scale respect to the preceding figure, where peaks 2 (H_2) and 28 have been omitted, to show the behaviour of the peak 18 (H_2O).*

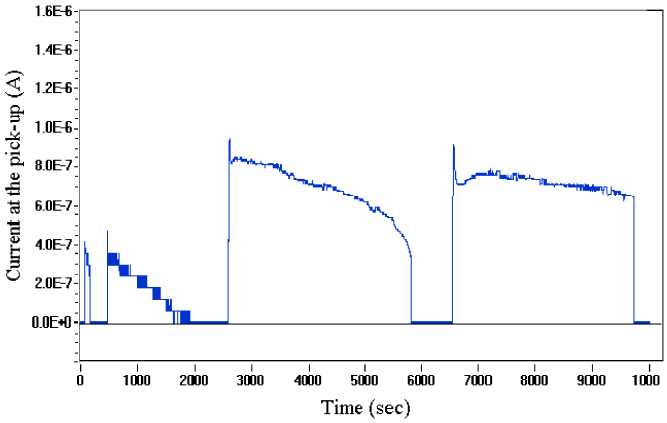

Figure 5-7: *Multipacting current at the pick-up probe as a function of time; multipacting has been intentionally stopped from time to time.*

electron yield δ_{max} from 2.3 to 1.1 after electron bombardment, with a dose $>10^{-3}$ C/mm^2. The sample was inserted in an unbaked system and the base pressure was ca. 10^{-7} Torr [19].

The variation of SEY during electron bombardment under similar experimental conditions is shown in Fig. 5-8, where the yield measured at the bombardment energy of 500 eV and 100 eV is plotted as a function of the dose on the sample. Below a dose of 10^{-6} C/mm^2, SEY does not change significantly and corresponds to the yield of the as received surface (after exposition to air). For higher doses the yield decreases towards a stable value reached for a dose larger than $5{\cdot}10^{-3}$ C/mm^2. Experiments on samples have shown that the alteration of the yield is localised to the electron impact region and is quite permanent under vacuum. Part of the SEY reduction remains after an air exposure.

In order to study the effect of the electron bombardment on the secondary electron yield, copper and stainless steel samples, exposed to different electron doses during multipacting, have been analysed by means of Auger. The results will be discussed in section 5.7.

5.2.4 Reduction of the secondary electron electron yield by multipacting in the multi-wire chamber

In the preceding section the measurement of the secondary electron yield as a function of the electron dose for copper has been reported. This measurement was obtained by monitoring the SEY when bombarding a small area of the sample, by means of an electron beam from an electron gun.

In the following section I will give an estimation of the decrease of the secondary electron yield as a function of the multipacting electron dose in the multi-wire chamber taking in consideration a larger area exposed to the electron bombardment, and therefore, reproducing more closely the situation of the LHC accelerator.

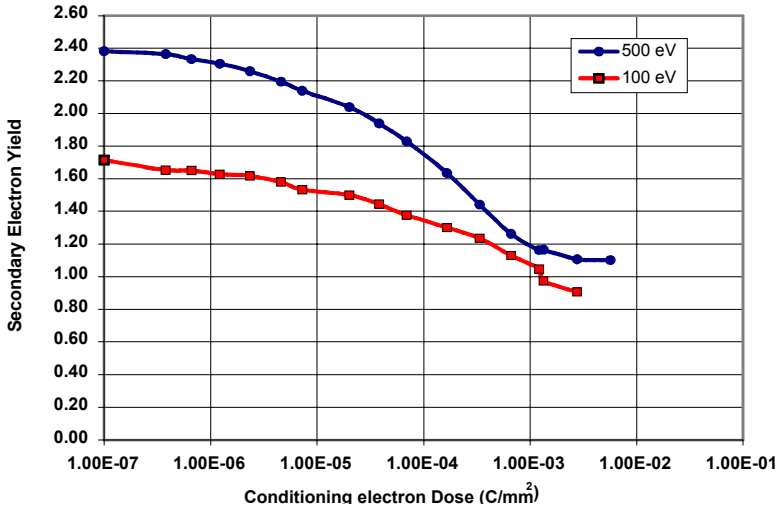

Figure 5-8: *Secondary electron yield measured at the bombardment energy of 500eV (upper curve) and 100eV (lower curve) as a function of the electron dose* [19]

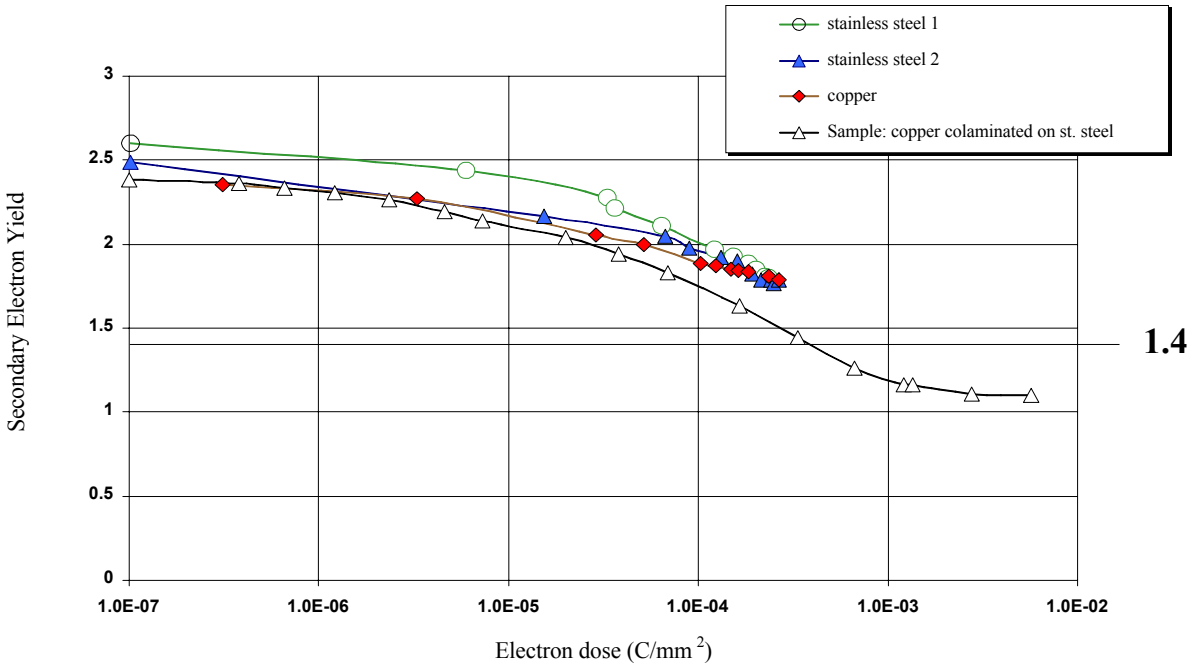

Figure 5-9: *Secondary electron yield as a function of the electron dose for the multi-wire chamber with different materials and a copper sample (primary electron energy 500eV).*

Cross checking the experimental measurements shown in Fig. 5-2, and estimations given in Fig. 4-10, related to the critical SEY as a function of the pulse amplitude given by simulations, one can correlate the decreasing of the $\delta_{\max}$ as a function of the electron dose in the multi-wire chamber.

A comparison of the reduction of the SEY with the electron dose, as measured for the copper sample and as estimated for the multi-wire chamber is shown in Fig. 5-9.

The difference can be attributed to re-adsorption of desorbed molecules inside the multi-wire chamber. Multipacting electrons stimulate molecular gas desorption from the bombarded surface, Q_e term in Eq. (5.1). The molecules are not immediately evacuated from the system but remain in the chamber with a probability of being re-adsorbed, Q_a term in Eq. (5.1), resulting in a recontamination of the surface. See in particular the behaviour of 18 peak in Fig. 5-6.

Even under high vacuum conditions ($\sim 10^{-7}$ $mbar$) a clean surface would become rapidly covered with contaminants from the residual gas atmosphere. The number of particles striking a surface of unit area per second is given by

$$\dot{n}_s = \frac{1}{4} N_g \bar{v} = N_g \left(\frac{RT}{2\pi M} \right)^{\frac{1}{2}} = 2.7 \cdot 10^{22} \frac{p}{\sqrt{MT}} (cm^{-2} s^{-1}) \tag{5.7}$$

where N_g is the number density of gas molecules, and $\bar{v}$ their average velocity, p the pressure, R the gas constant. Assuming a monolayer capacity of $3{\cdot}10^{14}$ $molecules/cm^2$, M=28 and T=300°K, Eq. (5.7) yields $\dot{n}_s \approx 10^6 p$ (monolayer/s), which means that at a pressure of $10^{-6} mbar$ the number of molecules necessary for the build up of a monolayer strikes the surface in 1 s.

In the case of the copper sample, where the electron beam coming from an electron gun hits an area of a few mm^2, the desorbed gases have a low probability to recontaminate the area from where they have been desorbed. The recontamination effect can be assumed to be negligible, resulting in an ideal decreasing of the secondary electron yield.

Differently in the case of an enlarged area, as for the multi-wire chamber, the gases desorbed by multipacting partially re-deposit on the surface where multipacting is still acting. The secondary electron yield decreases with a lower rate than during a localized electron beam bombardment of a sample. This effect must be considered when estimating the required scrubbing dose for LHC. The situation could even be worse at cryogenic temperatures, as for LHC, where cryosorbtion on the cold surface of the beam screen can not be neglected.

Furthermore, if the system is left under vacuum for a few hours, following a conditioning with an high electron dose, the multipacting threshold decreases and a partial re-conditioning is necessary, even if the re-conditioning requires a lower electron dose[5]. After conditioning a copper surface, (as discussed below in section 5.4), I have measured the minimum $V_{p-p} = 193V$. I have left the system in stand-by for 10 hours under vacuum, the final base pressure of the system was $3.8{\cdot}10^{-8}$Torr. I have verified afterwards that the multipacting threshold decreased to the minimum $V_{p-p} \approx 177V$. This recontamination

[5]This effect is typical in RF cavities.

effect, during stand-by, has been found to be pressure dependent. This effect is less pronounced in the case of a sample, where the SEY was weakly affected by a long period under vacuum [38].

5.2.5 Reduction of the secondary electron yield by beam scrubbing in the arcs of LHC

The objective is to estimate the scrubbing time necessary to decrease the secondary electron yield in the LHC below the critical value $\delta_{crit} = 1.4$.

The proton bunches in LHC produce photons which may create photoelectrons or be reflected from on the beam screen. In the dipole magnet, the photoelectrons produced in the horizontal plane experience a low energy gain from the beam, since they are constrained to move vertically by the magnetic field. The possibility has been studied to use a ribbed wall, with low forward scattered reflectivity R=0.02, which causes most of the photoelectrons to be produced in the horizontal region.

We are interested in the conditioning effect which takes place in the vertical plane in a dipole magnet section. The number of photoelectrons produced in the vertical plane is proportional to the photon reflectivity R of the beam screen material. When estimating the scrubbing time for LHC we consider, in a first approximation, only the contribution of the photoelectrons (secondary electron yield $\delta \rightarrow 0$). In the dipole magnet sections the required scrubbing time per unit length is given by

$$\tau = \frac{2\pi R_p D}{eR\gamma\Gamma} \tag{5.8}$$

where D is the required photo-electrons dose for the conditioning of the surface, γ the photoelectric yield, Γ the linear photon flux. Considering the conditioning dose for a copper sample of $5{\cdot}10^{-4} C/mm^2$ which is necessary to reduce the secondary electron yield from 2.4 to 1.4, R=0.02 (ribbed wall), $\gamma = 0.1$ and $\Gamma \approx 10^{17}$ photons s^{-1} m, the scrubbing time would be $\tau \approx 550h$.

For the multi-wire chamber I have estimated a conditioning electron dose of $1 \div 1.5{\cdot}10^{-3}$ $\mathrm{C/mm^2}$ to reduce the secondary electron yield from 2.4 to 1.4. This conditioning dose is obtained by extrapolating the curve of Fig. 5-9 for higher electron doses, where the SEY has a logarithmic dependence on the pulse amplitude. Hence, in this case, the scrubbing time for LHC increases by a factor of $2 \div 3$, to $\tau \approx 1100h$.

In the LHC straight sections the scrubbing time is reduced by a factor R. Thus, in the latter case $\tau \simeq 50h$ for the straight sections.

The previous estimate takes into account only the conditioning due to the photoelectrons, but not the contribution arising from the multipacting electrons.

Alternatively, considering multipacting electrons, and a maximum heat load $W_{max} \cong$ 200 mW/m, compatible with the cryogenic system, with an average electron energy of 200eV, the corresponding linear flux of electrons bombarding the vacuum chamber surface is $6{\cdot}10^{15}$ s^{-1} m^{-1}. The electron dose is then given by

$$D = \frac{W_{\max}}{2\pi R_p E} \approx 8 \cdot 10^{-9} \frac{C}{mm^2 s}. \tag{5.9}$$

The beam scrubbing time required to accumulate an electron dose of $1.5{\cdot}10^{-3}C/mm^2$ is reduced to about 52 hours in the dipole sections.

This estimate is obtained considering a beam intensity below the critical threshold given by Eq. (3.5). It should be mentioned, that large pressure rise induced by electron desorption, together with photo-desorption, may not permit to reach the desired stable beam intensity for scrubbing.

LHC will operate in the first commissioning period, with beams of much lower intensities. During the first year of commissioning LHC will operate with one tenth to one fifth of the nominal beam current. During this period the beam intensity will be below the multipacting threshold intensity given by Eq. (3.5).

Since mainly photoelectrons will be involved in the reduction of the SEY, to calculate the scrubbing time I will consider Eq. (5.8). If one assumes a linear increase of the beam intensity from one tenth to one fifth of the nominal intensity in a period τ_c, the photon flux will increase proportionally according to

$$\Gamma(t) = \frac{\partial\Gamma}{\tau_c}t + \Gamma_0 \tag{5.10}$$

with Γ_0 the initial photon flux and $\partial\Gamma$ the increment of the photon flux during τ_c. The photoelectron dose per unit length is given by

$$D^{'} = \int_0^{t'} \frac{eR\gamma\Gamma(t)}{2\pi R_p}dt \tag{5.11}$$

I assume a period of τ_c =3000h during the commissioning of the first year. A comparison between the accumulated *photoelectron* dose as a function of time obtained at nominal beam parameters during the commissioning period, is given on the left-hand side of Fig. 5-10. Furthermore, taking into account the reduction of the secondary electron yield as a function of the electron dose as in Fig. 5-9, one obtains the reduction of the SEY during the commissioning period, shown on the right-hand side of Fig. 5-10. The reduction of the SEY for LHC is plotted considering the typical SEY reduction rates both for the copper sample and for the multi-wire chamber.

A scrubbing time lower than the commissioning period is estimated when taking into account the reduction rate of the SEY typical of the copper sample.

In contrast to this, a scrubbing time larger than the commissioning period would be required when considering the reduction rate of the SEY for the multi-wire chamber.

One can remark that the energy gain of the photoelectrons, at one tenth of the nominal intensity, is lower than the energy gain at nominal beam intensity. From Eq. 1.7, the energy gain for a photoelectron near the wall is E_{max}=2eV, when N_b is one tenth of the nominal value. The photoelectrons may not gain sufficient energy under these conditions to be effective for scrubbing; thus, low energy photoelectrons could be lost, for surface scrubbing.

Nevertheless, a large fraction of low energy photoelectrons are still moving across the beam pipe when the subsequent proton bunch is passing by. Therefore, this second bunch should accelerate them to energies which are sufficient for scrubbing. To evaluate the number of photoelectrons participating in the scrubbing effect a more detailed calculation

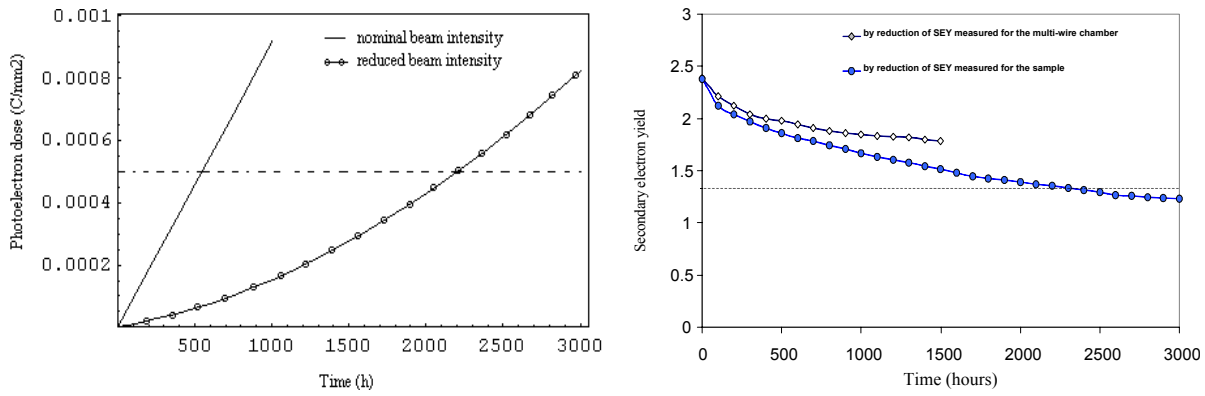

Figure 5-10: *LHC dipole sections: scrubbing time and reduction of the secondary yield.* Left: *comparison between the accumulated* photoelectron *dose as a function of time obtained at nominal beam parameters (left curve) and during the commissioning period (right curve).*
Right: *reduction of the secondary yield due to the photoelectrons during the commissioning period: considering the typical reduction rate of the SEY measured for a copper sample (lower curve) and for the multi-wire chamber (top curve).*

will be necessary; a difficulty in the calculation may arise in defining a threshold electron energy below which the electron conditioning is no longer effective.

Nevertheless, as discussed in section 5.2.4, the secondary electron yield is not permanently reduced by electron bombardment. If the system is left under vacuum, following a conditioning with an high electron dose, the multipacting threshold may decrease and some re-conditioning would again be necessary. A problem remains the surface recontamination, during venting of the system to air. It has been shown in section 5.2.1, that after venting the multi-wire chamber to air for a few days the multipacting current returns to its original value. If, after the commissioning period, some of the LHC sections need to be vented to air, scrubbing will again be necessary. In this case, dedicated conditioning runs, should be considered.

5.3 Freon plasma conditioning - CCl_3F

A Freon-vapor rf discharge processing method is a promising method in eliminating multipacting, as first observed by J.W. Noè. The reduction of multipacting is achieved by leaking Freon11 (CCl3F) vapor into a superconducting lead cavity, during a multipacting discharge [34].

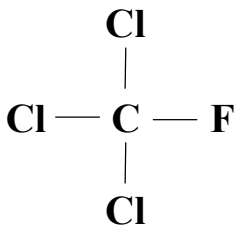

Figure 5-11: *Trichloromonofluoromethane - Freon11 (CCl_3F)*

Previously this novel method has been tested on this lead cavity only, but never on material such as stainless steel or copper. The objective was to verify the effectiveness of the freon plasma conditioning, and in particular, to study its effect on a copper surface.

I have arranged a glass bulb connected with a gas leak valve in the upper part of the multi-wire chamber[6], in order to let the freon vapour flow all along the chamber during the experiment, while the valve of the pumping system was open.

The minimum pulse amplitude to trigger multipacting, before the freon injection, was V_{p-p} =90V, and the base pressure ca. $3{\cdot}10^{-8}$ mbar. I could trigger multipacting by setting the electron current at the pick-up to 1μA.

When I reached a pressure of $5{\cdot}10^{-4}$ mbar by opening the freon leak valve, a series of current spikes were recorded at the pick-up, see Fig. 5-12, and a *blue flashing light* was visible inside the multi-wire chamber. The process lasted for a few seconds only, then abruptly multipacting stopped. The pulse amplitude must be increased to initiate again multipacting in the system. At this increased pulse amplitude the same effect could be observed. When setting a pressure of 10^{-3} mbar or higher, the current stabilized at the pick-up and a *bright stable light* was visible in the chamber. I have created in this way a freon plasma inside the chamber, which have been maintained for a few minutes[7]. After the freon plasma treatment[8], multipacting could no longer be observed even by setting the highest pulse amplitude. According to previous considerations given in section 4.2, I may conclude that, at this stage, the effective secondary electron yield of the chamber surface, is lower than 1.7.

[6]The first experiment was done with the stainless steel multi-wire chamber

[7]closing the freon gas leak valve, had little effect on the pressure; the light was still visible and the pressure was stable, an effect of ion trapping is possible in the plasma region. In order to stop the plasma it was necessary to switch off the RF.

[8]freon consumption during the experiment has been less than 1 mg; freon can be recovered, by a properly designed recovery system

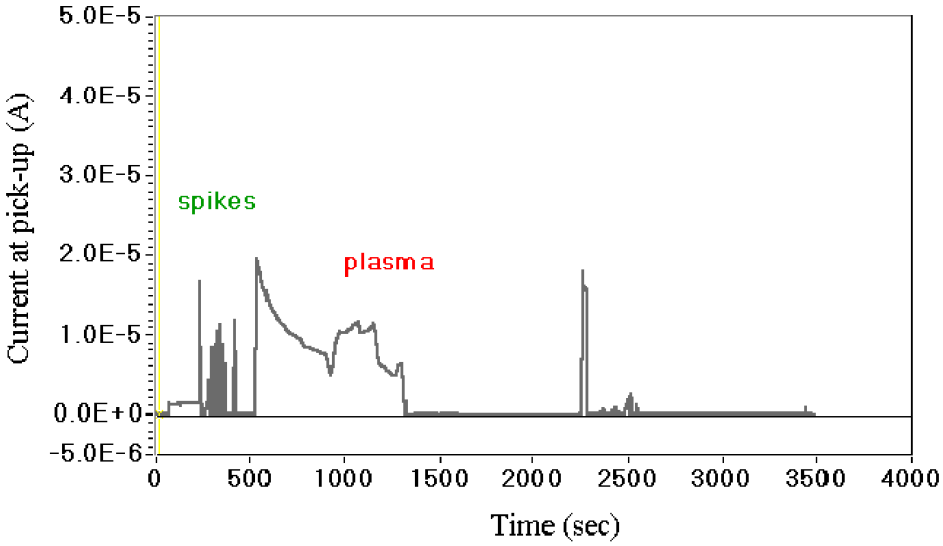

Figure 5-12: *First experiment with freon injection. Current spikes appear in the pressure range* $5{\cdot}10^{-4}mbar$, at higher pressure *the plasma regime takes place (between* $500 \div 1300$ sec)

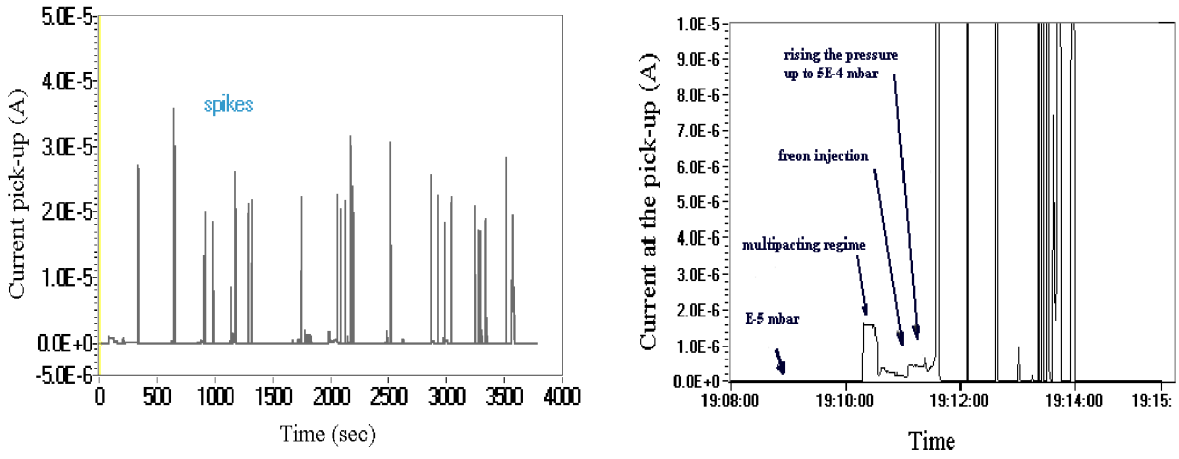

Figure 5-13: *Current recorded at the pick-up during the second freon injection. Pressure during injection is ca.* $5{\cdot}10^{-4}mbar$

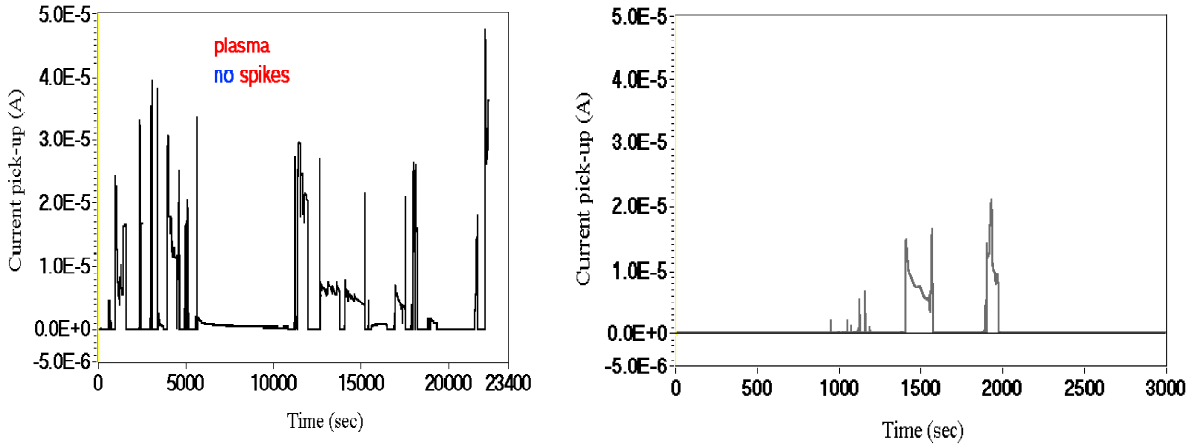

Figure 5-14: Left: *Argon discharge, multipacting is still present after a long exposure to the argon discharge. Pressure range between* $5 \cdot 10^{-4} mbar$ to $1 mbar$.
Right: Freon discharge on a copper surface.

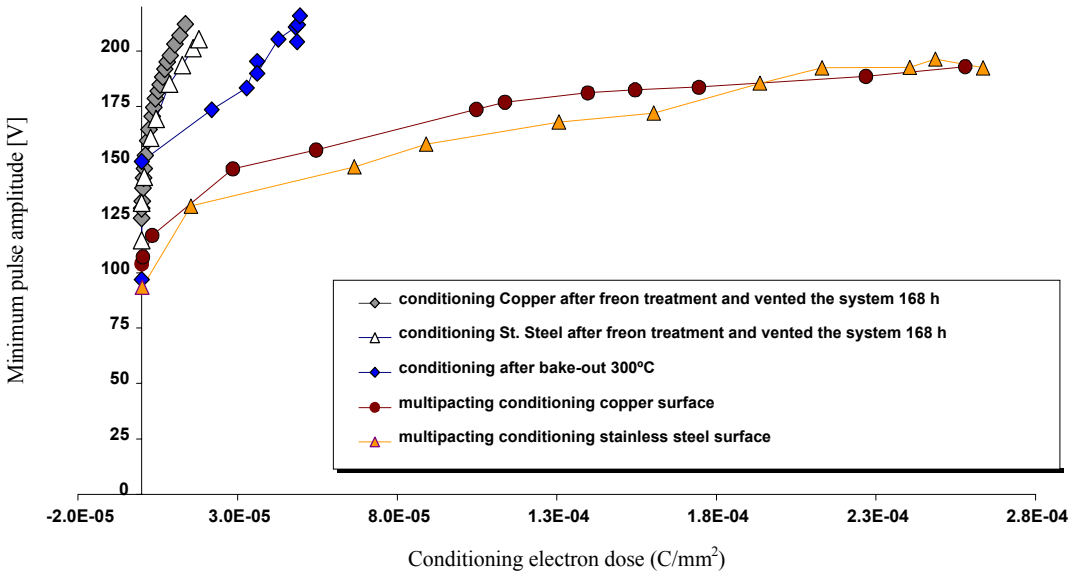

Figure 5-15: *Minimum pulse amplitude required for multipacting as a function of the integrated electron dose: conditioning after Freon11 plasma and after venting the system to air for one week (upper curves), compared with conditioning and conditioning after bake-out. After 1 week exposition to air the effect of freon is still visible*

In order to study the chemical effect of the freon plasma on the surface, samples have been introduced inside the multi-wire chamber during freon injection to be subsequently analyzed by Auger electron spectroscopy[9]; the experimental results are shown in section 5.7.

I have performed a second experiment on the stainless steel multi-wire chamber. In similar conditions as described above, I have injected freon setting a pressure in the chamber in the order of $5{\cdot}10^{-4}$ mbar. The aim was to reproduce only the behaviour of the current spikes, and to avoid to enter the pressure range of the plasma regime, e.g. 10^{-3} mbar or higher. After some minutes of processing under these conditions multipacting disappears, see Fig. 5-13.

During both experiments I have arranged a thermocouple inside the chamber to measure a temperature increase which could be due to the reaction of the freon radicals with the surface contaminants. A temperature rise of $0.6°C$ has been measured during both the experiments, but this seems not significant to justify the assumption.

Recently some tests [35] have shown that the freon treatment does not deteriorate, and may even improve, the performance of a superconducting cavity.

Memory effect after venting the system

To test the efficiency of the freon treatment after a long exposure of the surface to air, I have vented the chamber to atmospheric pressure with air for $168h$. Subsequently, multipacting is tested and the minimum pulse amplitude was found to be ca. V_{p-p} =110V. During the following multipacting conditioning I have verified that only little degradation of the surface occurs, as shown in Fig. 5-15. The conditioning dose necessary to eliminate multipacting from the multi-wire chamber was found to be less than $2{\cdot}10^{-5}C/mm^2$.

Argon injection

An effective way to reduce the secondary emission yield is ion bombardment of the surface. Since the effect of freon could be due to an ion discharge in the vacuum chamber in the presence of an RF field, I have injected argon during multipacting. Argon was injected in the same way as freon. The spikes could not be observed at any pressure, ranging from $10^{-5}mbar$ up to 1 mbar. The plasma could be operated with a stable luminescence inside

[9] we measured the SEY of a copper sample exposed to freon plasma conditioning. The sample has been extracted after venting the chamber to nitrogen, and it has been exposed to air ca. 25 min, before being introduced in the secondary yield experimental setup. The sample presents a $\delta_{\max} \lesssim 2$ ($E_{max} \approx 500eV$), while a reference OFHC copper sample presents a $\delta_{\max} = 2.35$ ($E_{max} \approx 350eV$). However, after baking to $300°C$, the sample exposed to the freon plasma presents a $\delta_{\max} \approx 1.3$, ($E_{max}$=600eV), against $\delta_{\max} = 1.9$ (E_{max}=400eV) measured for the reference sample. The relatively high initial secondary yield of the sample exposed to the freon plasma, is probably ascribed to direct exposition to air and related fast recontamination, during the transport of the sample. It is interesting to note that after baking the SEY drops down to 1.3, which is the secondary yield of a sputtered copper sample, free of contaminants.

the chamber. After a long exposure to the argon plasma, as shown on the left-hand side of Fig. 5-14[10], multipacting was found to be still present.

The bias-voltage is neutralized during the plasma regime. This is due to the presence of charged particles near the wires in the chamber. When the bias-voltage is neutralized, the RF pulse voltage corresponds to a *zero average* signal (*DC free* pulse - see appendix A). As a consequence, the net energy gain of the ions inside the chamber will be low and the ion bombardment will not be efficient.

Therefore, argon is not as effective as freon in conditioning the surface. The argon experiment furthermore suggests that during the freon injection some chemical changes may take place on the surface.

[10]Eventual presence of peaks on this figure have been obtained by switching on and off the RF, trying to reproduce with argon the spikes behaviour visible during the freon injection

5.4 Freon plasma conditioning of a copper surface

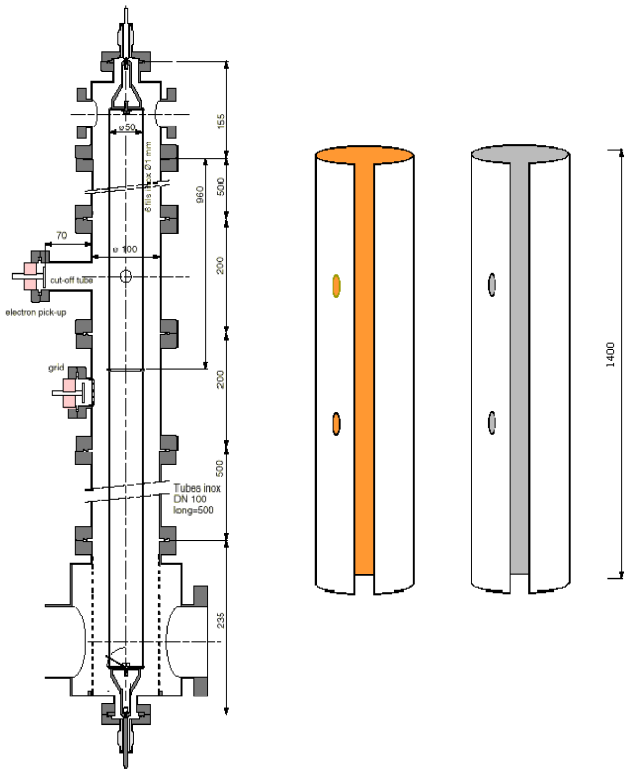

Figure 5-16: *The rolled sheets are introduced and fitted along the chamber in order to study the multipacting effect on different surfaces. The rolled sheets are made of pure OFHC copper, TiZrV NEG sputtered on stainless steel, and aluminium. At the level of the pick-up flanges, openings are made to measure the multipacting electrons.*

In order to study multipacting with different surface materials, I have built copper, stainless steel or aluminium made from ($100mm$ diam., $1.4m$ long) rolled sheets, which were introduced and fitted into the multi-wire chamber. The stainless steel sheet has been subsequently coated with a TiZrV non-evaporable getter alloy.

Copper and TiZrV getter alloy are the proposed LHC beam pipe materials. In the case of a copper surface the objectives were to study the multipacting conditioning, and the effectiveness of the freon plasma conditioning. A TiZrV getter material presents a very low secondary electron yield when it is activated. The aim was to activate the TiZrV getter *in-situ* and to verify the vanishing of the electron multiplication resonance.

The copper rolled sheet has been fitted in the multi-wire chamber, the conditioning of the surface is achieved with a multipacting electron dose of the same order of magnitude as for the stainless steel surface, as shown in Fig. 5-15.

Subsequently I have tested the freon plasma conditioning. The freon treatment has been found to proceed faster on the copper surface than on the stainless steel surface. Under the conditions of the earlier experiments, the same spikes appear at a threshold

pressure of $5{\cdot}10^{-4} mbar$. At higher pressures the plasma regime lasted a few minutes only, as shown on the right-hand side of Fig. 5-14, then multipacting was no more visible, even at the highest available pulse amplitude. Also in this case we can conclude that $\delta \max < 1.7$ has been achieved.

Following the freon plasma treatment I have vented the chamber to atmospheric pressure for 168h, then multipacting was checked again. Even for the copper surface the conditioning dose necessary to eliminate multipacting was low, as shown in Fig. 5-15, suggesting that little degradation of the surface occurs during exposure to air.

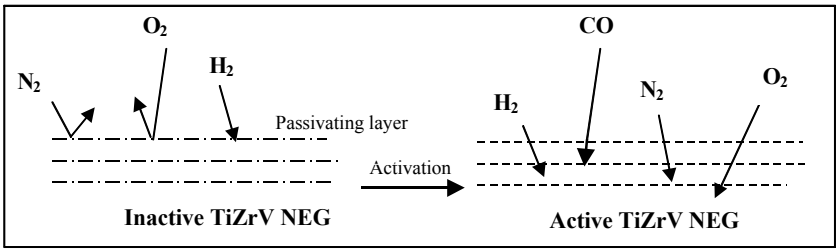

Figure 5-17: *NEG activation process.*

5.5 Thin film TiZrV Non Evaporable Getter (NEG) coating

A surface may provide a useful pumping action when able to retain adsorbed gas molecules. Getters materials are able to fix gas molecules on their surface in the form of stable chemical compounds. Getters are used as pumps as they react with gas molecules by two types of forces: chemical forces involving electrons, and Van der Waals forces. The first involves covalent or metallic bonding, generally with binding energies > 0.4 eV/molecule, while the second involves forces of electrostatic nature, e.g. dispersion polar forces, with binding energies < 0.4 eV/molecule.

For a molecule adsorbed on a surface at temperature T the escape probability is

$$\nu = \nu_0 e^{-\frac{E}{kT}}$$

with E the binding energy of the molecule, ν_0 the frequency of oscillation of a molecule on the surface, and $h\nu_0$ is in the order of the binding energy of the adsorbed molecule. The mean surface lifetime is given by Eq. (5.6), where a good pumping action is obtained when τ is larger than the duration of the experiment.

The getter surface must be clean to provide a large number of free adsorption sites. There are different ways to produce a clean getter surface:

- by in-situ deposition of a fresh getter film
- by heating the getter to a high temperatures so as to diffuse oxygen from the surface into the getter bulk

These two types of getter are called evaporable and non-evaporable getters (NEG), and for this latter getter the required temperature is called *activation temperature.* Activation is carried out by properly heating the NEG getter materials and promoting the diffusion of oxygen of the passivating surface layer until the surface is sufficiently clean to start sorbing the impinging gases, see Fig. 5-17.

Usually the NEG is an alloy containing zirconium, vanadium or titanium.

NEGs are usually produced by fixing a powder of the getter material to a metal substrate. After insertion in the system the activation is achieved by heating. If the getter

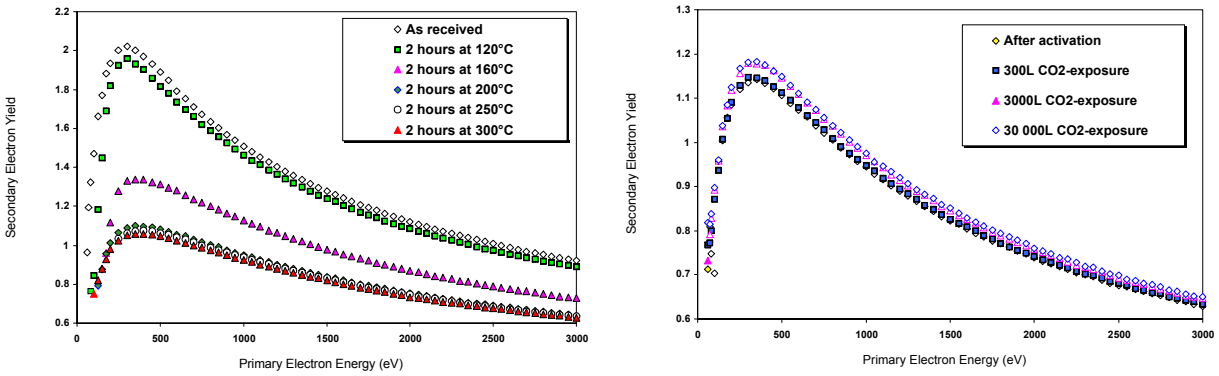

Figure 5-18: Left: *Secondary electron yield of TiZrV NEG on Cu, as received and after 120°C, 160°C, 200°C, 250°C and 300°C activation*
Right: *Influence of CO_2-exposure expressed in Langmuir (1L=1.33 10^{-6} mbar·1sec) on the SEY of activated TiZrV NEG* [33]

is working at room temperature no or very limited diffusivity (diffusion of chemisorbed species into the bulk) takes place. At high temperatures, the capacity is greatly enhanced since the diffusion of dissociatively chemisorbed species is promoted. In general the getter materials are studied with the aim to get a high diffusivity to increase both the sorption speed and the capacity. The performance of a given NEG depends on the activation temperature, sticking probability of gases, surface capacity, total pumping capacity (H_2 as reference).

Thin-film getter coatings, produced by sputtering, have been found to recover their chemical properties with a bake-out *in-situ,* after being exposed to air. The TiZrV getter alloy has a low activation temperature, around $200°C$, and a high sticking factor for H_2, it is at the moment under study in view of the future application for LHC, to be employed as beam pipe material. If the getter material is exposed to gases as CO or CO_2, with a partial pressure sufficient to form one monolayer on the getter surface, the chemical reactivity and the pumping action are drastically reduced [40], we are in presence of *saturation* of the NEG.

The advantage of the TiZrV getter is that after activation it presents a low secondary electron yield, as shown on the left-hand side of Fig. 5-18. The measurements performed at CERN [39] show that $\delta_{\max}$ decreases from an initial value larger than 2 to less than 1.1, after $200°C$ activation. The secondary emission yield of the TiZrV getter remains low even after saturation of the surface by means of CO_2 exposure, as shown on the right-hand side of Fig. 5-18.

In order to test multipacting with the TiZrV getter surface, I have fitted the TiZrV non-evaporable getter rolled sheet along the multi-chamber[11], see Fig. 5-16. After insertion in the system, the minimum pulse amplitude necessary to trigger multipacting was

[11]The impedance of the system has been measured slightly larger than the impedance of the chamber

measured to be $V_{p-p} \approx 110V$. This value is larger with respect to stainless steel, since an *as received* getter surface presents a secondary electron yield which is slightly lower than an *as received* stainless steel surface[12].

The whole system has been baked at $250°C$ for 24 hours. I have verified the absence of the electron multiplication resonance, due to the expected reduction of the secondary electron yield, by the NEG activation[13]. In order to study the recontamination of the getter surface, the system has been vented to atmospheric pressure with air for 720h. As a consequence of this treatment, I have measured minimum $V_{p-p} \approx 195V$ (near the limit of the available pulse amplitude). According to the estimations given in section 4.2, it follows that $\delta \simeq 1.8$. As a consequence, the recontamination for an activated TiZrV getter appears to be very low.

To determine the threshold temperature necessary to eliminate multipacting, which should be comparable to the NEG activation temperature, I have introduced in the chamber a second TiZrV rolled sheet replacing the first one. The aim was to increase the temperature in step of $30°C$ until multipacting was no more present in the system. Before the first NEG activation the multipacting threshold was $V_{p-p} \approx 120V$.

Baking at $150°C$ for $12h$, I have verified that multipacting is reduced in strength but is still present[14] in the system. Next, the temperature has been increased, and I have verified that $180°C$ for $12h$ was the lowest temperature for which multipacting could be entirely suppressed in the multi-wire chamber.

The system has then been baked at an activation temperature of $220°C$, followed by venting to atmospheric pressure for 168h. Under these conditions, multipacting was weakly present at the highest available pulse amplitude $V_{p-p} = 210V$. At this stage, the secondary electron yield of the TiZrV surface can be estimated as $\delta_{\max} \lesssim 1.7$.

---

before the TiZrV sheet insertion. To measure the line impedance a reflectometer method has been used.

[12] depending on the exposition time to air after the deposition of the film getter material. Generally the SEY for TiZrV is in the range $1.8 < \delta_{\max} < 2.2$ against $\delta_{\max} = 2.4 \pm 0.1$ of the stainless steel.

[13] The pressure in the multi-wire chamber, immediately after the NEG activation, is not as low as expected and, this could be caused by the fact that after activation the NEG has experienced saturation due to a possible source of gas in the system. Since the secondary electron yield remains low even after saturation, multipacting should not be affected by this latter effect.

[14] the minimum $V_{p-p} \approx 150$V, which corresponds to $\delta_{\max} \approx 2$

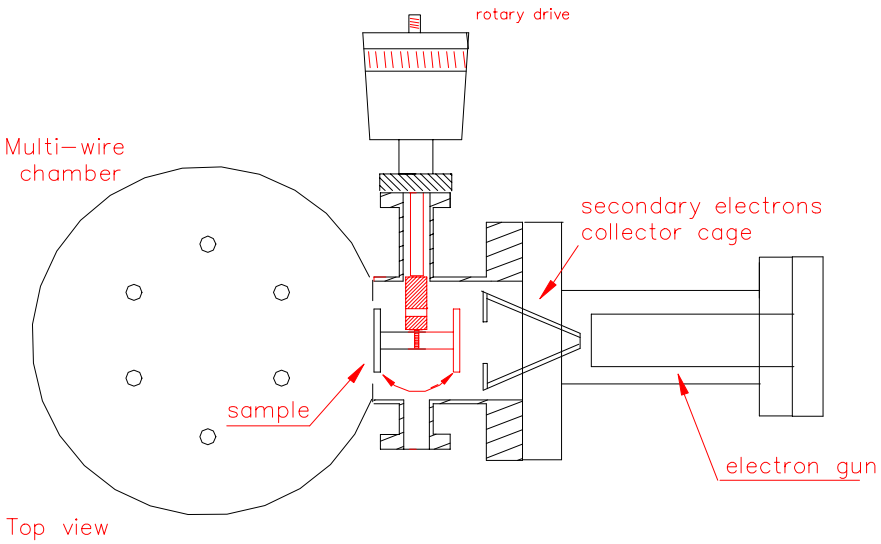

Figure 5-19: *Top view of the experimental set-up to measure the secondary electron yield in the multi-wire chamber*

5.6 Measurement of the secondary electron yield

5.6.1 Experimental set-up and calibration of the system

The objective was to measure the reduction of the secondary electron yield during multipacting conditioning on different samples arranged in the multi-wire chamber.

I have built the system to measure the SEY in the multi-wire chamber, shown in principle in Fig. 5-19. The sample faces the internal part of the experimental chamber during multipacting. From time to time to measure the SEY the sample is turned, by means of a rotary sample holder, to face the secondary electron yield apparatus. Monitoring the reduction of the SEY as a function of the multipacting conditioning electron dose is possible without exposing the sample to air.

The apparatus to measure the SEY shown in Fig. 5-20 and on the left-hand side of Fig. 5-21, consists primarily of an electron gun and a collector for the emitted secondary electrons. The rotary sample holder allows to charge the experiment with two samples at a time.

The electron are accelerated in the electron gun to energies between $60eV$ and $3keV$. They are guided by electrostatic deflection plates through a hole in the collector onto the sample. The collector is positively biased with respect to ground in order to collect all the secondary electrons emitted by the sample and to re-capture the secondary electrons emitted by the collector itself. Only a very small fraction of backscattered electrons can escape. The sample current i_s and the collector current i_c are measured simultaneously. The SEY is calculated as:

$$\delta = \frac{i_c}{i_c + i_s}$$

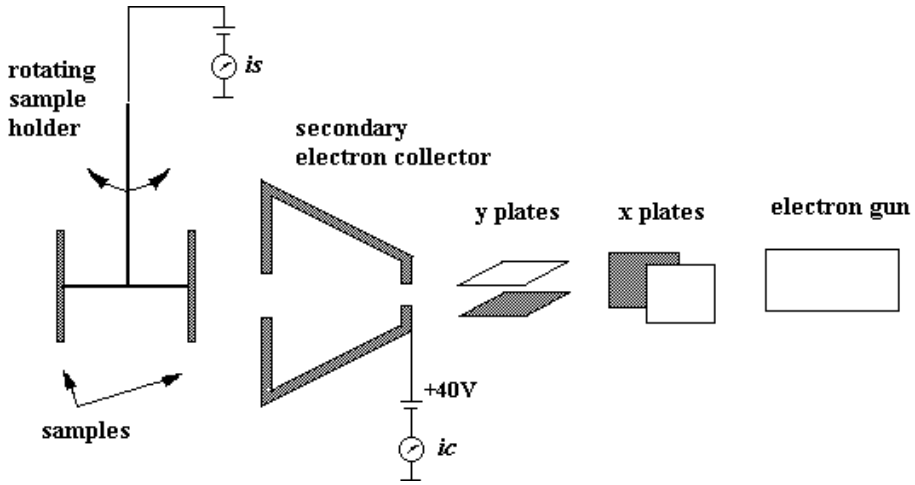

Figure 5-20: *Schematic of the experimental set-up to measure the SEY*

where the sum of the sample current and of the collector current represents the primary beam current. The SEY of the material can be changed by primary electron bombardment. To avoid this effect, a low primary electron current typically 5 $10^{-9}A$ with a pulse length of $200 \div 300ms$ are used to obtain a sufficiently high signal to noise ratio, but without affecting the SEY by the primary electron bombardment.

The experimental set-up has been tested and the result of the measurement of the secondary electron yield for a copper sample is shown on the right of Fig. 5-21. The apparatus will also be used to measure the SEY during the freon plasma conditioning method.

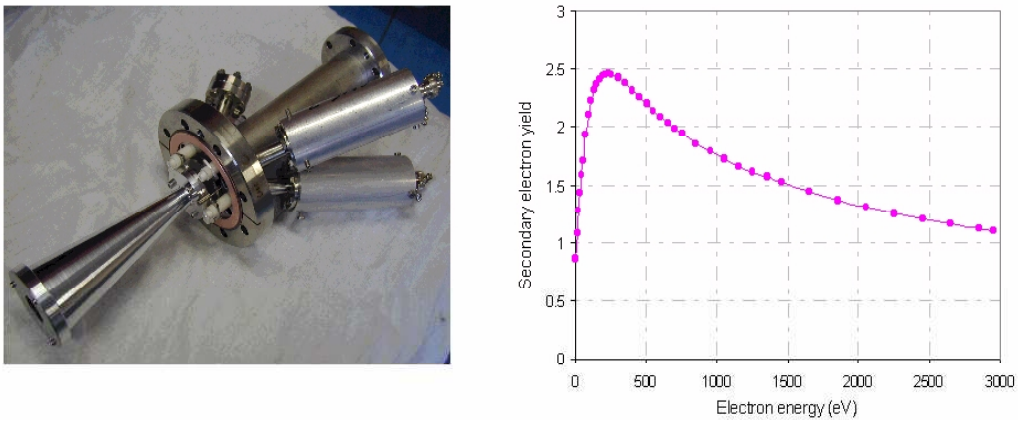

Figure 5-21: *Secondary yield apparatus and test result of the SEY for an* as received *copper sample*

5.7 Auger electron spectroscopy analysis

Introduction

Even if the variation of δ_{SEY} during multipacting, and by electron bombardment is well known, the physical reason for this decrease is not well understood. As discussed in the preceding section 5.2.3, and shown in Fig. 5-8, the secondary electron yield decreases for copper to $\delta_{\max} \lesssim 1.1$, under the effect of electron bombardment.

Electron beam stimulated desorption (ESD) of adsorbed molecules from the surface may result in a decrease of the secondary electron yield due to the removal of contaminants causing an high SEY.

However the experimental evidence is not in agreement with this simple model.

Following an exposure to a high electron dose, a SEY which is even lower than for the pure material is obtained; the SEY for a pure, cleaned copper is $\delta_{\max} = 1.3$, while for a copper sample exposed to electron beam conditioning $\delta_{\max} \lesssim 1.1$. This anomalous decrease, below the secondary electron yield of the pure material, suggests that scrubbing is not only and simply a *cleaning* effect due to desorption of contaminants from the surface [54].

Motivated by the fact that beam scrubbing is one of the most promising ways to condition *in-situ* the LHC beam screen, Auger electron spectroscopy analysis of samples exposed to different multipacting electron doses have been performed.

In addition, and to better understand the freon plasma effect, both stainless steel and copper samples, exposed to the freon plasma, have been analyzed by Auger electron spectroscopy.

A brief introduction to the Auger electron spectroscopy technique, to characterise a surface, will be given here:

Auger electron spectroscopy (AES)

Auger electron emission is initiated by the creation of an ion with an inner shell vacancy. Auger electrons are emitted in the relaxation of the excited ion. In this process an electron from a higher lying energy level fills the inner vacancy with the simultaneous emission of an Auger electron. This simultaneous two electron coulombic rearrangement results in a final state with two vacancies. Auger electrons identify the emitting atoms[15]. When the Auger transitions occurs whitin a few angstroms of the surface, the Auger electrons may be ejected from the surface without loss of energy and contribute to the total spectrum of secondary electrons at a distinct characteristic energy. The Auger peaks appearing in the energy distribution N(E) are small compared with the background current and the use of N(E) is in general inadequate for analytical purposes. Instead the differential distribution dN(E)/dE is recorded. The differentiation can largely eliminate the background and makes the peaks more clear to identify. Since the escape depth of the

[15] Auger electron emission is one of the two relaxation mechanisms possible in an excited ion, the other is X ray fluorescence. In the low-Z elements, the probability is greater that an Auger transition occurs, whereas X-ray emission is favoured for high-Z elements.

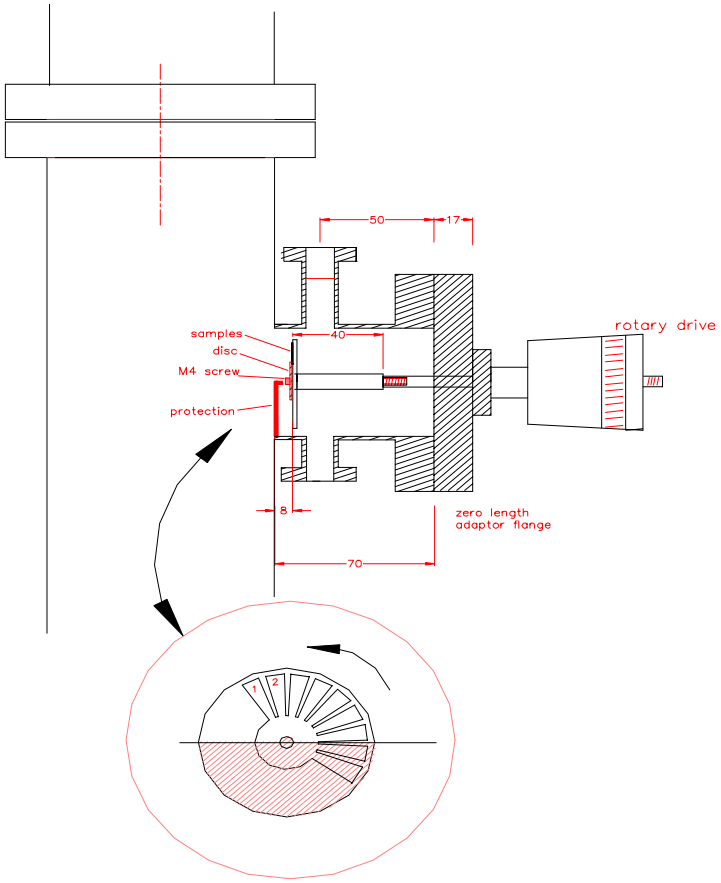

Figure 5-22: *Rotary drive support. Samples are covered by a stainless steel foil behind the lower half part which protects them from multipacting. By rotating the holder samples are uncovered and exposed to different electron doses.*

Auger electrons is only few atomic layers, AES has a high depth resolution. A depth profile can be obtained when the surface layers are continuously removed by sputter etching and the Auger peaks for the elements of interest are monitored simultaneously. Apart from hydrogen and helium all elements can be detected by AES. A more detailed description of AES technique is given in references [22][47].

5.7.1 Electron cloud scrubbing effect

In order to expose stainless steel samples to different electron doses during multipacting I have built a rotary holder support system, Fig. 5-22. Only one sample is exposed initially to the electron bombardment, while the other samples are covered by a stainless steel foil, situated in the lower half part.

The samples are subsequently uncovered, thus exposed to different electron doses. After conditioning, the chamber is vented with nitrogen. The samples are transported under nitrogen atmosphere and introduced in the Auger electron spectroscopy apparatus. In this

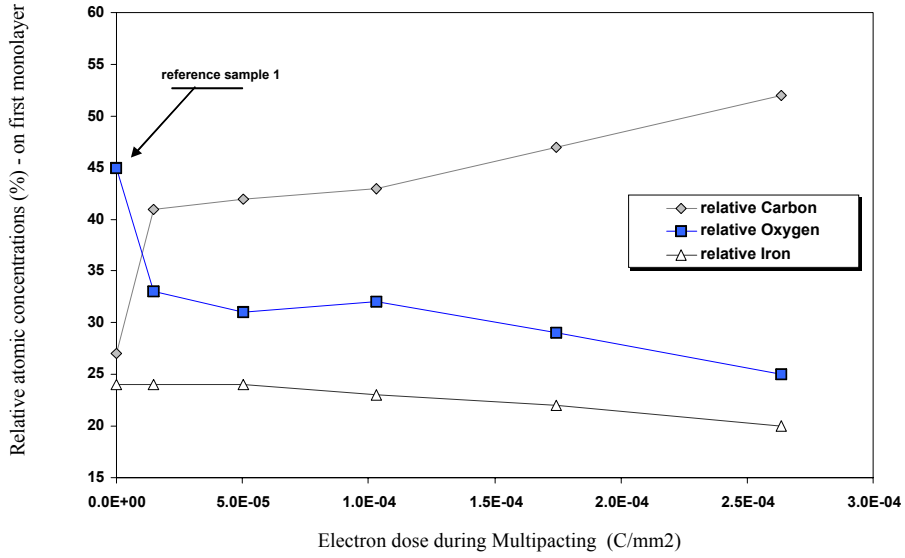

Figure 5-23: *Results of the Auger electron spectroscopy indicate that the relative carbon atomic concentration on the surface increases during electron bombardment while that of oxygen decreases. The first monolayer relative concentrations are shown. Although these are relative measurements, one may infer that both effects occur since the iron concentration remains essentially constant. The exact behaviour of the carbon and oxygen curves shown in figure is typical, and it has been observed in different measurements.*

way they are only weakly contaminated by the unavoidable exposure to air[16]. Results of the Auger electron spectroscopy show that the relative carbon atomic concentration on the surface increases during electron bombardment while that of oxygen decreases, see Fig. 5-23. Although these are relative measurements, one may infer that both the effects occur since the iron concentration remains essentially constant.

Auger spectrum are also shown in Fig. 5-25.

The maximum secondary electron yield for carbon varies between 0.5 and 1 [48], depending whether if it is in the form of soot or of graphitic.

An explanation of the carbon increase could be as follows: residual hydrocarbon molecules remain in the chamber even at low pressures (10^{-9} mbar), and are decomposed by cracking due to the energetic multipacting electrons. The resulting volatile components are evacuated by the pumping system, while non-volatile material deposits as carbon on the surface. As a result, a low SEY surface layer appears, on the chamber surface exposed to the electron bombardment.

Not only the primary electrons, but also the secondary electrons produced near the

[16]The samples are extracted from the chamber in an inert atmosphere, obtained inflating *nitrogen* in a glove bag wrapped around the extraction flange; the samples are then carried in a nitrogen atmosphere to the Auger spectroscopy laboratory and rapidly introduced in the Auger spectroscopy apparatus to be analyzed.

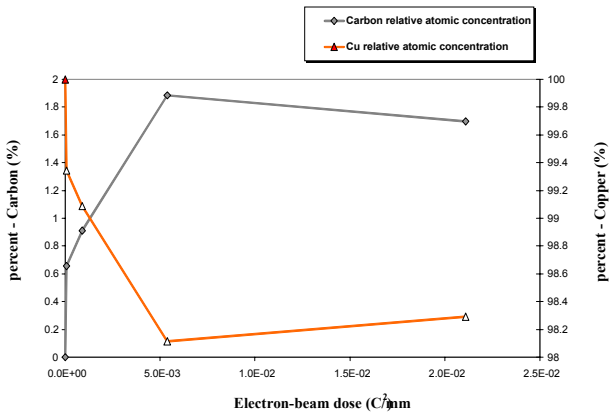

Figure 5-24: *Carbon growth induced by electron-beam on a pure Cu sputtered sample, monitored in AES* [49]

surface are responsible of the build up of this deposit, as the low energy secondary electrons have a significantly larger cross section for interacting with material. Considering a CO molecule, the dissociation of the molecule takes place at the threshold energy of $12eV$, and hence, the dissociation probability is high also for secondary electrons.

During multipacting both the desorption of contaminants causing a high SEY, and the build-up of a carbon layer, with $\delta < 1$, lead to the reduction of the secondary electron yield of the area exposed to the electron bombardment. In the multi-wire chamber, since the SEY decreases, the multipacting intensity also decreases. Thus, the desorption of contaminants and the building-up of the carbon deposit are reduced, in a process that, in turn, causes the decrease of the multipacting in the system.

Measurements performed *in situ* in the Auger spectroscopy apparatus [49] on a Cu sample which was previously sputtered with ions, resulting in a clean, pure copper surface (Cu 100%), confirm the carbon growth induced by an electron-beam, as shown in Fig. 5-24. In the same system, a measurement on a pure silicon wafer, did not show the carbon growth, probably due to the fact that oxides are tightly bound to the silicon crystal.

A bibliographic research has confirmed the hypotesis that a carbon growth takes place under electron bombardment. This effect is directly related to the fabrication process of carbonaceous nano-structures by electron-beam-induced deposition (EBID), to produce tips and wires suitable for imaging in atomic force microscopy [50][51][52]. In addition, the electron-beam deposition is a well-established technique for high resolution material deposition from the gas phase onto a substrate, where a finely focused electron beam locally decomposes gas molecules which are then adsorbed on the sample surface. The growth rate and the shape of carbon tips and wires, with sizes and lengths in the order of tens of nm, can be exactly defined, as they are influenced by the parameters of the incident electron beam, e.g. the electron energy, beam current, electron dose and the working distance. The carbon growth is obtained by employing the residual gas in the vacuum system as a source material. It is found that an increasing beam current leads to a

decrease in the length growth probably due to enhanced thermal desorption of adsorbates and due to a reduced sticking coefficient [53].

As a conclusion, the secondary electron yield decreases during multipacting conditioning, and electron beam bombardment, due to two different simultaneous surface effects[17]:

- the removal of contaminants from the surface responsible for a high secondary electron yield
- the formation of a carbon layer with a secondary electron yield lower than 1.

5.7.2 Samples exposed to freon plasma conditioning

Before the first freon injection, described in section 5.3, I have introduced five samples inside the multi-wire chamber, in order to study the surface composition by means of Auger spectroscopy. Results of the Auger analysis are compared with the analysis for the reference samples which were cleaned in the same way but not exposed to the freon plasma.

Three OFHC copper and two stainless steel samples were exposed to the multipacting electrons, during freon injection[18].

Table 2 shows the relative *atomic* concentrations (%) on the OHFC copper surface, *exposed* and *not exposed* to the freon plasma (*reference*). Table 3 shows the related depth profiles for the copper surface samples. Oxides are no more present on the surface of the Cu samples after exposure to the freon plasma, while chlorine is found up to a considerable depth (ca.300Å). In addition, carbon has been significantly reduced, indicating that a *cleaning* effect has occurred on the copper. The color of the copper surface is clearly changed (to rose) on the region exposed to the freon plasma.

Table 4 shows the relative *atomic* concentrations (%) for the stainless steel surface, *exposed* and *not exposed* to the freon plasma. Table 5 shows the related concentration *thickness* (depth corresponding to half of the initial concentration) on the stainless steel samples. Freon radicals react rather differently on the stainless steel surface: carbon has been deposited (atom. conc. 74%) on the surface, probably originating from cracking of the freon molecules. The reduction of oxides is marked on the stainless steel sample but chlorine is present at the few percent level only.

It is interesting to note that fluorine is absent in all the samples.

The atomic concentrations as a function of depth for the *as received* and *exposed to the freon plasma* copper samples, are shown at the top of Fig. 5-26. The lower part of Fig. 5-26 shows the atomic concentrations as a function of depth for *as received* and *exposed to the freon plasma*, stainless steel samples. The Auger spectra are also shown in Fig. 5-25.

[17] in order of importance. The exact relative contribution of the two effects is difficult to estimate.

[18] three Cu samples are respectively chemically cleaned, alcohol cleaned and not cleaned Stainless steel sample are respectively chemically cleaned and cleaned only with alcohol; (although all the samples were chemically cleaned some months before, and then kept in the laboratory, exposed to air)
Chemical cleaning consists in exposing the samples to a perchloroethylen vapour for 5 cycles of 20 min/cycle, following ultrasound with ALMECO, a bath in demineralized water and finally they are introduced in an oven for $1^h and$ 30min .

I may conclude from the Auger spectroscopy analysis, that on the copper the freon plasma conditioning, surface, results in a decrease of the secondary electron yield due to the removal of the surface contaminants, and to an increased content of chlorine; a real *cleaning* effect occurred on the copper surface. On the stainless steel sample both effect occur a large carbon deposition, presenting a low SEY, and a partial surface *cleaning*[19].

5.7.3 Effect of freon plasma on the surface during multipacting

Table 1 shows the appearance energy for the CCl_3F products. The ionization energy for freon11 is ca. $11.5eV$ [41].

During the multipacting discharge the electrons travel across the multi-wire chamber with an energy of the order of $100eV$, as shown in Fig. 4-8. Each electron may ionize different atoms and produce several radicals of freon by cracking the CCl_3F molecules, as the threshold production energy ranges between $11.5eV$ and $20.5eV$. Chlorine and fluorine are halogen atoms with the highest electron affinity, since they have one electron less than the following noble gases. Radicals of freon contains chlorine and fluorine, react on the vacuum chamber surface with contaminating molecules such as oxides, hydroxides, hydrocarbons to form stable molecular compounds. The reaction products which are gases may be evacuated from the multi-wire chamber by the pumping system. Hence, an effect of cleaning may occur, which may result in a reduction of the secondary electron yield. This effect is experimentally more evident on copper than on stainless steel.

A known chemical compound which has a high affinity to react with water adsorbed on a surface is dichloropropane. The reaction involving mainly CCl_2 (between freon products, see Table 1)

$$(CH_3)_2CCl_2 + H_2O \rightarrow (CH_3)_2C = O + 2HCl \tag{5.12}$$

is claimed to reduce the base pressure in a vacuum system by a factor of 80 (alternatively carbon-fluoride formed with fluorine and carbon monoxide, is a very strong decomposing reagent of water $COF_2 + H_2O \rightarrow CO_2 + 2HCl$ with an enthalpy of reaction $\Delta H = -12.5kCal/mol$) [36][37]. The reaction energy in (5.12) is supplied by heating at moderate temperature.

During a freon plasma treatment the production of radicals could also be achieved by photo-dissociation due to radiofrequency or by heating of the vacuum chamber instead of by cracking with the multipacting electrons.

[19] In section 5.7.1, I have advanced the hypothesis that multipacting conditioning is due primarily to a *cleaning* effect, due to electron desorption, and simultaneously to a *building-up* of a carbon layer. This scenario would justify the faster freon plasma conditioning of the copper surface than on the stainless steel surface (carbon deposition), see section 5.4.

Appearance Energy determinations[20]

Ion	AE (eV)	Other Products	Method	Reference	comm.
CCl+	20.00 ±0.20	2Cl+F	PI	S Schenk et al., [42]	LLK
CCl+	20.5	2Cl+F	PI	J Jochims et al., [41]	LLK
CCl2+	17.0	FCl	PI	J Jochims et al., [41]	LLK
CCl2+	17.12 ±0.04	Cl+F	PI	A Ajello et al., [43]	LLK
CCl3+	13.50	F	PI	J Jochims et al., [41]	LLK
CCl3+	13.25 ±0.04	F	PI	A Ajello et al., [43]	LLK
CCl3+	12.77 ±0.15	F	EI	Curran [44]	RDSH
CF+	15.61 ±0.05	3Cl	PI	Schenkel et al., [42]	LLK
CF+	15.7	Cl2+Cl	PI	Jochims et al., [41]	LLK
CF+	18.35	3Cl	PI	Jochims et al., [41]	LLK
CFCl+	15.95 ±0.05	Cl2	PI	Schenk et al., [42]	LLK
CFCl+	16.0	Cl2	PI	Jochims et al., [41]	LLK
CFCl+	16.02 ±0.04	Cl2	PI	Ajello et al., [43]	LLK
CFCl+	17.1 ±0.1	2Cl	EI	Syrvatka et al., [45]	LLK
CFCl+	17.41 ±0.15	?	EI	Curran [44]	RDSH
CFCl2+	11.65	Cl	PI	Jochims et al., [41]	LLK
CFCl2+	11.57 ±0.04	Cl	PI	Ajello et al., [43]	LLK
CFCl2+	11.97 ±0.07	Cl	EI	Curran [44]	RDSH
Cl+	13.7 ±0.5	F(-)+CCl2	PI	Schenk et al., [42]	LLK
Cl+	15.20 ±0.10	F(-)+CCl2	PI	Schenk et al., [42]	LLK
Cl+	15.6 ±0.1	Cl(-)+CFCl	PI	Schenk et al., [42]	LLK

Table 1: *Appearance Energy determinations for Trichloromonofluoromethane* **[46]**

[20] *EI Electron impact techniques ("Electron impact")*
PI Photoionization mass spectrometry
Data compiled as indicated in comments:
LLK - S.G. Lias, R.D. Levin, and S.A. Kafafi
RDSH - H.M. Rosenstock, K. Draxl, B.W. Steiner, and J.T. Herron

Results of the Auger analysis are shown in the following tables, for 3 copper samples chemically-cleaned, alcohol-cleaned and not-cleaned, and for 2 stainless steel samples chemically-cleaned and alcohol-cleaned, compared with the same number of reference samples, which were not exposed to freon plasma.

	freon *plasma*	C (%)	O (%)	Cu (%)	Cl (%)	others[21] (%)
Cu *chem. cleaned*	*reference*	11	40	47	–	2
	exposed	**5**	**none**	**64**	**31**	–
Cu *alc. cleaned*	*reference*	44	22	32	trace	2
	exposed	**10**	**none**	**55**	**35**	–
Cu *not cleaned*	reference	55	10	32	1	2
	exposed	**7**	**none**	**63**	**30**	–

Table 2: Auger spectroscopy results of the Cu samples for the first freon treatment giving the atomic concentration (%) of the first monolayers. Independently from the cleaning method, oxides (and water) are no longer present after the freon plasma treatment, hydrocarbons are consistently reduced while chlorine is present in a significant amount.

	freon *plasma*	C *thickn.* (Å)	O *thickn.* (Å)	Cl *thickn.* (Å)
Cu *chem. cleaned*	*reference*	30	29	–
	exposed	**few**	=	**267**
Cu *alc. cleaned*	*reference*	18	31	–
	exposed	**few**	=	**294**
Cu *not cleaned*	reference	18	29	–
	exposed	**few**	=	**218**

Table3: Concentration thickness for C, O and Cl on the Cu samples. Chlorine is present up to a large depth, hydrocarbons have been strongly reduced, oxides are completely removed

[21] 'others' refer to *Ca* in the chemically cleaned copper sample, and to $S+N$ for the alcohol and not cleaned samples

.

	freon *plasma*	C (%)	O (%)	Fe (%)	Cl (%)	others[22](%)
St. st. *che. clean.*	*reference*	32	43	22	–	3
	exposed	**74**	**12**	**7**	**4**	**3**
St. st. *alc. clean*	reference	40	34	19	–	7
	exposed	**79**	**7**	**5**	**5**	**4**

Table 4: Auger spectroscopy results for the first freon treatment for Stainless steel. Atomic concentration (%) on the first monolayer. Independently from the cleaning method, carbon has been deposited on the surface, oxides consistently reduced and chlorine is present in small amount only

	freon *plasma*	C *thickn.* (Å)	O *thickn.* (Å)	Cl *thickn.*(Å)
St. st. *che. clean.*	*reference*	25	36	–
	exposed	**37**	**47**	**18**
St. st. *alc. clean.*	*reference*	32	42	–
	exposed	**40**	**40**	**33**

Table5: Concentration thickness for C, O and Cl on the stainless steel surface samples.

[22]'others' refer to *Ni+N* on the chemically cleaned stainless steel sample, and to *S+Ni+Ca* for the alcohol cleaned sample

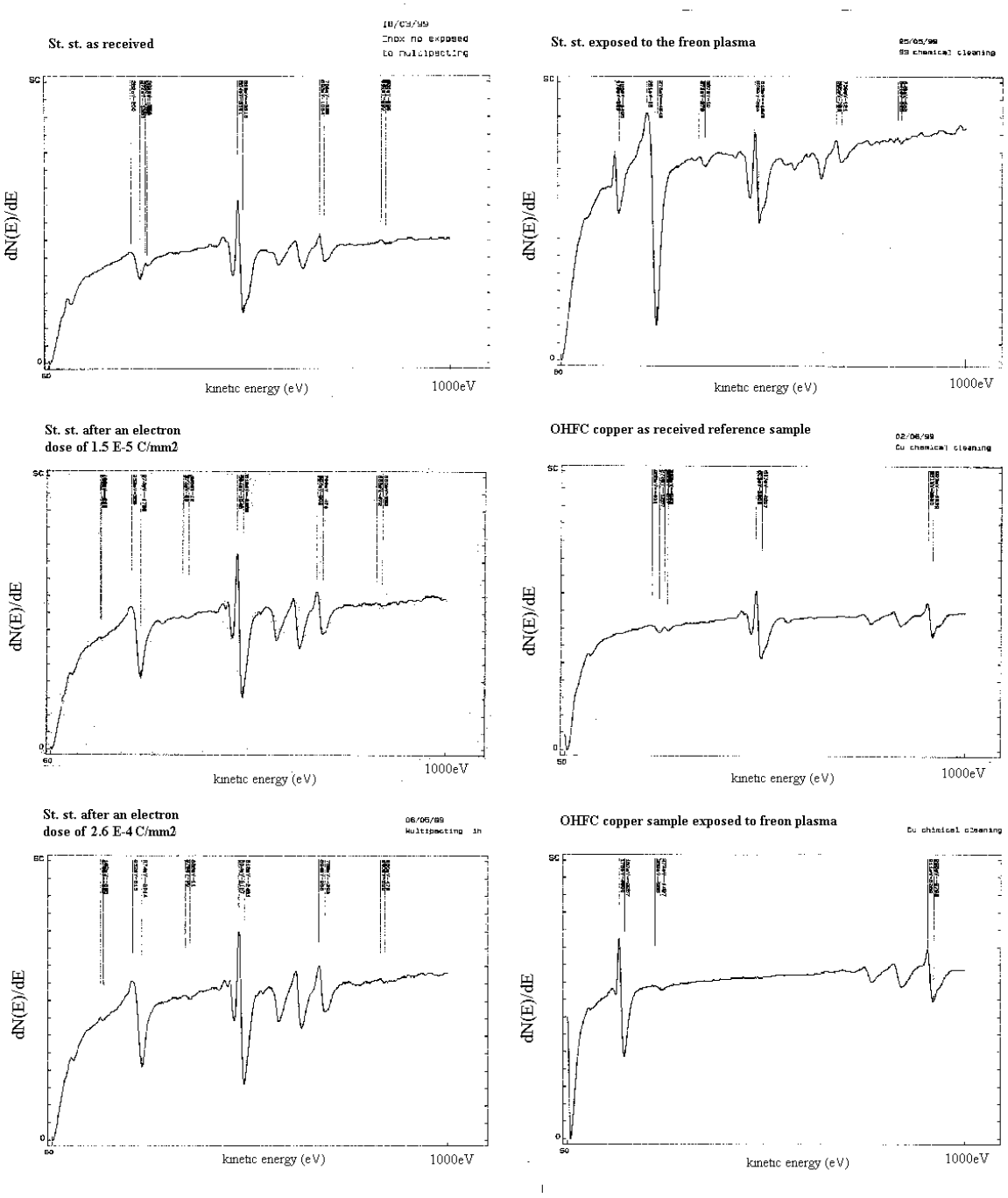

Figure 5-25: *Auger analysis of samples exposed to different electron doses, and to freon plasma conditioning. The peaks at 185eV, 275eV, 517eV, 700eV and 921eV are characteristic for chlorine, carbon, oxygen, iron and copper respectively.*
Top left*: as received Stainless steel (st.st.) reference sample* Center left*: St.st. after a dose of* $1.5 \cdot 10^{-5} C/mm^2$ Below left*: St.st. after a dose of* $2.6 \cdot 10^{-5} C/mm^2$
Top right*: St.st. sample exposed to freon plasma.* Center right*: as received copper reference sample* Below right*: Copper sample exposed to freon plasma.*

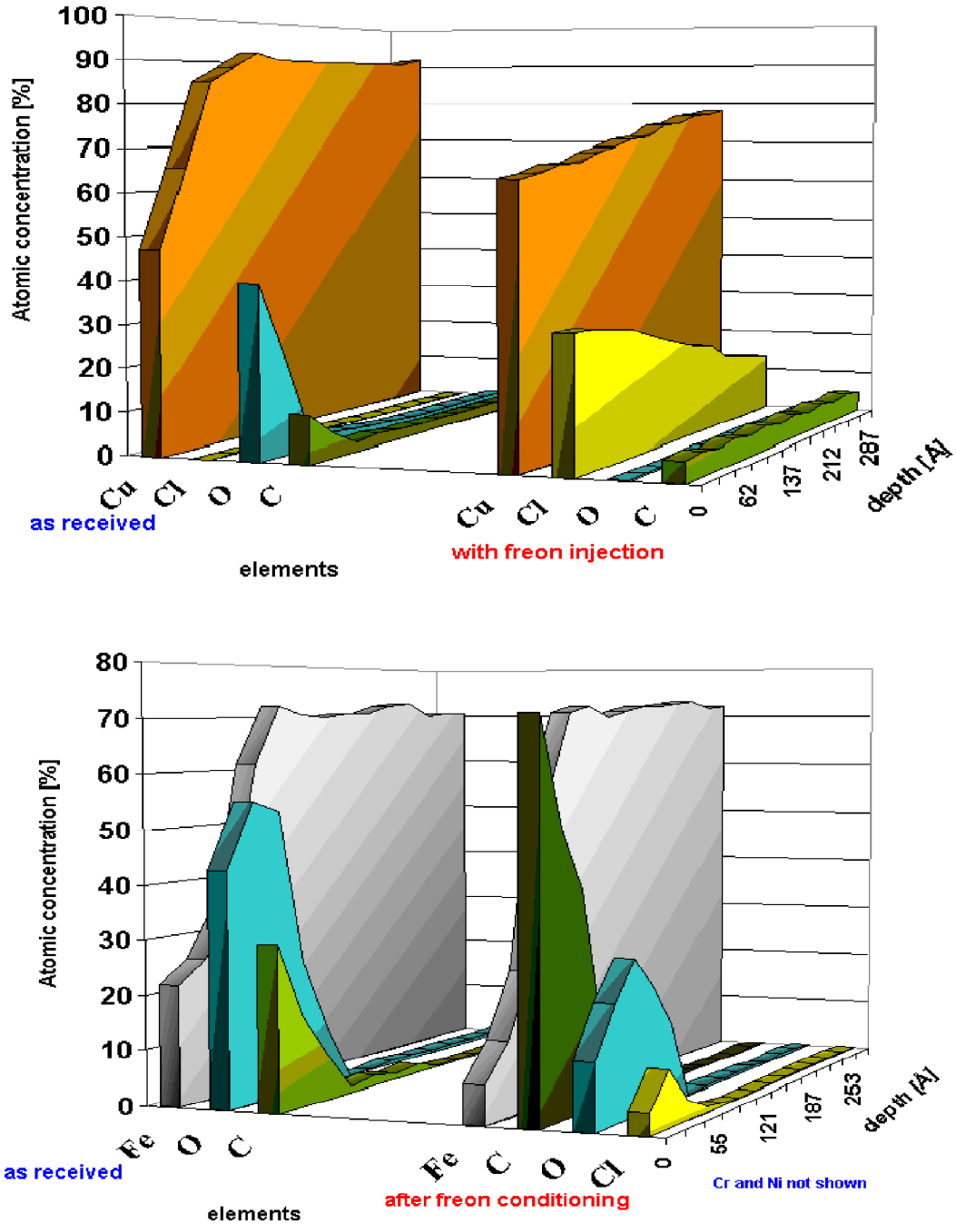

Figure 5-26: *Atomic concentrations as a function of depth: Auger spectroscopy analysis of* chemically clened *copper and stainless steel samples.*
Top: *copper samples as received* and *exposed to the freon plasma.*
Lower: *stainless steel samples as received* and *exposed to the freon plasma.*

Chapter 6

Suppression of multipacting with a solenoid magnetic field

Introduction

The effect of a solenoid magnetic field on the electron cloud in the travelling-wave multiwire chamber has been investigated.

Multipacting with electrons of relatively low energy - in the order of 100 eV as in the experimental chamber, see Fig. 4-6 - can be strongly influenced by an external magnetic field. Even in presence of a low magnetic field the resonance conditions for multipacting may no longer be fulfilled and, as a result, a suppression of the multipacting process is achieved[1].

The axial magnetic field was produced by a coil wound along the chamber. In the travelling-wave system I have found that a complete suppression of the electron multiplication can be achieved with a magnetic field of only 5 Gauss.

Since in the case of LHC the 8.4 Tesla dipole magnetic field forces the electrons to move in the vertical plane along the magnetic field lines during multipacting, any additional solenoid magnetic field in the dipoles would not be effective. A solenoid field would be useful to suppress multipacting at the LHC straight sections where the dipole magnetic field is absent.

The experimental setup is discussed in section 6.1, where the experimental results are also presented; in section 6.2 a simple model is discussed, and the possibility to use a solenoid in the field-free regions of the LHC is analysed in section 6.3, toghether with an estimate of the magnetic field which is necessary to suppress the electron multiplication resonance.

[1] for a defined pulse period

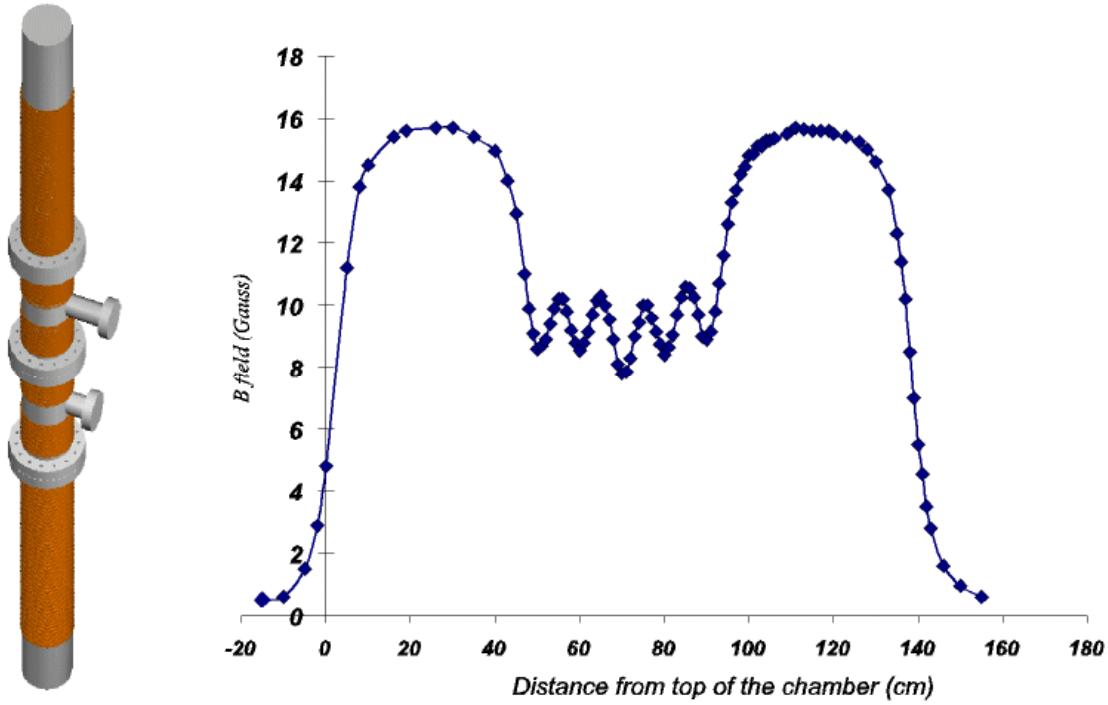

Figure 6-1: *Coil wound around the multi-wire chamber, and the measured solenoid field B_z, per Ampere.*

6.1 Solenoid magnetic field experimental setup and measurement

A solenoid coil with a 0.75 mm diameter insulated Cu wire has been wound along the 1.4 m long cavity. I assume that, though the wire makes a small helical angle with the cross-sectional plane, I can adequately model the coil with a circumferential current. The current flowing around the solenoid per meter is nI, where n is the number of turns per meter and I is the current in each turn. For a solenoid of infinite length the magnetic flux density along the chamber axis, is given by $B_z = \mu_0 nI$.

In our case $n = 1333$ turns per meter, therefore the field should be B_z=16.7 $10^{-4}T$ per Ampere of current in the solenoid.

In the central region of the chamber, shown on the *left*-hand side of Fig. 6-1, the flanges do not permit to wind a perfect solenoid. Thus B_z is not constant along the chamber. The magnetic field has been measured along the axis, by means of a Hall probe. I have introduced the probe in a tube of non-magnetic material, properly centered in the chamber, and measured the B_z component all along the z-axis of the chamber. A map of the magnetic field is shown on the *right* of Fig. 6-1. The field decreases at the level of the central flange regions where no coil turns are present.

The ratio between the length of the longest parts of the solenoid and the solenoid

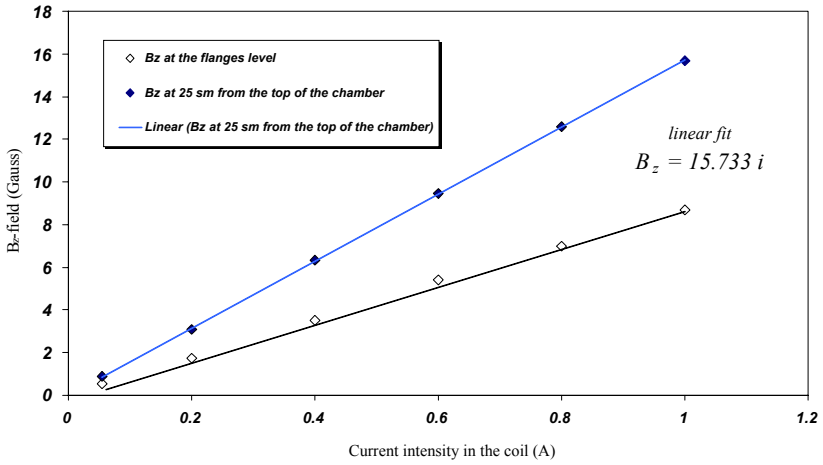

Figure 6-2: *Magnetic field versus the current intensity; upper curve as measured at 25 cm from the top of the chamber, lower curve as measured near the flanges.*

diameter is 5:1, which is a good approximation for an infinite solenoid. The magnetic flux density has been measured in these regions as B_z=15.7 Gauss in good agreement with the expected value of 16.7 Gauss. Fig. 6-2 shows the measured field B_z as a function of the current intensity in the solenoid, at fixed positions in the chamber.

Experimental results: multipacting and magnetic field

Multipacting has been triggered in the chamber with the following RF pulse parameters: amplitude V_{p-p} 210 V, period 20ns, width 10ns and a bias-voltage ca. -10 V. These values corresponding to the output power limit. As shown in Fig. 6-3, increasing the magnetic flux density B_z, the multipacting current at the pick-up at first slightly increases, and then decreases to zero for $B_z \geq 4.7$ Gauss.

In the case of a slightly lower pulse amplitude of 195 Volt, the electron multiplication stops at a lower value of $B_z = 3.5$ *Gauss*.

6.2 Model

In this section I present a simple model to describe the suppression of multipacting in the multi-wire chamber by a solenoid magnetic field. In order to explain the effect of the solenoid magnetic field on multipacting, we integrate the equations of motion for a *reference* electron travelling inside the chamber in the presence of a magnetic flux density ranging from 0 to 5 Gauss.

As defined in chapter 3, the phase of the pulse is given by $\varphi(t) = \frac{2\pi t}{T}$, $t = 0$ represents the beginning of the rectangular pulse and the time at which the electron is emitted from the surface. The fractional impact time of the period was defined as

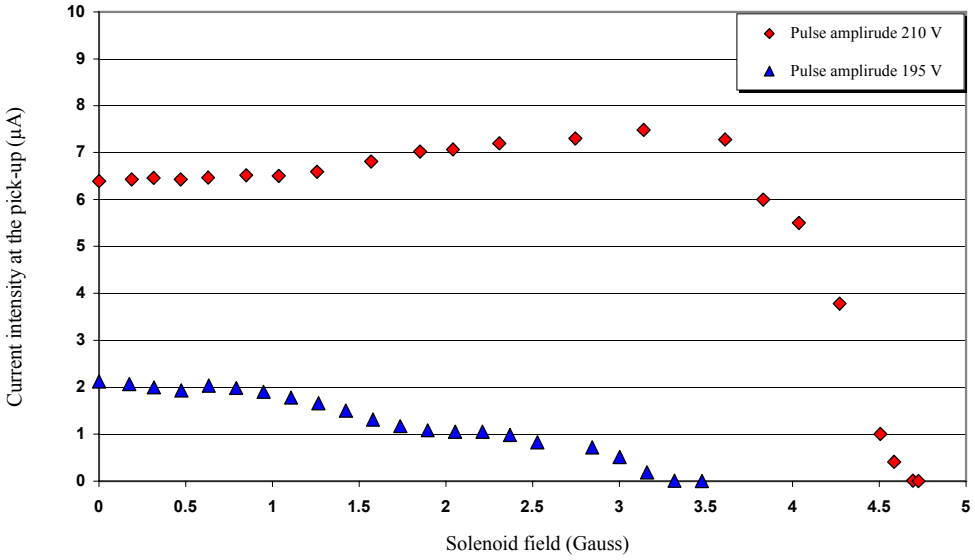

Figure 6-3: *Multipacting intensity as a function of the solenoid magnetic field; lower curve for a pulse amplitude 195 V, upper curve for the limit pulse amplitude 210 V.*

$$f = \frac{\varphi(t_{imp})}{2\pi} \tag{6.1}$$

where t_{imp} is the instant at which the electron hits the opposite side of the chamber; thus $f = 1$ represents an electron hitting the wall exactly in synchronism with the RF pulse (corresponding to the kinematic condition of Eq. 3.1).

In the calculations I consider a 5 eV energy electron (average energy of secondary electrons) emitted from the chamber surface and I integrate the equations of motion for different values of the applied solenoid magnetic field. The result in Fig. 6-5 shows the case of $B_z = 5$ Gauss, that the electron deviates substantially from its originary trajectory ($B_z = 0$).

In order to satisfy the kinematic multipacting conditions f should be ≈ 1. In Fig. 6-4 the factor f has been calculated as a function of the magnetic flux density. The factor f decreases while B_z is increased, therefore, the reference electron strikes the wall always earlier; when f is far from one the electron gets out of phase with respect to the RF pulse. An estimation of the lower limit value of f for which electron multiplication occurs was given in section 3.2.2. There it was found that multipacting should stop for f values lower than 0.9[2]. Thus, from Fig. 6-4, we would expect that $B_z \approx 3$ Gauss is sufficient to stop

[2]The estimation of $f \approx 1 \pm 0.1$ was drawn considering one 5eV *reference* electron, where a more complete model should take into account the entire energy spectrum of the secondary electrons, resulting in slightly larger windows than predicted here.

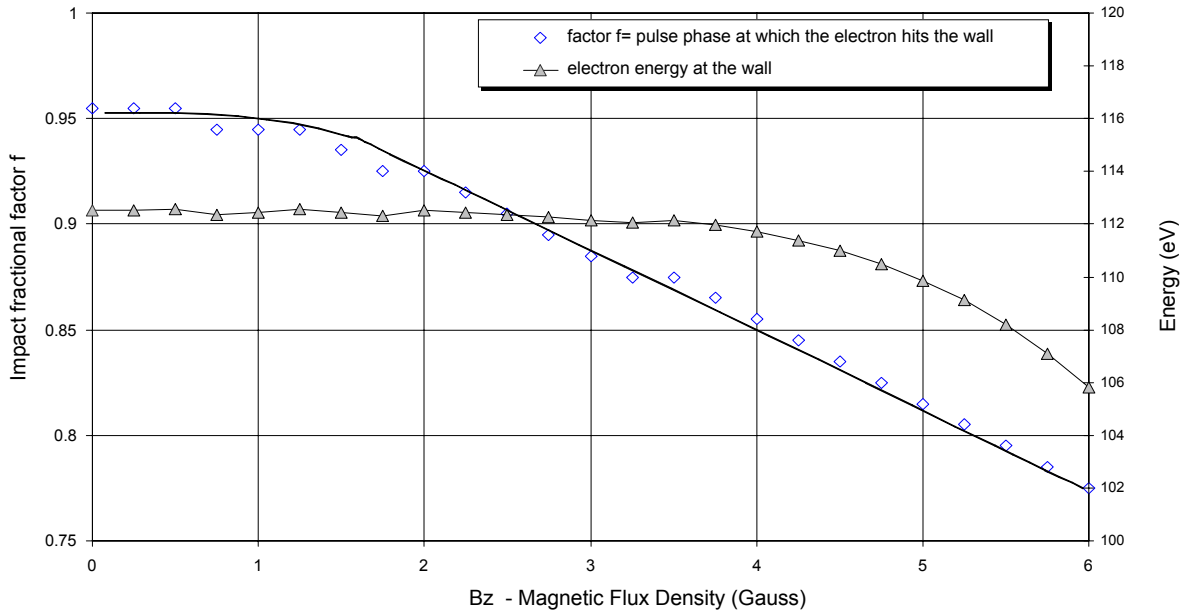

Figure 6-4: *Factor f and electron impact energy as function of the applied axial magnetic field*

multipacting instead of the measured value $B_z = 4.7$ Gauss; nevertheless, considering that the multipacting current is measured in the central part of the chamber[3], where the magnetic field is reduced by a factor of 1/3, see *right* of Fig. 6-1, the model explains quite well the experimental result.

For larger B_z the electrons are no more coupled with the pulses and the multipacting resonance should stop[4].

6.3 Solenoid magnetic field in the LHC field-free regions of the LHC

Most of the LHC circumference is occupied by high-field dipole magnets in which the electron motion is constrained to the vertical plane. In a vertical magnetic field B of 8.4 Tesla, the electron with energy $E \approx 200eV$, rotates on a circle in the x-z plane with a Larmor radius

$$r = \frac{\sqrt{2emE}}{eB} \simeq 5.6\mu m \tag{6.2}$$

[3] where the pick-up probe is located, see flanges on *left*-hand side of Fig. 6-1

[4] A more detailed calculation should evaluate the factor f averaged over RF phases of emission, and over all secondary electron emission energies.

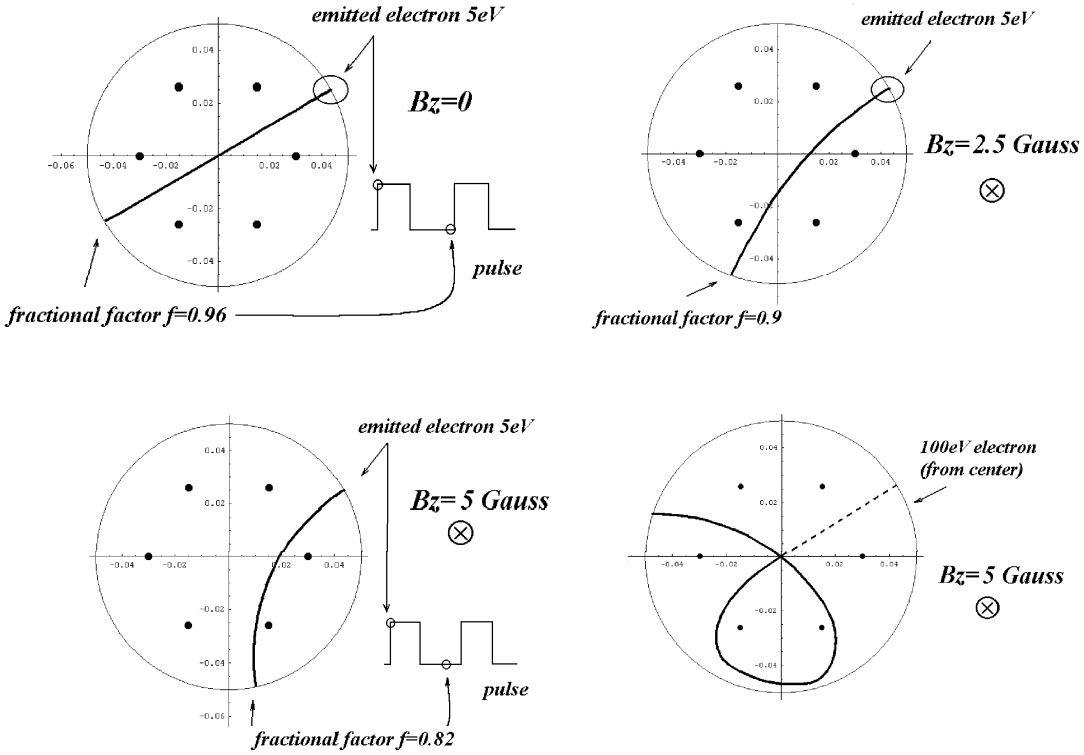

Figure 6-5: *Electron trajectories in the multi-wire chamber with solenoid magnetic field B_z=0, 2.5 and 5 Gauss, and pulse amplitude 210V.*
Top Lef*: B_z=0 Gauss, $f = 0.96$ (multipacting is present)*
Top Right*: B_z=2.5 Gauss, $f = 0.9$*
Below Left*: B_z=5 Gauss, $f = 0.82$ (multipacting is absent)*
Below Right*: 100 eV electron passing the center of the chamber when the magnetic field is on - trajectory related to 2 pulse periods; during the 1st pulse period the electron approaching the surface is decelerated and the Larmour radius decreases*

Electrons experience ~ 100 cyclotron rotations during the bunch passage; therefore they only receive a net vertical kick from the beam in the dipole magnet. Here a weak solenoid magnetic field would not affect the multipacting resonance.

Nevertheless a solenoid field could be used in the field-free regions where no dipole magnetic field is present. Electrons receive both a horizontal and a vertical kick from each passage of the bunch.

In order to estimate the magnetic field necessary to suppress multipacting in the LHC accelerator we have run a series of simulations with the LHC program code including the axial magnetic field. A magnetic flux density of 50 Gauss was shown to reduce consistently the heat load in the LHC drift field-free regions [56]. The presence of an axial magnetic field of $B_z = 50\ Gauss$, should not affect the motion of the proton beam, since $v_\perp \times B_z \simeq 0$, where $v_\perp$ is the transverse velocity of the proton.

In the following I draw some conclusions on the electron motion in the presence of a

solenoid magnetic field, in order to estimate analytically the magnetic field necessary to suppress the multipacting resonance.

As it was discussed in section 1.2, the maximum photoelectron energy gain by the first proton bunch is given by

$$E_{\max} = 2mc^2 r_e^2 \left(\frac{N_b}{b}\right)^2 \approx 200eV \tag{6.3}$$

However, most photoelectrons will see only a fraction of the bunch, and the average energy gain is $< E_{ph} > \approx E_{\max}/3 \approx 80eV$[5].

As the photo-electrons cross the chamber between two bunches they will hit the wall with a fractional time factor (defined by Eq. (6.1)), which depends on their energy; I will assume that the average factor f for the photoelectrons is given by

$$< f(E_{ph}) >= f(< E_{ph} >) \approx f_{ph}(E_{\max}/3) \tag{6.4}$$

the average factor f for the photo-electrons is then $f_{ph}(80eV)$. The photo-electrons cross the LHC vacuum chamber and hit the opposite side of the beam pipe producing secondary electrons with 5eV average energy. The secondary electrons are driven back to the surface by the magnetic field, and produce other electrons according to the secondary electron yield $\delta(E)$; since $\delta < 1$ for low energy electrons, the initial number of secondary electrons is strongly reduced.

Similarly, we can define an average factor f for the first generation of secondary electrons which move along the beam pipe, assuming $< f(E_{se}) > \approx f_{se}(5eV)$.

Multipacting is substantially reduced if

$$f_{ph}(80eV) + f_{se}(5eV) \leq 1 \tag{6.5}$$

or $t'_{ph} + t'_{se} \leq T$, where t'_{ph} and t'_{se} represent the time of flight of the *reference* photoelectron and of the secondary electron respectively across the beam pipe, and T the bunch period.

I will consider the simplest case of electrons emitted parallel to the surface normal, and a round beam pipe with R=2.2cm. Integrating the equations of motion for the *reference* $80eV$ photoelectron and for the *reference* $5eV$ secondary electron, for nominal proton beam parameters (7TeV) and without solenoidal magnetic field, we have $f_{ph} + f_{se} > 1$. In this case the *reference* secondary electron, is still in the chamber before the passage of the subsequent proton bunch and will take part in multipacting[6]. L*eft*-hand side of Fig. 6-6 shows the fractional time factor $f_{ph} + f_{se}$ as a function of the applied axial magnetic field.

[5] In the kick approximation, the momentum gained by a photoelectron emitted at a scaled position $\bar{z}$ will be $p = \Delta p_{\max} \int_{-z_{tail}}^{\bar{z}} \lambda(z')\, dz'$,where $\lambda(z)$ is the longitudinal bunch distribution,and z_{tail} refers to the tail of the bunch. Since the number of photoelectrons produced at a scaled longitudinal position $\bar{z}$ is proportional to $\lambda(z)$, the momentum gained by the photoelectrons will be uniformly distributed between 0 and $\Delta p_{\max}$, consequently the average energy gain is $E_{\max}/3$ [57].

[6] Nevertheless, in this case, the secondary electrons with an energy larger than ca. 9eV are considered lost, because they hit the wall before the passage of the next bunch and do not contribute to multipacting.

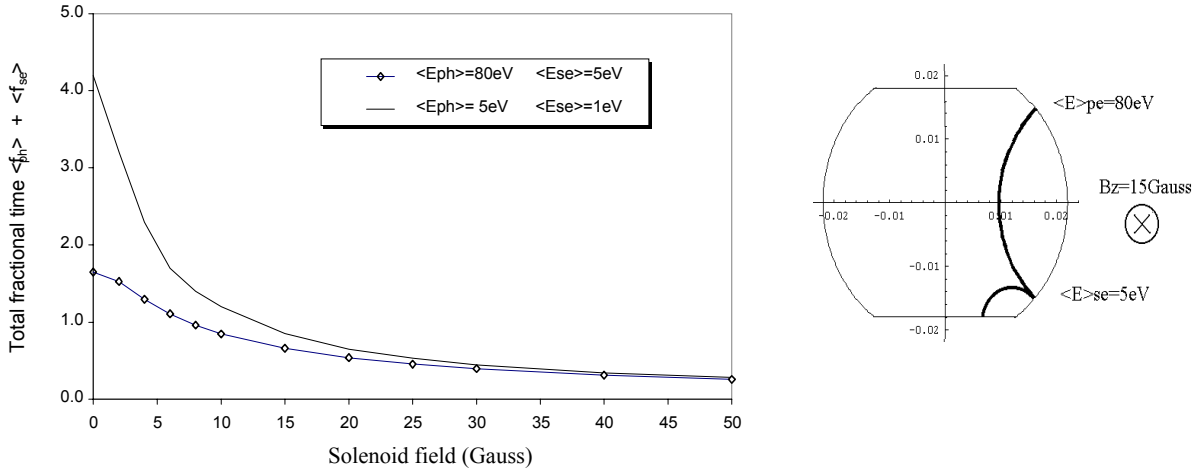

Figure 6-6: Left: *Factor f as a function of the solenoid field, $f < 1$ for $B_z \approx 15$ Gauss* Right*: Warm straight LHC section, secondary electrons are bent back to the surface before the passage of the subsequent proton bunch*

The lower curve corresponds to the case $< E_{ph} >= 80eV$ and $< E_{se} >= 5eV$, while for the top curve (worst case) I assume an average energy $< E_{ph} >= 5eV$ for the photoelectrons, and an average energy $< E_{se} >= 1eV$ for the emitted secondary electrons. A fractional time factor larger than 1 corresponds to a multiple number of periods T that would be necessary to let the secondary electron strike the surface.

For $B_z \approx 15$ *Gauss*, we have

$$f_{ph}(5eV) + f_{se}(1eV) \ < 1 \tag{6.6}$$

In this case, all the secondary electrons hit the wall and are lost before the arrival of the following proton bunch. *Right*-hand side of Fig. 6-6 shows trajectories of the photoelectron and secondary electron reference particles for $B_z = 15$ *Gauss*.

Reduction of the surface heat load due to the solenoid magnetic field

The solenoid field has a twofold advantage:

- drive the secondary electrons back to the surface before the passage of the subsequent bunch
- confine the secondary electrons in a region near the surface

As discussed above, the secondary electrons are driven back to the surface by the magnetic field, and produce other electrons according to the secondary electron yield $\delta(E)$. The solenoid field turns the new generations of electrons back, which decreases in magnitude, depending on δ and on the magnetic field intensity, before the next bunch passage.

During the subsequent bunch passage the secondary electrons are confined in a region near the surface and experience a maximum energy gain $E_{max} \approx 200eV$, with an average energy of ca. $80eV$. As a consequence the surface heat load is consistently reduced by:

- a reduction in the number of secondary electrons, by one or several orders of magnitude
- almost one order of magnitude less for the average energy gain of the secondary electrons, ca. $80eV$ compared to $650eV$ for a uniform distribution (see Chapter 1) of the electrons in the chamber

In the positron ring of the PEP II B-factory, beyond a current threshold a pressure rise has been observed. The pressure rise in the accelerator, could be reduced by a factor 2 (but not suppressed), by a solenoid magnetic field of 25-50 Gauss. In case of multipacting is confirmed for PEP II, the observed pressure rise may be due to the primary photoelectrons and to the secondary electrons, which are reduced in number but not completely eliminated by the magnetic field. Nevertheless, in the PEP II case according to the previous estimations one would expect a larger reduction of the pressure rise than observed.

Chapter 7

100 MHz Coaxial resonant cavity

Introduction

The aim of developing a resonant cavity was to test multipacting with a higher electric field with respect to the TW multi-wire chamber; since the electric field can be much higher in a resonant cavity for the same available RF power. The energy is stored in the resonant cavity while in the multi-wire chamber, when operating in the TW mode, the power is adsorbed by the line loads terminating it.

Higher electron energies give the possibility to test the conditioning methods described in the previous Chapter in more detail. In particular, since we expect a lower critical SEY with respect to the multi-wire chamber, it will be possible to study the multipacting conditioning for larger multipacting electron doses. The effect of the solenoid magnetic field and the freon plasma conditioning will be also tested in the resonant cavity.

The cavity has been designed and built to operate at a resonance frequency of 100MHz, in the $\lambda/2$ configuration. The detailed description of the resonant cavity is given in Chapter 2. After the optimization of the cavity performances, the first measurements have been completed and the presence of the first level of multipacting has been verified.

The experimental set-up is shown in section 7.1. The optimizations of the cavity parameters and the measurements of the Q quality factor are given in section 7.1.1. The measurement of the first multipacting level is shown in section 7.1.3.

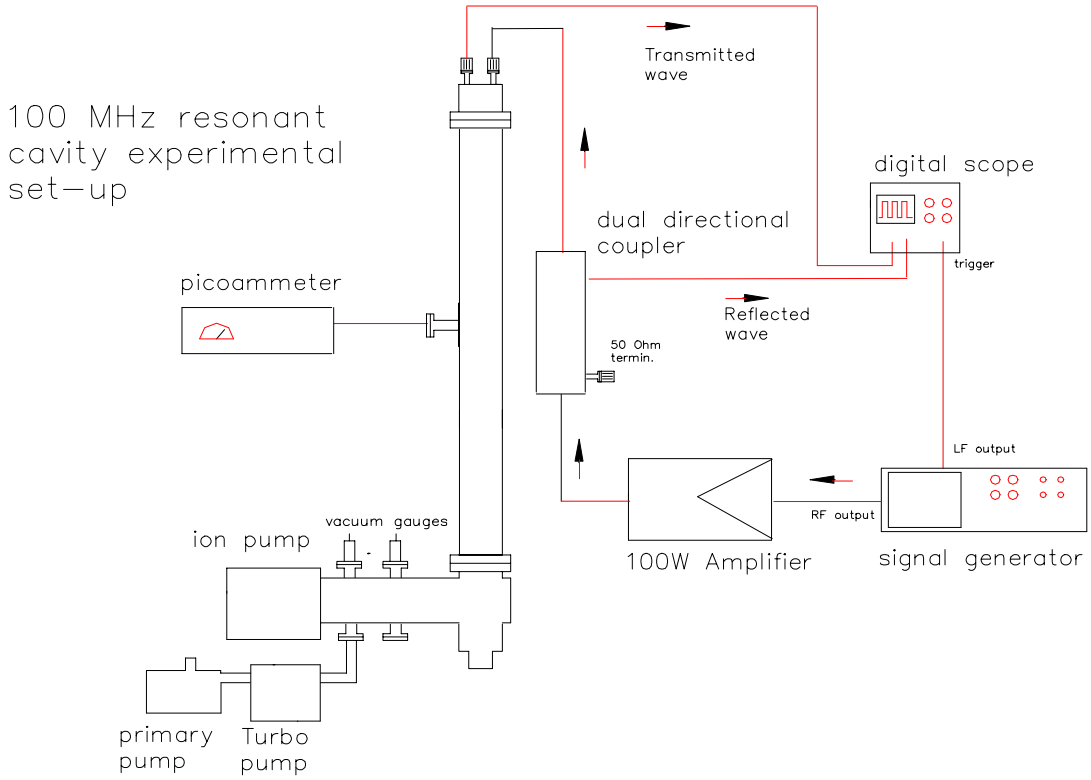

Figure 7-1: *100MHz resonant cavity experimental set-up*

7.1 Experimental set-up general overview

The resonant cavity is part of a coaxial waveguide. Two coaxial conductors with $100mm$ and $32mm$ diameters are delimited at the top and bottom by two metallic planes perpendicular to the cavity axis. The experimental set-up is shown in Fig. 7-1.

The 100 MHz signal produced by a radiofrequency generator is sent, via an amplifier and a dual directional coupler, to the coupling loop, in order to excite the magnetic field inside the resonant cavity. Part of the signal is reflected back and sent, via the directional coupler, to the oscilloscope to be analyzed. The second loop is arranged to take a fraction of the radiofrequency signal inside the cavity. The transmitted signal is sent to the oscilloscope to be measured.

The coupling loops are mounted on two manual drives, which are used to adjust the active area of the loop, intercepting the field lines.

A pick-up probe has been arranged at the half height of the cavity to measure the multipacting current intensity. The parameters of the cavity have been optimized to obtain the maximal multipacting current intensity. The cavity dimensions determine the presence of multipacting. Before the construction of the resonant cavity, I have run the LHC multipacting simulation program, for a coaxial cavity configuration, to determine the geometry which gives multipacting with the maximum current intensity. The simulation

provides the ratio between the outer and the inner conductor radius of 3:1.

7.1.1 Coupling loop calculation

The inductive coupling is obtained by arranging the loop inside the cavity, intercepting the magnetic field lines, at the top of the cavity where the magnetic field is high.

The objective of the calculation was to estimate the area of the coupling loop. In order to calculate the impedance of the loop I assume, as a first approximation, a circular geometry. In addition, I assumed a normalized current flowing in the conductor I_c. The magnetic field at a radial position r in the chamber is given by

$$H_0 = \frac{I_c}{2\pi r}\cos(kz)\mathbf{e}_\theta$$

with z the axial direction. The magnitude of the voltage induced in the loop by the cavity is

$$V = \omega\mu_0 S\bar{H}$$

where S is the area of the coupling loop, ω the resonance frequency and $\bar{H}$ the average magnetic field intercepting the coupling loop.

The power in the is

$$P_{ext} = \frac{1}{2}I_s^2 Z_0$$

where the current I_s is given by

$$I_s = \frac{V}{\sqrt{Z_0^2+\omega^2 L^2}}$$

L is the self-inductance for a round loop with radius r', $L = \frac{\mu_0 S}{2\pi r'}$, and $Z_0 = 50\Omega$.

Since on a perfectly conducting wall the amplitude j of the current density must be equal to the amplitude of the magnetic field $j = n \times H$, where the field H is assumed to be purely tangential $H = H_t$. The power dissipated on the walls and required to maintain the level of excitation follow from the integration over the surface S of the cavity

$$P_d = \frac{R_s}{2}\int_S H^2 ds$$

where R_s is the surface resistivity of the cavity surface, and the integral is taken over the whole cavity surface. The dissipated power has to be restored by the power supplied by the coupling loop, and from this condition I calculate an area of the loop $S = 501mm^2$, in order to have[1] $P_d = P_{ext}$.

[1] r$' = 0.002m$, and with the internal conductor silver-coated. The dissipated power on the external conductor, on the internal conductor and on the two delimiting flanges expressed in percentage are ca. 62%-29%-9% respectively.

7.1.2 Measurement of the quality factor Q

With an external excitation $Ce^{i\omega t}$ the differential equation for an oscillating electric field with damping factor p is given by

$\frac{d^2E}{dt^2} + p\frac{dE}{dt} + \omega_0^2 E = Ce^{i\omega t}$.

Assuming an external frequency close to the natural frequency $\omega \sim \omega_0$, the substitution of the trial solution $E = Ae^{i\omega t}$ gives the stored energy proportional to the square of the amplitude of the field

$W \propto \mid A \mid^2 = \frac{C^2/4\omega_0^2}{\Delta\omega^2 + \frac{\omega_0^2}{4Q^2}} \propto \frac{1}{\Delta\omega^2 + \left(\frac{\omega_0}{2Q}\right)^2}$.

The quality factor of the resonator may be characterised by the narrowness of its resonance. Let $\Delta\omega_H$ be the full width at half height of the $\mid A \mid^2$ versus the ω curve, stored energy versus excitation frequency then for $\omega \sim \omega_0 \pm \Delta\omega_H/2$ the amplitude A has decreased to $A/\sqrt{2}$ and the stored energy has reduced by 1/2. Thus, $\Delta\omega_H = \frac{\omega_0}{Q}$ or

$Q = \frac{\omega_0}{\Delta\omega_H} = \frac{f}{\Delta f_H}$

Similarly from the same differential equation the phase shift between the two amplitudes A and C is given by

$\tan\varphi = \frac{\omega\omega_0/Q}{\omega^2 - \omega_0^2}$

if the solution for ω is evaluated with a phase shift of $\varphi = \pm\pi/4$ then $\Delta\omega = \pm\frac{\omega_0}{2Q}$. By comparison it can be seen that $\Delta\omega$ is half of $\Delta\omega_H$ and that the phase shift $\varphi = \pm\pi/4$ corresponds to the half height of the curve.

There are several methods which can be used to measure Q.

- by the decay time of the stored energy, as seen in section 2.2.2
- by the measurement of $\Delta\omega$ when the stored energy is halved, which correspond to a signal drop of -3 dB, alternatively $\Delta\omega_H$ can be found by detecting the phase shift of $\Delta\varphi = \pm 45°$

In the last case the loss should not be too high, Q not too small and the distance of the neighbouring modes much greater than $\Delta\omega_H$.

So far no external losses have been considered. The Q value was given by $Q = \frac{\omega_0 W}{P_p}$ in section 2.2.2, where P_p represents the losses in the cavity. Therefore the cavity has to be loosely coupled to the transmitter, otherwise the losses P_{ext} in the transmission line and transmitter will change the result. The Q of the external system is called $Q_{ext} = \frac{\omega_0 W}{P_{ext}}$, the loaded Q of the system is then $Q_L = \frac{\omega_0 W}{P_p + P_{ext}}$ which leads to

$\frac{1}{Q_L} = \frac{1}{Q} + \frac{1}{Q_{ext}}$

the so called coupling factor $\beta = \frac{Q}{Q_{ext}} = \frac{P_{ext}}{P_p}$ is related to the reflection coefficient at resonance by

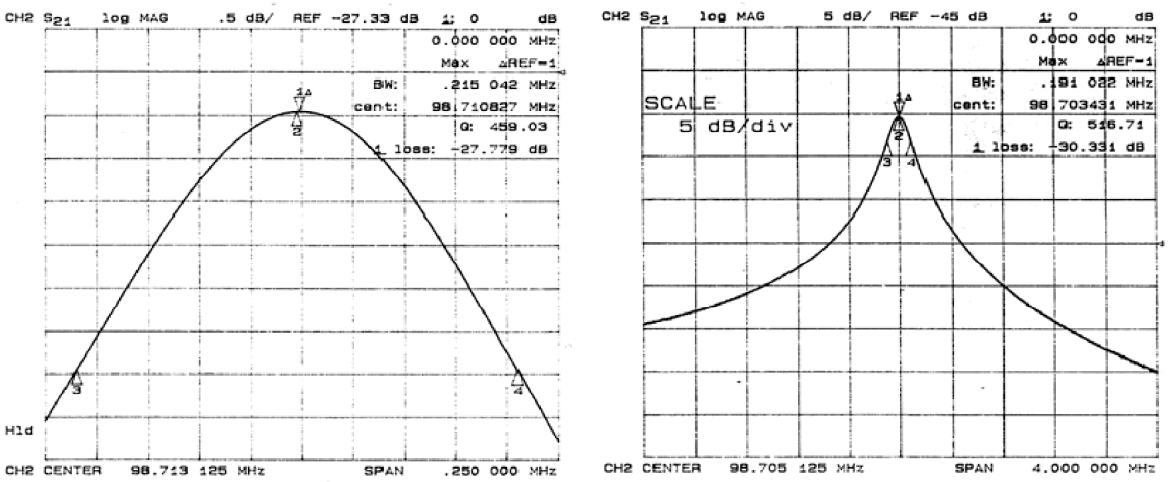

Figure 7-2: *Resonance frequency 98.7 MHz and quality factor $Q=\omega/\Delta\omega$*

$$| \rho | = \frac{|1-1/\beta|}{1+1/\beta}$$

For $\beta = 1$, the so called critical coupling all power from the transmission line goes to the resonator and no reflection occurs. In this case $P_{ext} = P_p$, $\rho = 0$ and $Q_L = Q/2$.

For $\beta \ll 1$, weak coupling, and $\beta \gg 1$, strong coupling all the power will be reflected. The coupling is adjusted by changing the area of the loop by the manual drive.

I have measured the resonance frequency and the quality factor in the cavity, as shown in Fig. 7-2.

The resonance frequency is $\nu = 98.7MHz$ and the loaded quality factor $Q_L \approx 500$, thus assuming $\beta \approx 1$ the quality factor is $Q \approx 1000$.

7.1.3 Multipacting in the resonant cavity

Multipacting occurs for defined electric field amplitudes, known as multipacting *levels*, when the secondary electron yield is greater than 1, e. g. when the electron energy is comprised between the energy E_1 and E_2 of Fig. 3-4. The multipacting levels which are related to electron energy near E_2 present a longer conditioning time than the levels which are related to E_1. In the resonant cavities, the quality factor Q as a function of the electric field shows an abrupt decrease corresponding to the multipacting levels.

An increase of the input power is adsorbed by the multipacting electrons which prevent the increase of the electric field amplitude in the chamber. In this way the multipacting process contributes to keep stable conditions. Nevertheless there is a limit in the power that the multipacting electrons can absorb for each level; if the limit is overcome the electric field amplitude increases, and the resonance condition is no more fulfilled.

The resonant frequency and the coupling are adjusted at low power to minimize the power reflected from the cavity. Increasing the input power, the transmitted signal increases until the first multipacting *level* is reached. This condition is characterized by a

distortion of the transmitted and reflected signals. A fast pressure increase occurs and a current is recorded at the pick-up.

Multipacting is maintained until the level is overcome, corresponding to a fast increase of the transmitted signal, and a decrease of the reflected signal. The overcome of one multipacting *barrier* does not assure that the conditioning is complete. Sometimes by reducing the forward power it is possible to reproduce again multipacting. When multipacting no longer occurs, it is possible to start the conditioning of the next multipacting level corresponding to higher electric field.

Measurement of the first multipacting level A consequence of multipacting is the decreasing of the coupling β. In practice it is preferable to obtain $\beta \gtrsim 1$ in order to get $\beta \approx 1$ ($P_{ext} = P_p$) during multipacting[2]. As the coupling β depends on the area of the loop intercepting the magnetic field lines, a larger area than that corresponding to $\beta = 1$ is necessary.

During the experiment three e.m. signals are measured: the forward, the reflected and the transmitted signal. It is useful to modulate the amplitude of the $100MHz$ forward signal with a low frequency sinusoidal wave. I have set the modulating signal to $0.1Hz$ and I have measured the first level of multipacting in the $100MHz$ resonant cavity as shown in Fig. 7-3.

Since the multipacting electrons absorb nearly all the power in the cavity, the resulting transmitted signal tends to be reduced when multipacting took place. In contrast, the reflected signal increases during multipacting, since the coupling between the loop and the cavity is changed. Finally the pressure abruptly increased to more than $10^{-5}mbar$, and a current signal has been observed on at the pick-up probe.

[2] a series of loops with different size have been prepared to select the most favorable for multipacting

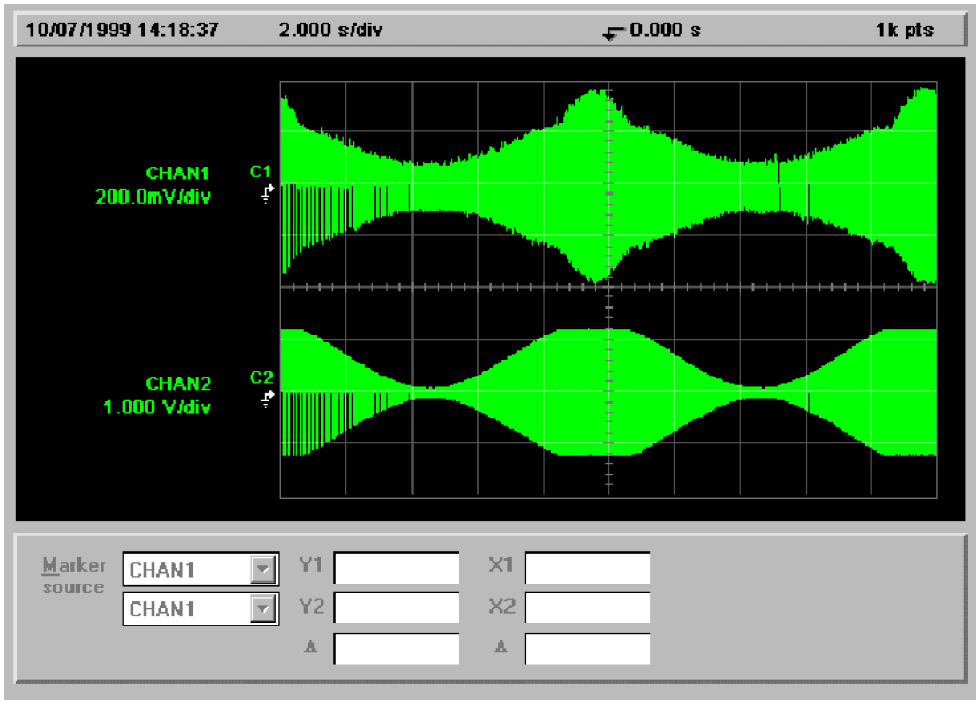

Figure 7-3: *Reflected (top) and Transmitted (lower) signals for a forward signal with a low frequency amplitude modulation 0.1Hz. The transmitted signal becomes constant when multipacting occurs. In contrast the reflected signal increases during multipacting, since the coupling between the loop and the cavity changes.*

Part IV

Conclusions

Electron multipacting phenomenon has been studied previously at CERN with two computer simulation codes which were used for estimating the heat load in the LHC beam screen: one code has been developed at LBL [12] and one at CERN [13][14]. The simulations have shown that depending on the photo-electron yield, the secondary emission yield and the reflectivity of the beam screen material, the heat load may vary from less than 0.1 Watt/meter to more than 15 Watt/meter. The cryogenic system cannot tolerate a total heat load exceeding 0.5 Watt/meter. The cryogenic budget for the heat load induced by multipacting is only 0.2 Watt/meter. It is, therefore, fundamental to study the phenomenon in order to determine the most effective way to reduce these detrimental effects for the LHC accelerator.

In this thesis the conditions for multipacting and the LHC multipacting model are presented. Moreover, some of the important parameters for multipacting in the LHC, such as the energy gain during the passage of a proton bunch, the threshold proton intensity necessary for multipacting, and the concept of a critical secondary electron yield are discussed.

A travelling-wave (TW) multi-wire chamber and a $100MHz$ resonant cavity have been built to study and in particular to reproduce multipacting using a radiofrequency pulse to simulate the effect of the proton beam on the electrons. The aim of the study has been to determine the influence on the multipacting of the parameters, such as the RF amplitude, pulse period and pulse width (simulating to the beam parameters), vacuum chamber materials, surface conditioning, treatment, etc. Furthermore, solutions to reduce multipacting in LHC have been investigated.

The systems were fitted with an electron pick-up which could measure the number of incident electrons on the wall, and the production of secondary electrons. The advantage of the travelling wave system with respect to the resonant system is that the secondary electrons drift takes place in the period between two pulses and thus simulates more closely the real phenomenon in the LHC accelerator. Nevertheless, the resonant cavity can store higher electric fields, giving the possibility to study the multipacting phenomenon in more detail. I present the electric and magnetic field configurations of the experimental systems, as required for the computer simulations.

The system reveals very clear evidence of a multipacting behaviour which is sensitive to the pulse amplitude (related to the bunch intensity in LHC), to the repetition rate (bunch spacing) and to the pulse width (bunch length). I have determined experimentally the multipacting dependence on the RF pulse parameters in the multi-wire chamber setup. To validate the computer code developed at CERN to simulate multipacting, this program has been adapted to the travelling-wave experimental set-up, and I have performed new simulations for the multi-wire chamber geometry. Moreover, I have studied a model to explain the multipacting dependence on the RF pulse parameters and on the minimum RF amplitude for multipacting. The results obtained both with the simulations and with the model show a qualitative agreement with the experimental results.

In order to verify the correctness of the average electron energy estimation for LHC, as given by the simulations: I have built an energy spectrum analyzer, which was used to measure the energy distribution of the electrons hitting the surface of the multi-wire chamber during multipacting. Furthermore, an electron gun was built to test the energy

spectrum analyzer. The simulations are in good agreement with the experimental data for the energy distribution, giving confidence in the LHC multipacting code.

The critical secondary yield δ_{crit}, is a crucial parameter for the LHC. A substantial effort is aimed at finding ways how to reduce the effective SEY below this value. The electron cloud decreases if the secondary electron yield is below a critical value, while it increases if the SEY is above the critical value. In the multi-wire chamber the same effect occurs. I have estimated the δ_{crit} for the experimental system both with calculations and by computer simulations. In particular, the estimated critical secondary yield is δ_{crit}=1.7 when the highest experimental pulse power is taken into account in the simulation. Thus, according to the simulations, if the effective $\delta_{\max}$ is lower than 1.7 the resonance of multipacting can no longer be initiated.

Beam scrubbing, by means of the energetic multipacting electrons, is one of the most effective ways for *in-situ* cleaning of the beam screen surface in LHC.

In the multi-wire chamber, I have determined how the multipacting intensity decreases as a function of the electron dose, in order to estimate the electron dose necessary to reduce the secondary yield below the critical value for LHC. Considering nominal LHC beam parameters ($7TeV$-$0.54A$) and the reduction of the secondary yield measured in the travelling-wave chamber, I estimate for the LHC dipole sections a scrubbing time of ~1100 hours. This estimation is the worst case, when considering the effect of photoelectrons only. If we take into account also the contribution of the multipacting electrons, the scrubbing time is substantially reduced to 90 hours. Nevertheless, the pressure in the beam pipe can increase due to electron stimulated desorption (as in the SPS accelerator at CERN, where multipacting has very recently been observed with LHC-type proton beams), causing, ultimately, the loss of the proton beam. I have estimated the reduction rate of the secondary electron yield for the LHC during the commissioning period in the first year of operation, when LHC operates with one tenth to one fifth of the nominal beam current. It turns out that the scrubbing time may exceed the commissioning period, if one considers the secondary yield reduction rate measured in the travelling-wave chamber.

It is observed that following a high electron dose, the multipacting threshold could again decrease while the system is left in stand-by under vacuum. A re-conditioning period would then be necessary. A severe problem may be the relatively fast surface recontamination, due to venting of the system to atmospheric pressure.

Even if the variation of the SEY during multipacting or electron bombardment is a known effect, the observed decrease of the secondary electron yield to a value lower than that for the pure material, is not understood. Motivated by the fact that beam scrubbing is one of the most promising ways to *in-situ* condition the LHC beam screen, an Auger electron spectroscopy analysis of samples exposed to different multipacting electron doses was performed.

From my studies I can conclude that the secondary electron yield decreases during multipacting conditioning, or electron-beam bombardment, due to two different simultaneous surface effects:

- the removal from the surface of contaminants causing a high secondary yield
- the build-up of a carbon layer on the surface of the material, which has a secondary

yield lower than 1

The relative contribution of the two effects is difficult to estimate.

Finally, since I was interested in measuring directly the reduction of the secondary electron yield during multipacting conditioning, I have built a system to measure the SEY in the multi-wire chamber.

In spite of the *in-situ* beam-scrubbing scenario for LHC, other possible remedies have been studied in order to suppress multipacting in the most effective way and as permanently as possible. After bake-out of the chamber the multipacting threshold is increased consistently and the scrubbing time reduced by about one order of magnitude.

A promising way to eliminate multipacting from the system was a novel plasma RF discharge treatment using Freon11 (CCl_3F), which I have tested with the multi-wire chamber on stainless steel and on a copper surface. The freon plasma RF discharge treatment was found to be particularly effective in rapidly suppressing multipacting in the multi-wire chamber. In addition, I studied the recontamination time after the freon plasma treatment and after venting the system to atm. pressure with air for a long period of time, with promising results.

Auger spectroscopy analysis shows that on stainless steel and copper samples exposed to the freon plasma two different effects occur, both very effective at reducing the secondary electron yield. I may conclude from the Auger spectroscopy analysis, that the freon plasma conditioning, on the copper sample surfaces, results in a decrease of the secondary electron yield due to the removal of the surface contaminants by the freon radicals, and to a large concentration of chlorine; a real *cleaning* effect occurs on the copper surface. The radicals of freon, containing the reactive fluorine and chlorine, are produced by cracking due to the multipacting electrons. On the stainless steel samples a large carbon deposition occurs, which has a low secondary yield. Recent tests [35] have shown that the freon treatment does not deteriorate (and may even improve) the performance of a superconducting cavity. The effect of photo-desorption on a surface exposed to the freon plasma needs still to be investigated.

In order to study multipacting with different LHC surface materials, I have used rolled sheets100mm diam., 1.4m long, made of OFHC copper, TiZrV-coated (LHC beam pipe materials) and aluminium, which were fitted into the multi-wire chamber.

The freon plasma RF discharge treatment, was found to be very effective at quickly eliminating multipacting also on the copper surface.

With the TiZrV (NEG) coated surface, I have observed the complete disappearance of multipacting, after baking the system at 180°C and the consequent NEG activation. In addition, the recontamination, due to venting the system to atm. pressure for a long period of time, was found to be very low.

A complete suppression of the electron multiplication can be achieved with an axial solenoid magnetic field of only few Gauss in the experimental multi-wire chamber. From simulations [56] the heat load at the LHC beam pipe is significantly reduced in the straight sections in the presence of less than 50 $Gauss$ axial magnetic field. From an analytical calculation I could demonstrate that by applying a solenoid field of $B_z = 15$ $Gauss$ the secondary electrons are reduced by some order of magnitude before the passage of

the subsequent bunch. A solenoid magnetic field is, therefore, a promising method to suppress multipacting in the LHC straight sections, while it would be ineffective in the dipole magnets where any electron motion is dominated by the strong vertical field of 8.4 T.

A 100 MHz resonant cavity was built to study multipacting with higher electric field than in the travelling-wave chamber. I took part in the assembling, optimization of the performance and in the start-up of this system. The preliminary tests, during which multipacting was observed in the resonant cavity have been presented.

More recently multipacting has been unambiguously observed in the SPS with an LHC-type proton beam [5] during dedicated *machine development* (*MD)* sessions for LHC. I took part in the measurements, where above a threshold beam intensity a pressure rise by more than a factor 50 has been observed. Next, I measured the current of the electrons travelling across the vacuum chamber during multipacting, by means of a pick-up probe placed in the accelerator. The current at the pick-up was recorded, while the pressure increased strongly in the accelerator vacuum chamber. Moreover, I have performed preliminary measurements of beam loss caused by the pressure rise, by means of scintillator counters placed near the vacuum pipe, along the circumference of the accelerator.

An extensive program is underway at CERN for the next *MD* period in the SPS in order to evaluate the possible remedies, like the freon plasma treatment, the activation of the TiZrV coating and the solenoid magnetic field, which were tested by the recent studies, and to determine the most effective way to avoid the detrimental effect of the electron-cloud in the LHC accelerator.

Part V

Bibliography

Bibliography

[1] P. Farnsworth, J. Franklin Inst., 2, 411-16,1934, and Z. Phys., **129**, 491-6,1951.

[2] O. Gröbner, 10th Int. Conf. on High Energy Accelerators, protvino, July (1977)

[3] O.S. Bruning "*Simulations for the Beam-Induced Electron Cloud in the LHC beam screen with Magnetic Field and Image Charges*", LHC project Report 158, 7 November 1997

[4] M.A. Furman, "*The Electron-Cloud Effect in the Arcs of the LHC*", CERN LHC Project Report 180 (May 1998), also published as LBNL-41482/CBP Note 247.

[5] G. Arduini, K. Cornelis, J.M. Jimenez, G. Moulard, M. Pivi, K. Weiss "*Electron cloud: SPS observations with LHC type beams*", will be presented at next: Workshop on LEP-SPS Performance - 17-21 January 2000, Chamonix, France.

[6] I.R.Collins, O.Gröbner, N.Hilleret, J.M. Jimenez and M.Pivi, "Electron cloud potential remedies for the vacuum system of the SPS", will be presented at next: Workshop on LEP-SPS Performance - 17-21 January 2000, Chamonix, France

[7] O. Gröbner "*Bunch-Induced Multipacting*", PAC97, Vancouver,BC, May 12-16, 1997

[8] J.S. Berg, "Energy Gain in an Electron Cloud during the passage of a bunch", LHC project note 97, 1 July 1997*of the SPS*", will be presented at next: Workshop on LEP-SPS Performance - 17-21 January 2000, Chamonix, France.

[9] S. Ramo, J. Whinnery, T. Van Duzer, "*Fields and waves in communication electronics*", J. Wiley and Sons, 1984

[10] E. Sommersalo, P. Yla-Oijala, D. Proch and J. Sarvas "Computational methods for analyzing electron multipacting in RF structures, Particle Accelerator, Vol. 59, pp. 107-141.

[11] *Cern accelerator School RF engineering for Particle Accelerator,* Yellow book, CERN 92-03 June 1992

[12] M.A. Furman, *"The Electron-Cloud Effect in the Arcs of the LHC"*, CERN LHC Project Report 180 (May 1998), also published as LBNL-41482/CBP Note 247.

[13] F. Zimmermann, "*A simulation Study of Electron-Cloud instability and Beam-Induced Multipactoring in the LHC",* LHC Project Report 95 (1997)

[14] O. Bruning "*Simulations for the Beam-Induced Electron Cloud in the LHC beam screen with Magnetic Field and Image Charges*", LHC project Report 158, 7 November 1997

[15] H. Seiler, "Secondary electron emission in the scanning electron microscopy", Phys. 54 (11) (1983)

[16] N. Hilleret Cern, private communication, October 1998

[17] J-M. Laurent, CERN, notes about "*Bunch induced multipactoring tests for LHC*"

[18] E. Mercier, N. Hilleret, B.Henrist, *Mésure de la distribution en energie des electrons secondaries pour le LHC*, Cern, Rapport de stage, Mars-Juin 1999

[19] O. Brüning, F. Caspers, I.R. Collins, O. Gröbner, B. Henrist, N. Hilleret, J.-M. Laurent, M. Morvillo, M. Pivi, F. Ruggiero and X. Zhang "*Electron Cloud and Beam Scrubbing in the LHC*", LHC-Project-Report-290, presented at the Particle Accelerator Conference (PAC'99), New York, 29 Mar - 2 Apr 1999.

[20] G.V. Stupakov, "*Photoelectrons and Multipacting in the LHC: Electron-Cloud build-up*", LHC Project Report 141, October 1997

[21] F. Zimmermann, "Electron-cloud Simulations for the Straight Sections", LHC Project Note 201, September 1999

[22] Ertl and Kuppers, *Low energy electrons and chemistry*

[23] D. Briggs and M.P. Seah, *Pratical Surface Analysis,* Second Edition pg. 75-78, John Wiley and Sons Ltd. (1990)

[24] *Methods of experimental physics,* Vol. **22, 4** pg 218-223, Academic Press Inc. (1985)

[25] J.B. Jeanneret, "*Photoemission in LHC - A simple model*", CERN SL/Note 97-48 (AP)

[26] I.R. Collins, A.G. MAthewson and R. Cimino, " *VUV Synchrotron Radiation Photoemission Investigation of Proposed Materials for the Vacuum Chambers of the Large Hadron Collider"*, CERN Vacuum Technical Note 97-24, Presented at ECASIA'97, Göteborg, Sweden,16-20 June 1997.

[27] N.J. Félici, *Introduction a l'optique corpusculaire,* Gauthier-Villars and C. 1965

[28] N. Tolk, M. Traum, J. Tully and T. Madey, *Desorption Induced by Electronic Transitions*, DIET I. Springer Verlag, Berlin 1983.

[29] R. Calder, G. Dominichini, and N. Hilleret, "*Influence of various surface treatments on the secondary electron yield of Niobium",* Nucl. Instr. and Meth. in Phys. Res. B13 (1986) 631-636, North-Holland, Amsterdam

[30] M. Lavarec, P. Bocquet, and A. Septier "*Variation of the secondary emission coefficient of real surfaces under the effect of primary electronic bombardment*" Acc. of Sci. Paris, V. 288 p.77-80 (1979) series B

[31] H.J.Hopman, J. Verhoeven, J.J. Scholtz, R. Fastenau, "*Time variation of secondary electron emission during electron bombardment of rutile*", Applied Surf. Sci., 111, (1997), 270-275

[32] C. Scheuerlein, "*The influence of an Air Exposure on the Secondary Electron Yield of Copper",* Diplomarbeit at CERN, Berlin (1997)

[33] B. Henrist, N. Hilleret, C. Scheuerlein, "*The Secondary Electron yield of the Non Evaporable Getter Alloys TiZr and TiZrV*", CERN Vacuum Technical Note 98-08, Apr. 1998

[34] J.W. Noe', "Freon Plasma surface treatment for multipactoring", Nucl. instr. and Meth., A328, 291 (1993)

[35] J.W. Noe', J. Rico and H. Uto, Nucl. instr. and Meth., A328, 285 (1993)

[36] K. Tatenuma, T. Momose, H. Ishimaru,"*Quick acquisition of clean ultrahigh vacuum by chemical process technology*", 1719, J. Vac. Sci. Tech., A 11(4), Jul/Aug 1993

[37] C. Benvenuti, G. Canil, P.Chiggiato,P.Collin, R.Cosso, J. Guerrin, S. Ilie, D. Latorre and K.S. Neil, "*Surface cleaning efficiency measurements for UHV applications",* CERN

[38] N. Hilleret, private communication, Cern, May 1999.

[39] B. Henrist, N. Hilleret, C. Scheuerlein, "*The secondary electron yield of the non evaporable getter alloys TiZr and TiZrV*", CERN, Vacuum technical Note 98-08, Apr. 1998

[40] Vladimir Rouzinov, private communication, Cern, July 1999.

[41] Jochims, H.-W.; Lohr, W.; Baumgartel, H., *Photoreactions of small organic molecules V. Absorption-, photoion- and resonance photoelectron-spectra of CF3Cl, CF2Cl2, CFCl3 in the energy range 10-25 eV*, Ber. Bunsen-Ges. Phys. Chem., 1976, 80, 130. [all data]

[42] Schenk, H.; Oertel, H.; Baumgartel, H., *Photoreactions of small organic molecules VII Photoionization studies on the ion-pair formation of the fluorochloromethanes CF2Cl2, CF3Cl, and CFCl3*, Ber. Bunsen-Ges. Phys. Chem., 1979, 83, 683. [all data]

[43] Ajello, J.M.; Huntress, W.T., Jr.; Rayermann, P., *A photoionization mass spectrometer study of CFCl3, CF2Cl2 and CF3Cl*, J. Chem. Phys., 1976, 64, 4746. [all data]

[44] Curran, R.K., *Positive and negative ion formation in CCl_3F*, J. Chem. Phys., 1961, 34, 2007. [all data]

[45] Syrvatka, B.G. Bel'ferman, A.L. Gil'burd, M.M. Moin, F.B., *Determination of the dissociation energy of the double bond in some fluorochloro-substituted ethylenes and their ions by electron bombardment*, J. Org. Chem. USSR, 1971, 7, 8, In original 9.

[46] web page⇒ http://webbook.nist.gov/chemistry/

[47] *Hanbook of Auger Electron spectroscopy*, Third edition, Φ Physical Electronics

[48] H. Bruining, *Physics and application of secondary electron emission*, London, Pergamon Press. Ltd (1954)

[49] M. Taborelli, private comunication, Cern, May 1999

[50] K.I. Shiffmann, *"Investigation of fabrication parameters for the electron beam induced deposition of contamination tips used in atomic force microscopy",* Nanotechnology **4** (1993) 163-169

[51] N. Miura, H. Ishii, J. Shirakashi, A. Yamada, M. Konagai, "*Electron-beam induced deposition of carbonaceous microstructures using scanning electron microscopy",* Appl. Surf. Sci. 113/114 (1997) 269-273

[52] H. Hiroshima and M. Komuro, "*Fabrication of conductive wires by electron-beam-induced deposition",* Nanotechnology **9** (1998) 108-112

[53] H.W.P. Koops, A. Kaya and M. Weber, "*Fabrication and characterization of platinum nanocrystalline material grown by electron-beam-induced deposition",* J. Vac. Sci. Tech. B 13(6), Nov/Dec 1995

[54] N. Hilleret, B. Henrist and M. Taborelli, private communications, Cern, Mar 1999 - Sep 1999.

[55] V. Baglin, I.R. Collins, J. Gómez-Goñi, O. Gröbner, B. Henrist, N. Hilleret, J-M. Laurent, M.Pivi - R. Cimino - V.V. Anashin, R.V. Dostovalov, N.V. Fedorov, A.A. Krasnov, O.B. Malyshev, E.E. Pyata, "*Experimental investigations of the electron cloud key parameters*", presented at the e+e- Factories'99 conference, KEK Tsukuba, Japan, 21-24 Sep. 1999.

[56] X. Zhang, private communication, Cern, April 1999

[57] G.V. Stupakov, "*Photoelectrons and Multipacting in the LHC: Electron-Cloud build-up*", LHC Project Report 141, October 1997

[58] F. Caspers, J.-M. Laurent, M. Morvillo, and F. Ruggiero, "*Multipacting tests with a resonant coaxial setup*", CERN LHC Project Note 110 (September 1997)

[59] *Cern accelerator Superconductivity in Particle Accelerator,* 206-209, Haus Rissen, Hamburg - Germany*,* 17-24 May 1995, Yellow book, CERN 96-03 June 19

[60] K. Ohmi, "*Beam-photoelectron instability at KEKB: applying a magnetic field*", KEK Preprint 98-37 (1998), presented at the 1st Asian Particle Accelerator Conference (APAC98) Tsukuba, Japan, 23-27 March 1998.

Part VI

Appendixes

Appendix A

Fourier series of the RF pulse

As previously discussed a displacement potential typically from 0 to 200 Volt has been applied to the wires, in order to shift the pulses by the desired voltage. As the amplifier is a 1-1000 MHz frequency band, this results in a RF pulse spectrum which is cut in its DC component (0MHz, n=0 on the right of Fig. A-1) at the amplifier output; the typical RF pulse signal as recorded at scope (chamber output) is shown on the *left* of Fig. A-1; *right*-hand side shows the Fourier spectrum (amplitudes normalized to 1) of the real pulse, compared to the Fourier spectrum of a square pulse (where the normalized amplitude V=1).

For a square pulse ($|V_- |=V_+$) the Fourier series is

$$f(t) = \frac{4V}{\pi} \sin \omega t + \frac{4V}{3\pi} \sin 3\omega t + \frac{4V}{5\pi} \sin 5\omega t + ... = \sum_{n=1}^{\infty} \frac{4V}{n\pi} \sin n\omega t \quad n = 1, 3, 5....$$

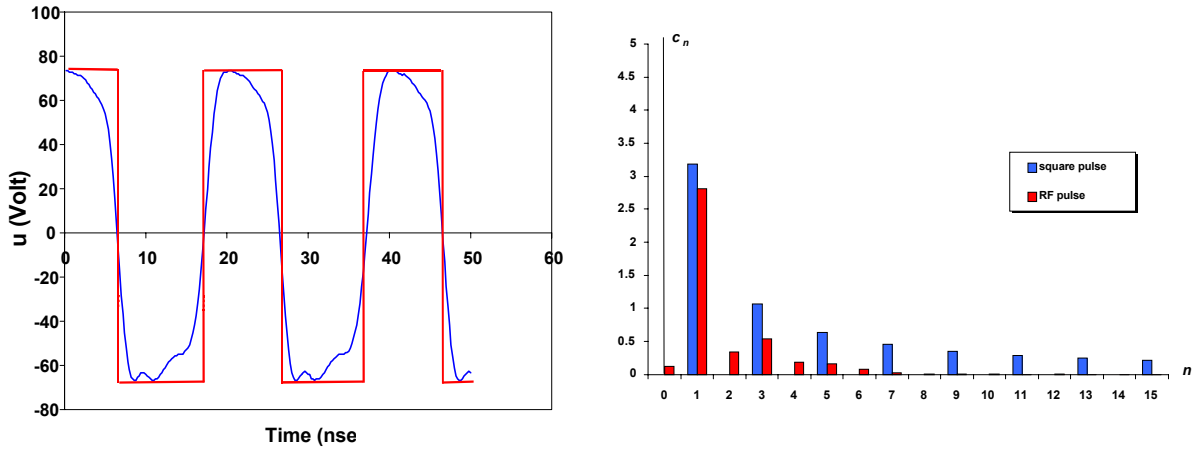

Figure A-1: left*: typical RF pulse signal at the scope (V_{p-p}=140 V).*
right*: related fourier spectrum of the RF pulse compared to the fourier spectrum of a square pulse (amplitude normalized to 1)*

Appendix B

Setting the correct square pulse amplitude for the simulations

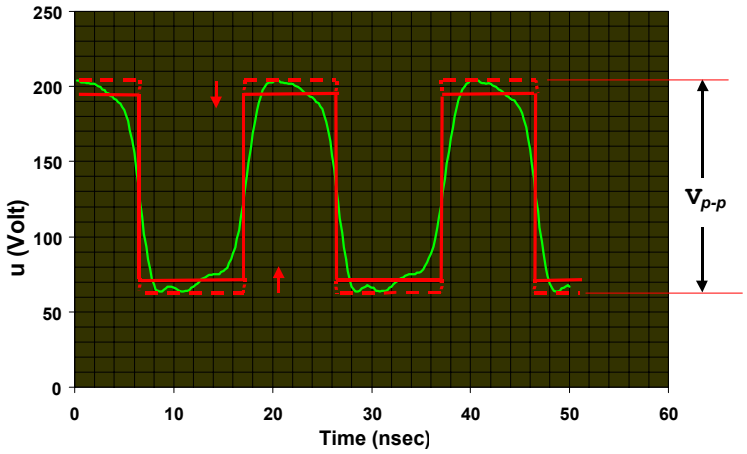

Figure B-1: *Real pulse amplitude and rectangular pulse used in the simulations*

The real RF pulse has been approximated with a square pulse shape, which has been used in the theoretical studies and in the simulations.

To simulate correctly the pulse amplitude V_{p-p} of a real RF pulse, the amplitude of the square pulse has to be set properly. Therefore, using a 2D (*Mathematica*) program, I integrate the equations of motion for an electron in the multi-wire chamber with:

- a real RF pulse or with
- a rectangular pulse

TOF and the impact energy of the electron during its flight across the chamber is determined, with a real RF pulse. Furthermore, I calculate the TOF and the impact energy of the electron, with a rectangular pulse.

The correct rectangular pulse amplitude is found when the electron crosses the chamber with the same time of flight and hits the surface with the same energy, as for the real pulse[1]. The amplitude of the square pulse is decreased until the correct value is found, as shown in Fig. B-1 in the case of V_{p-p}=140V.

[1]If in the simulations we set a square pulse amplitude equal to the real pulse amplitude V_{p-p}, it results in smaller TOF and overestimation of the electron energy.

Appendix C

LHC multipacting simulation program adapted to the multi-wire chamber geometry

In the simulation program the electrons are modelled by macro-particles which initially carry the same charge. In all simulations I generate 1000 and 2000 macro particles, for the first 20 pulse passages.

The real RF pulse has been approximated with a square pulse.

In order to simulate correctly the peak to peak amplitude V_{p-p} of a real RF pulse the amplitude of the square pulse has been set as discussed in section 3.2.

The pulse and the gap between two pulses are both divided in 50 slices, allowing a proper modelling of the particle motion, particularly under the influence of space charge [3].

The recalculation of the space charge field is very time consuming, nevertheless it has been calculated 10 times during two pulse passages. For the space charge field calculation we assume a four-fold symmetry of the electron cloud and map all electrons into one quadrant of the transverse plane. In a second step we calculate the electric field components of the electron cloud on a 25 times 25 (or 50 times 50) mesh and store the results on a two dimensional matrix for tracking. An additional option allows the generation of image charges which lead to an equipotential surface at the vacuum chamber. Once an electron reaches the boundary of the vacuum chamber the program calculates the secondary emission yield of the incident electron as a function of its energy and incident angle θ with respect to the surface normal. The charge of the emitted macro-particle is given by the product of the initial charge and the secondary emission yield $\delta(E,\theta)$. For the secondary emission yield we assume

$$\delta(E,\theta) = \frac{\delta_{\max} \cdot 1.11 \cdot \left(\frac{E}{E_{\max}}\right)^{-0.35} \cdot \left(1 - e^{-2.3\left(\frac{E}{E_{\max}}\right)^{1.35}}\right)}{\cos\theta} \tag{C.1}$$

where E is the electron energy, E_{max} the energy for which the secondary emission yield has a maximum and $\delta_{\max}$ the maximum secondary emission yield for normal incidence of the electron [15].

I assume during simulations $E_{max} = 350eV$, unless otherwise stated, and limit the $\cos\theta$ to values lower then 0.2.

Fig. 3-4 shows the theoretical curve C.1.

The energy distribution of the emitted macro particle is determined by a MonteCarlo algorithm, which in principle, can generate an arbitrary distribution. However, the initial energy distribution of the secondary electrons is still an unknown parameter. Last measurements at CERN indicates that most of the secondaries are emitted at very low energy (0-5 eV) with a FWHM of ca. 4.4 eV [18].

If an electron hits a central wire it is considered lost in the simulation, as it produces low energy secondary electrons which are attracted back to the wire due to its positive potential.

Appendix D

Calibration of the residual gas analyzer

On the test set-up, cold chatode gauges, ionisation gauges and a residual gas analyser are used to measure the total and partial pressure of the vacuum system. Those instruments output currents proportional to the total or partial pressure of the gas present in the system; the proportionality coefficients, called the sensitivity or calibration factors, depend on the individual instrument, on their power supplies and characteristics and vary with the gas to be measured. They are generally provided with calibration mean values and some are individually calibrated in the laboratory.

Total pressure gauges calibration

In vacuum ionisation gauges, the molecules of the residual gas are ionised by a low energy electron beam oscillating in the gauge volume, and the ion current is measured by an electrometer. The calibration factor, called the sensitivity of the gauge, S, is defined as $I = iPS$

with I the ion current, i the electron current (or emission current) and S the sensitivity of the gauge, which depends on the gauge, the power supply settings and the gas species. The individual calibration factors are measured in the laboratory.

Residual gas analyzer (RGA) calibration

The molecules of the residual gas are ionized in the ion source of the gas analyser by a low energy electron current i_G. The ions are extracted from the source and separated by a quadrupole mass filter, according to their ratio M/q. The ions are collected by a faraday cup, or amplified by a secondary emission multiplier if their intensity is too low, and the resulting current $I^+_{G_k}$ measured by an electrometer. The output signal of the electrometer is recorded as a function of the quadrupole mass filter excitation and produces peaks characteristics of the different species present in the residual gas. The calibration of the analyser gives the ratio between the peaks, expressed in Ampere, and the partial

pressures of the corresponding gas, in torr, according to $S = \frac{I^+}{P}$. The calibration can also be expressed relative to nitrogen. The base equation for the residual gas analyzer is

$$p_k = \frac{I^+_{G_k}}{s_{rG_k} \cdot s_{aG} \cdot i_G} \tag{D.1}$$

where p_k (torr) is the partial pressure of each gas, s_{rG_k} is the relative sensitivity for each gas species, and s_{aG} the absolute sensitivity related to the N_2 ($torr^{-1}$) nitrogen equivalent pressure is given by

$$s_{aG} = \frac{I^+_{G_{N_2}}}{i_G \cdot p_{N_2}} \tag{D.2}$$

The calibration provides the sensitivity factor for each gas as shown in the following tables. The sensitivity of the RGA for each gas peak is shown on the left table, while the cracking pattern of the gases is given on the right-hand side table.

peak	RGA sensitivity
2 of H_2	1.47
15 of CH_4	0.08
18 of H_2O	1.47
28 of N_2	0.3
28 of CO	0.27
40 of Ar	0.23
44 of CO_2	0.15
28 of C_2H_6	0.14
29 of C_3H_8	0.14

		RGA cracking pattern
N_2	14/28	0.07
Ar	20/40	0.10
CO	12/28	0.01
	14/28	0.004
C_2H_6	26/28	0.25
	27/28	0.31
	29/28	0.19
	30/28	0.19
CH_4	12/16	0.15
	14/16	0.05
	15/16	0.91
CO_2	28/44	0.6

Acknowledgments

I wish to thank:

Dr. O. Gröbner for his extraordinary competence in the subject, for his precious kindness which helped me a lot during these two years

Prof. E. Chiavassa for stimulating and difficult questions and for his fanciful kindness

J.M. Laurent for continuous help and suggestions which improved a lot the work

M. Morvillo for everything: a lot of brilliant ideas come directly from him, a source of inspiration for me

F. Ruggiero for very stimulating discussions on the electron cloud

N. Hilleret for a very useful ideas on the conditioning effect and for teaching me to be the first to doubt about my results

I. Collins and A. Rossi that make it possible for you to read this thesis in English, in particular Ian makes me very happy when he mentioned about my work during his electron cloud seminar in the CERN/LHC auditorium, and Adriana who helped me like a brother

O. Bruning, F. Zimmermann, X. Zhang for their collaboration in using the LHC simulation program and for useful discussions

M. Gautier and K. Magyary for their competence in vacuum and precious help

D. Latorre for Auger analysis and help to analyse the results

C. Scheuerlein, B. Henrist and G. Vorlaufer for help and lot of discussions on the subject

M. Taborelli for the idea of carbon growth during electron bombardment

G. Arduini and M. Jimenez for their help during the last MD measurements in the SPS

Barbara